ABSOLUTE PHOTOABSORPTION AND PHOTOIONIZATION STUDIES OF THE

HYDROGEN HALIDES HCl, HBr, AND HI, BY DIPOLE (e,e) AND (e,e+ion)

SPECTROSCOPIES IN THE UV, VUV AND SOFT X-RAY REGIONS

by

MONICA KAREN DYCK

B.Sc., Trinity Western University, 1994

A THESIS SUBMITTED IN PARTIAL FULFILLMENT OF

THE REQUIREMENTS FOR THE DEGREE OF

MASTER OF SCIENCE

in

THE FACULTY OF GRADUATE STUDIES

DEPARTMENT OF CHEMISTRY

We accept this thesis as conforming

to the required standard

THE UNIVERSITY OF BRITISH COLUMBIA

April 1997

In presenting this thesis in partial fulfilment of the requirements for an advanced degree at the University of British Columbia, I agree that the Library shall make it freely available for reference and study. I further agree that permission for extensive copying of this thesis for scholarly purposes may be granted by the head of my department or by his or her representatives. It is understood that copying or publication of this thesis for financial gain shall not be allowed without my written permission.

Department of ___CHEMISTRY___

The University of British Columbia
Vancouver, Canada

Date ___April 28, 1997___

Abstract

The absolute differential oscillator strengths (cross sections) for the photoabsorption spectra of the three hydrogen halide molecules HCl (5-280 eV), HBr (5-300 eV), and HI (5-120 eV) have been obtained by using dipole (e,e) spectroscopy, at both low (1 eV fwhm) and high (0.05-0.1 eV fwhm) resolution. Data for the valence and selected inner shells (Cl 2p, Br 3d, and I 4d) have been obtained at equivalent photon energies from the UV to soft X-ray regions. The absolute oscillator strength scales were determined by use of the VTRK (S(0)) sum rule for HCl, and the dipole polarizability (S(-2)) sum rule for HBr and HI. The value of the dipole polarizability derived from the VTRK normalized spectrum of HCl is in very good agreement with published experimental values.

In further experiments, dipole (e,e+ion) spectroscopy has been used to investigate the molecular and dissociative photoionization of HCl and HBr, in the valence and selected inner shell (Cl 2p, Br 3d) regions. Photoion branching ratios for molecular and dissociative photoionization determined from time-of-flight mass spectra have been used together with the absolute photoabsorption data to obtain partial photoionization differential oscillator strengths. Photoionization efficiencies have also been obtained. A consideration of the partial differential oscillator strengths for molecular and dissociative photoionization together with the electronic state partial differential oscillator strengths (obtained from earlier dipole (e,2e) studies, *Chem. Phys.* **83** (1984) 391, *Chem. Phys.* **98** (1985) 367) provides information concerning the dipole-induced breakdown pathways of HCl and HBr.

Table of Contents

List of Tables

List of Figures

Acknowledgements

I would like to sincerely thank my research supervisor, Dr. C.E. Brion, for his assistance, support, expertise, and patience through the course of my research and the writing of this thesis. Special thanks are also due to Dr. Glyn Cooper and Dr. Terry N. Olney who taught me what I needed to know about the technique of dipole (e,e) spectroscopy, as well as giving me a lot of help along the way and answering many questions. I wish to also thank the rest of the research group for their support and advice: J. Au, J. Neville, J. Rolke, and Dr. Y. Zheng.

Finally, I wish to thank my parents for their constant, wholehearted support and encouragement. This thesis is dedicated to them.

Chapter 1

Introduction

1.1 Background

A quantitative knowledge of the primary and secondary processes taking place in radiation chemistry, physics, and biology is essential for understanding and predicting the interaction of energetic radiation with matter. The primary step involves absorption of a photon by the molecule, followed by decomposition (i.e. ionization, dissociation, fluorescence, etc...). Above ~20 eV in the vacuum ultraviolet, decomposition is dominated by molecular ionization and ionic photofragmentation processes, in which one or more positively charged ions are formed per photon absorbed. In particular it is necessary to know not only the energies of the electronically excited and ionized states of atoms and molecules, but also the associated transition probabilities [cross sections (σ) or oscillator strengths (df/dE), where σ (megabarns) = 109.75(df/dE)eV^{-1}]. Such photoabsorption and photoionization data are useful in a variety of applications. Important areas requiring such absolute measurements include radiation-induced decomposition, dosimetry, radiation therapy and health physics, upper atmosphere modelling, space chemistry and physics, environmental protection, fusion, plasmas, electron and X-ray microscopy, the nuclear industry and indeed any area where energetic radiation or particles are to be found [1].

Dipole electron impact studies have provided much useful information (examples of which can be seen in the following references [2, 3, 4, 5, 6, 7]) regarding the electronic processes that occur within atoms or molecules. These studies give absolute photoabsorption and photoionization spectra, and thus absolute optical oscillator strengths (transition probabilities) over wide energy ranges, encompassing the valence and inner-shell regions. In the present work results of high impact energy electron energy loss spectroscopy (EELS) experiments in the dipole

1

regime are presented for the photoabsorption, photoionization and ionic photofragmentation of the hydrogen halides HCl, HBr, and HI. Dipole studies of the photoabsorption and photoionization of HF have been reported earlier [8, 9].

Traditionally spectroscopic investigations have used direct optical techniques to measure optical oscillator strengths for photoabsorption and photoionization processes. However, application of direct optical methods has proven to be somewhat limited, especially for studies of absolute transition probabilities in the far UV, vacuum UV, and soft X-ray regions of the spectrum. These regions are important as they cover formation of most of the electronically excited and ionized states of the valence shell as well as all inner shell transitions. The reasons for these limitations will be discussed in sections 1.2 and 1.3. A more recent advance in the measurement of absolute photoabsorption and photoionization oscillator strengths has been the use of inelastic collisions of high energy electrons at zero degree scattering angle [1, 2]. In electron impact experiments with sufficiently high impact energy and negligible momentum transfer, dipole selection rules operate and the excitation or ionization cross section is directly related to the optical oscillator strength. Therefore such dipole electron impact techniques, utilizing electron energy loss spectroscopy, can be used to determine the optical oscillator strengths (cross sections) for photoabsorption and photoionization of atoms or molecules as a function of electron energy loss, which is equivalent to the photon energy [1]. Why this is possible and how it is accomplished will be described further in sections 1.3, 2.1 and 2.2. The basic function and features of the dipole (e,e) and dipole (e,e+ion) instruments used to obtain this data will be described in chapter 3. Finally, in chapters 4-6 the experimental results for the three hydrogen halide molecules HCl, HBr, and HI will be reported and discussed, comparing the

present work with previously published data, in those cases where such information is available. Very little absolute photoabsorption and photoionization data is available for these molecules using direct optical techniques. Much earlier low resolution dipole (e,e) and (e,e+ion) measurements for HCl and HBr [10, 11] over limited energy ranges are possibly subject to appreciable errors due to limitations in the instrumentation and measurement precedures used at the time. Absolute photoabsorption oscillator strength (cross section) data have been obtained for the valence and selected inner shell processes for the three hydrogen halide molecules HCl, HBr, and HI in the UV, vacuum UV, and soft X-ray energy regions at high resolution. Photoionization and ionic photofragmentation oscillator strength (cross section) data have also been obtained over extended energy ranges for HCl and HBr from the absolute photoabsorption data and photoion branching ratios determined from time-of-flight (TOF) mass spectra obtained in the valence and inner shell regions of each molecule.

1.2 Conventional Photoabsorption Methods

Optical methods of spectroscopy, such as Beer-Lambert law photoabsorption, are capable in principle of giving reliable and accurate absolute measurements. However such information is limited and typically available only over short ranges at lower photon energies. Prior to the advent of synchrotron radiation, the principal limitation was the shortage of suitable continuum light sources at energies above 20 eV. Conventional discharge light sources using hydrogen and noble gas continua give useful but relatively weak structured continua up to ~20 eV [12]. In the past two decades the growing availability of tuneable synchrotron radiation, long viewed as an unwanted by-product of particle acceleration, has provided an intense photon source with a continuum stretching from the IR through the UV and vacuum UV and up to the hard X-ray

region, in the case of high GeV machines. Synchrotron radiation sources are giving some impressive spectroscopic results, however the access to such sources is still limited, and the technique presents other difficulties, particularly for *absolute* photoabsorption and photoionization measurements. In particular, direct optical studies are subject to the problems involved in the dispersion (i.e. energy selection) of *short* wavelength radiation. For example, mirrors and gratings, which are necessary for the monochromation used in optical techniques, suffer from very low reflectivity at shorter wavelengths (i.e. photon energies above 20-30 eV). This severely attenuates the usable monochromated photon intensity in spite of the high flux from the synchrotron source. However, it should be noted that significant higher photon fluxes have very recently become available with Third Generation sychrotron radiation sources such as the Advanced Light Source at the Lawrence Berkeley Laboratory [13]. Other difficulties in using VUV and soft X-ray radiation include the presence of higher order radiation (i.e. order overlapping), stray light corrections and light absorption by optical components, particularly in the carbon K region due to surface contamination [14]. Furthermore, in order to compensate for low light fluxes, energy resolution has often been sacrificed for sufficient intensity in optical work at shorter wavelengths [1]. A further difficulty in absolute optical measurements is the need to determine accurately the target density of the molecules and pathlength of the absorption cell, which is usually windowless in the VUV and soft X-ray regions.

Optical measurements can suffer from a further extremely serious problem in determining absolute oscillator strengths (cross sections) for *discrete* transitions. In particular the measurements typically require the use of the Beer-Lambert law, which relates absorption to the ratio of the intensities of the incident to transmitted light. This involves a logarithmic

transformation, and for discrete transitions the resulting absorption cross sections can suffer from the problem of "line saturation" if the spectrometer bandwidth is not significantly narrower than the natural linewidth of the narrowest line in the spectrum [3, 15]. Line saturation errors, which can in some cases be appreciable [3], result in cross-sections which are too small.

In terms of the intensity of the incident radiation, I_o, the Beer-Lambert law states that the intensity of the transmitted radiation, I, is given by

$$I = I_o e^{-n\sigma l} \tag{1.3.1}$$

where n is the number of molecules per cm^3, σ is the photoabsorption cross section (cm^2) of the molecule, and l is the pathlength in cm. Therefore, to obtain σ, the following logarithmic transform must be performed:

$$\sigma = \frac{1}{nl} \ln \frac{I_0}{I} \tag{1.3.2}$$

where nl is usually referred to as the number density of the target molecules. The actual observed shape and height of any absorption peak, as well as the ratio (I/I_o) depends on the bandwidth, or energy resolution of the instrument, and therefore at each energy the natural log of the ratio will vary with resolution. Thus for an absorption peak corresponding to a *discrete* excitation the true value of σ can, in principle, only be obtained if the instrument has infinite resolution, which requires the bandwidth to be equal to zero. Practically, this is obviously impossible, and this situation presents a further limitation of optical spectrometers in some situations. Ideally, in order to obtain a reasonably accurate absolute cross section, the instrumental bandpass should be significantly narrower than the natural linewidth of all discrete excitations in the spectrum of interest. The largest errors occur for transitions with high cross sections and very narrow

linewidths [3, 6]. These problems are particularly likely to occur at shorter wavelengths in the VUV and soft X-ray regions, since here the monochromated light flux can be quite low, and as a result the slits in the spectrometer are often opened up to compensate, resulting in lower resolution and greater bandpass. Care should therefore be taken in obtaining the optical cross sections, especially in the case of very strong, narrow bands, as they are more prone to the so called "line saturation" effects caused by the Beer-Lambert law. It is possible to reduce these errors by making the Beer-Lambert law measurements as a function of pressure and extrapolating to zero pressure [3, 16]. However this procedure is tedious and can still result in appreciable errors since the error bars are largest at the lowest pressures [16].

1.3 Photoabsorption and Photoionization by Fast Electron Impact

Dipole electron impact techniques avoid the difficulties of limited photon energy range, order overlapping, stray light, and low reflectivity at short wavelengths which are problematic in direct optical methods for photoabsorption measurements. In addition, such electron scattering techniques do not require path length or number density determinations for absolute measurements. The problem of "line saturation" when using the Beer-Lambert law is also avoided in dipole electron impact experiments using EELS since the measurements involve only the determination of the number of scattered electrons at each energy loss, and no logarithmic transform is involved.

In 1935, using the Born approximation, Bethe showed [17] that for inelastic fast electron impact on an atomic or molecular target there is a quantitative relationship (see section 2.1) between the differential electron scattering cross section and the optical oscillator strength, in the
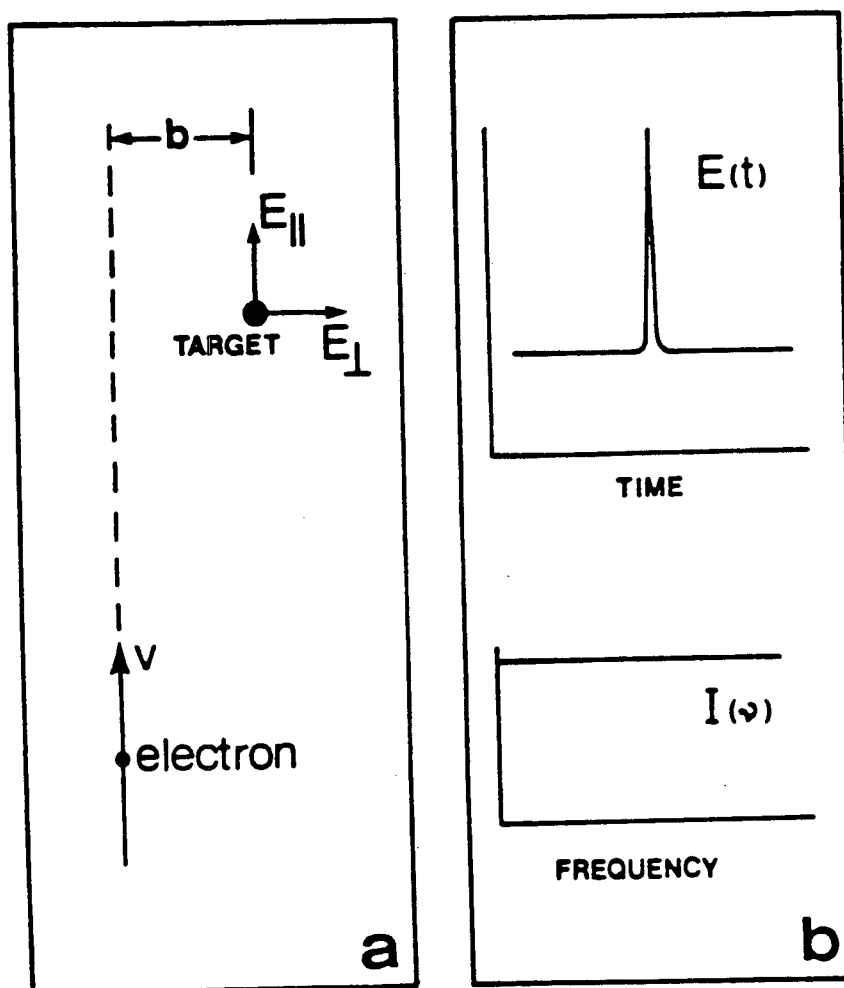
Figure 1.1. Virtual photon field induced in a molecular target by distant collision of a fast electron.

limit of zero momentum transfer (i.e. at high impact energy and zero degree scattering angle). Such fast impacting electrons provide an excellent simulation of a tuneable light source due to their ability to induce a virtual photon (dipole) field in the target molecule. As a fast electron passes by, the target experiences a sharp electric field pulse in the time domain (see Figure 1.1). If this function is Fourier transformed into the frequency domain, the result is a continuum composed of all frequencies at equal intensities. In reality, the initial pulse has a finite, though narrow, width, and the "flat" intensity falls off at higher frequencies. However, under appropriate kinematic conditions a sufficiently wide spectral range of equal intensity can be achieved for use in the laboratory. Continuous energy transfer to the target is possible over essentially a very large portion of the electromagnetic spectrum. In dipole electron energy loss spectroscopy (EELS) experiments the continuously variable energy loss is analogous to photon energy (see section 2.2). An electron beam is readily produced by thermionic emission and the energy losses of the inelastically scattered electrons can be continuously selected by means of a linear ramp potential and an electrostatic electron analyzer, thus simulating photoabsorption using a tuneable source of radiation. Since the intensity of the "pseudo photons" produced by passing fast electrons is constant with energy loss E, there is a "flat" virtual photon source, which therefore gives the correct *relative* spectral photoabsorption shape [2]. Whereas optical methods require several different monochromators to cover sufficiently wide ranges of wavelength, dipole electron impact methods simply require scanning of the energy loss in a single spectrometer to cover a very wide spectral range. The target density, or pressure, is kept constant and sufficiently low so as to avoid multiple scattering processes. No determination of the absolute target density is required since absolute scales are determined using the S(0) or S(-2) sum rules as described in section 2.4. Thus

quantitative photoabsorption, photoionization and photoelectron (PES) spectroscopies can be simulated by appropriate dipole electron impact methods using EELS [2].

Limitations to the technique of electron energy loss measurements by dipole (e,e) spectroscopy include the significant drop-off of the signal at higher energies, due to the $\sim E^3$ dependence of the Bethe-Born conversion factor (see section 2.2). This effectively imposes an upper limit to the energy range accessible by this method. A second difficulty is the presence of stray electrons and background gases in the measured energy-loss spectrum. This problem can be avoided by careful and correct background subtraction. Thus far, the determination of *absolute* photoabsorption data by dipole (e,e) methods is limited to gas phase experiments. Dipole electron impact techniques, used within these limitations, still provide an excellent method of obtaining data for the photoabsorption and photoionization of a variety of atomic and molecular targets.

Chapter 2

Theoretical Background

2.1 The Dipole (e,e) Method and the Bethe-Born approximation

Bethe's work using the Born theory of particle scattering provides the basis for dipole electron scattering studies [17, 18]. An important result of the Bethe-Born theory is the quantified relationship between the electron impact differential inelastic scattering cross section $d\sigma/dE$ and the generalized differential oscillator strength $df/dE(K)$.

$$\frac{d\sigma}{dE} = \frac{2}{E} \cdot \frac{k_n}{k_o} \cdot \frac{1}{K^2} \cdot \frac{df(K)}{dE} \qquad (2.1.1)$$

where k_o, k_n, and K are the incident, scattered and transferred momenta respectively, and E is the energy loss. Bethe further showed that the generalized oscillator strength could be expanded into a series of terms, the first of which is the optical or dipole oscillator strength, and the higher (non-dipole) terms involve higher powers of K, the momentum transfer.

$$\frac{df(K)}{dE} = \frac{df_o}{dE} + AK^2 + BK^4 + \dots \qquad (2.1.2)$$

From the cosine rule,
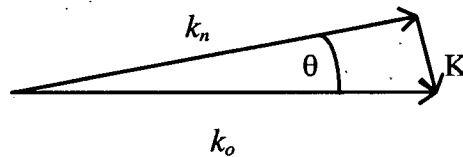
$$K^2 = k_o^2 + k_n^2 - 2k_o k_n \cos\theta \qquad (2.1.3)$$

It can be seen from equation 2.1.3 that K^2 approaches zero at high impact energy E_o (i.e. $k_o \sim k_n$) and zero scattering angle ($\theta = 0°$). Therefore in the limit of zero momentum transfer K, the generalized oscillator strength becomes equal to the optical oscillator strength and dipole selection rules are operative. Under these (dipole) conditions,

10

$$\frac{df_o}{dE} = \frac{E}{2} \cdot \frac{k_o}{k_n} \cdot K^2 \cdot \frac{d\sigma}{dE}$$ (2.1.4)

The optical oscillator strength is related to the absolute photoabsorption cross section σ_{phabs} by the relation

$$\sigma_{phabs} = 109.75(df_o/dE)$$ (2.1.5)

where σ_{phabs} is in megabarns (1 Mb = 10^{-18} cm^2) and df_o/dE has units of eV^{-1}. Thus the Bethe-Born theory shows that dipole transitions are induced in the target by fast electrons, and also that their optical oscillator strengths (i.e. transition probabilities) can be obtained by a simple kinematic conversion of the corresponding differential electron scattering intensities. The kinematic quantity $(2/E)(k_n/k_o)(1/K^2)$ in equation 2.1.4 is independent of the target species and is known as the Bethe-Born conversion factor. In practice this factor must be integrated over the small range of momentum transfers within the finite acceptance angle subtended about zero degrees by the spectrometer entrance slit. The Bethe-Born factors for each of the two instruments used in the present work have been detailed earlier [3, 19, 20]. This allows quantitative optical spectroscopy to be carried out using dipole electron impact methods.

2.2 Photoabsorption by Dipole (e,e) Spectroscopy

In direct photoabsorption experiments, when a molecule AB absorbs a photon of energy $E = h\nu$, the process results in an excited state AB*:

$$AB + h\nu \rightarrow AB^*$$ (2.1.1)
$$E$$

The probability for these processes (including all discrete and continuum states), as a function of energy, E, is given by the absolute total photoabsorption cross section. The same molecular excitation process can also occur in an inelastic electron scattering (i.e. dipole (e,e)) experiment

using an incident electron beam of fixed high energy E_o. The process can be represented by:

$$e^- + AB \rightarrow AB^* + e^-_{scatt} \qquad (2.1.2)$$
$$E_o \qquad\qquad\qquad (E_o - E)$$

where the incident electron (with impact energy E_o) imparts an energy E to the target during the excitation, and is scattered with a final energy (E_o-E). Under the conditions used in the present work (i.e. zero mean scattering angle and high incident electron energy) the kinetic energy transferred to the target molecule is small (< 1 meV), and therefore it can be seen from equations 2.1.1 and 2.1.2 that the energy loss, E, of the electron is equivalent to the photon energy, hν, in dipole (e,e) spectroscopy. With this equivalence in mind all energy scales in the present work are labelled as "photon energy."

As shown in section 2.1, in the limit of zero momentum transfer to the target molecule, dipole-allowed transitions are excited by fast electron impact. As the momentum transfer is increased, higher multipole transitions can be excited [18]. Under the high impact energy and zero degree mean scattering angle conditions of dipole (e,e) spectroscopy the momentum transfer is extremely small and the contributions from multipole transitions are negligible (< ~1%). Also, as described in section 2.1, the photoabsorption oscillator strength is related to the differential electron scattering cross section by the kinematic Bethe-Born factor $(E/2)(k_o/k_n)K^2$, which can be shown to be essentially proportional to E^3 at zero degree scattering angle in the hypothetical case of infinitely small acceptance angle [2]. In practice, integration over the range of K^2 in the finite acceptance angle slightly modifies this relationship [3, 19, 20]. It can be seen that the electron scattering signal will fall off more rapidly with energy loss than does the photoabsorption cross section by a factor of ~E^3 (or typically ~ $E^{2.5}$ to $E^{2.7}$ in the real case of finite acceptance angles). Therefore great care must be taken to account for any background due to stray electrons,

impurities or background gases.

The kinematic Bethe-Born factor is a function of the energy loss E, and is the same for all targets, but is spectrometer-dependent in that it depends on the acceptance angle of the particular spectrometer used and on the impact energy E_o. The Bethe-Born factor can be determined directly from an analysis of the scattering geometry of the spectrometer [3, 20], or it can be derived from the ratio of the Bethe-Born converted energy-loss signal to a known accurate absolute photoabsorption oscillator strength over a wide range of energies in the smooth continuum region [3, 19].

Thus the technique of dipole (e,e) spectroscopy can be used to measure photoabsorption oscillator strengths. The notation "dipole (e,e)" simply indicates that the conditions of the experiment determine that effectively only dipole-allowed transitions are studied, and that the process involves an incident electron and the release of a scattered electron. The dipole (e,e) technique uses electron energy loss spectroscopy, EELS, for the detection of scattered electrons with specific energy loss. In an EELS spectrometer the energy loss, E, can be continuously varied by changing a linear ramp voltage. A programmable DC power supply may therefore be used as the analogue of a scanning monochromator. A single power supply can scan a very wide energy range, from the IR to the X-ray region, thus avoiding the necessity of using several complex optical monochromators. In summary, dipole (e,e) spectroscopy simulates tuneable energy photoabsorption, with the energy loss being the equivalent of the photon energy [1, 2, 3].

2.3 Photoionization by Dipole (e,e+ion) Spectroscopy

If the photon energy hv supplied to the molecule AB is above the first ionization potential, then an electron, e^-_{ej}, can be produced and a positively charged molecular or fragment ion will be

formed:

$$AB + h\nu \rightarrow AB^+ + e^-_{ej} \qquad \text{Molecular Photoionization} \qquad (2.2.1)$$

$$\rightarrow A^+ + B + e^-_{ej} \qquad \text{Dissociative Photoionization}$$
$$E$$
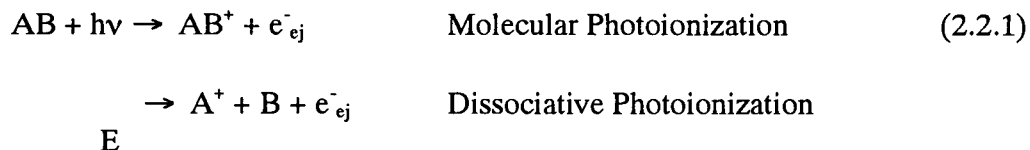
The same processes can also occur in an inelastic electron scattering (i.e. dipole (e,e+ion)) experiment, where a fast incident electron beam of energy E_o and energy loss E, can cause the formation of a molecular or fragment ion, an ejected electron e^-_{ej} , and a fast scattered electron e^-_{scatt} :

$$e^- + AB \rightarrow AB^+ + e^-_{ej} + e^-_{scatt} \qquad \text{Molecular photoionization} \qquad (2.2.2)$$

$$\rightarrow A^+ + B + e^-_{ej} + e^-_{scatt} \qquad \text{Dissociative photoionization}$$
$$E_o \qquad\qquad\qquad (E_o - E)$$
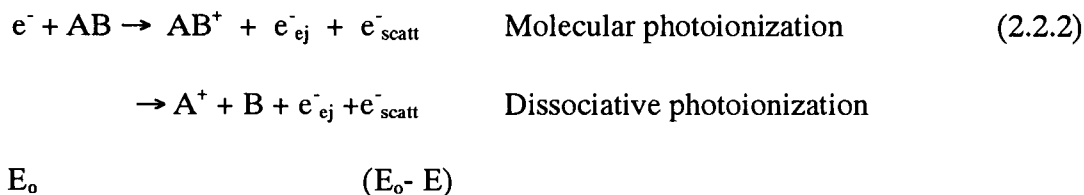
Thus the inelastic electron scattering experiment simulates photoionization with the energy loss E of the incident electron being used in the formation of $AB^+ + e^-_{ej}$ (or $A^+ + B + e^-_{ej}$).

The total photoionization oscillator strength distribution is made up of the sum of the partial photoionization oscillator strengths for the production of the molecular and all dissociative ions. In photoionization mass spectrometry, or in the equivalent electron-impact-based technique of dipole (e,e+ion) spectroscopy used in the present work, mass spectra are measured as a function of the equivalent photon energy (i.e. the energy loss) in order to determine what products of photoionization are formed at the energies absorbed by the target molecule. A useful quantity is the photoion branching ratio, BR^{ion}, which represents the intensity of a given ion relative to the total number of ions formed at any particular photon energy. It is determined by integration of the peaks in the baseline-subtracted mass spectra, and varies as a function of the photon energy. The partial photoionization oscillator strength (PPOS) for the production of a

molecular or dissociative ion, x, (df_x^{ion}/dE) is given by the triple product of the photoion branching ratio for the ion, the photoionization efficiency (η_i), and the absolute photoabsorption oscillator strength, determined in the present work from dipole (e,e) spectroscopy:

$$\frac{df_x^{ion}}{dE} = BR_x^{ion} \cdot \eta_i \cdot \frac{df_o^{abs}}{dE} \qquad (2.3.3)$$

The photoionization efficiency, η_i , is the probability that an ion is formed when a photon is absorbed. In the present dipole (e,e+ion) work, time-of-flight mass spectroscopy is used to determine the photoion branching ratios, by coincident detection of the fast scattered energy loss electron and the molecular ion produced in the dipole (e,e+ion) experiment. The photoionization efficiency η_i is also determined. The *total* photoionization differential oscillator strength distribution is equal to:

$$\frac{df_{Total}^{ion}}{dE} = \sum_x \frac{df_x^{ion}}{dE} = \eta_i \cdot \frac{df_o^{abs}}{dE} \qquad (2.3.4)$$

and is the sum of the PPOS's for the molecular and each dissociative ion, x.

The related techniques of photoelectron spectroscopy (PES) and dipole (e,2e) spectroscopy allow the determination of how the production of electronic states, j, of the molecular ion varies with the energy absorbed by the target [1, 2]. The electronic ion state (i.e. photoelectron) branching ratios can be determined from the background subtracted photoelectron (or dipole (e,2e)) spectrum in a manner analogous to that for photoionization branching ratios, and hence partial photoionization oscillator strengths for the production of electronic ion states, j, can be determined:

$$\frac{df_j^{ion}}{dE} = BR_j^{ion} \cdot \eta_i \cdot \frac{df_o^{abs}}{dE} \qquad (2.3.5)$$

Thus the total photoionization differential oscillator strength distribution can also be represented by the sum of the partial photoionization oscillator strengths for the formation of each of the electronic ion states j of the molecular ion.

$$\frac{df^{ion}_{Total}}{dE} = \sum_j \frac{df^{ion}_j}{dE} = \eta_i \cdot \frac{df^{abs}_o}{dE} \qquad (2.3.6)$$

The dipole-induced breakdown pathways for a molecule can therefore be determined from an examination of these two complementary manners in which the total photoionization oscillator strength distribution can be partitioned (i.e. equations 2.3.4 and 2.3.6), together with a consideration of ionization and appearance potentials and the associated Frank-Condon widths for production of the electronic and ion states. The latter quantities can be estimated from high resolution PES measurements.

2.4 Absolute Photoabsorption Oscillator Strengths (Cross sections)

The "flat" virtual photon field induced in the target atom or molecule allows the correct shape of the spectrum to be obtained in dipole (e,e) spectroscopy as discussed above in sections 1.4 and 2.1. Thus, by an appropriate process of normalization of the Bethe-Born converted relative energy loss spectrum, the absolute intensities of the photoabsorption spectrum can be determined. In principle, normalization can be achieved at a single energy loss or photon energy to a known optical absorption cross section. However, this latter method requires sufficiently accurate optical data from the literature, and this is not always available. The normalization is carried out independently in the present work by the use of one or other of two dipole sum-rules [7, 18, 21], which avoids the very difficult measurement of absolute target densities which are required in direct optical absolute photoabsorption and photoionization cross section determinations. The Thomas-Reiche-Kuhn (TRK), or S(0), sum rule equates the total

photoabsorption oscillator strength, integrated over all discrete and continuum states of the valence and all inner shells, to the number of electrons in the target molecule. Since in the dipole (e,e) method all inner shells cannot in general be measured, the valence shell modification (VTRK) of the S(0) sum rule is used [22]. In the VTRK procedure Bethe-Born converted the valence-shell electron energy loss spectrum is obtained out to high energy and the small remaining intensity (typically 5 - 10%) to infinite energy is estimated by extrapolation of a polynomial curve fitted to the higher energy region of the valence shell measurements (typically from 100 to 200 eV). Assuming shell separation, the total area is then normalized to the number of valence shell electrons, N_{val}, plus a small correction, N_{PE}, for Pauli excluded transitions to the already occupied states [22]. Reasonably accurate values of N_{PE} are available from Hartree-Slater calculations [23]. The valence shell, or VTRK sum-rule is given by

$$S_{val}(0) = \int_{E_n}^{\infty} \left(\frac{df}{dE} \right)_{val} dE = N_{val} + N_{PE} \qquad (2.4.2)$$

where E_n is the first excitation threshold. Using the VTRK procedures an absolute scale can typically be obtained with an accuracy of better than ~5% [2, 7].

The VTRK sum rule normalization procedure requires the valence electron energy loss spectrum to be obtained up to relatively high energies (typically at least 200 eV), well into the valence shell photoabsorption continuum. For molecules such as HBr or HI, the VTRK sum rule becomes difficult to implement because lower-energy inner-shell transitions (eg. Br 3d and I 4d) can interfere [7]. In such cases other methods of absolute scale normalization must be used. The accuracy of the absolute differential oscillator strength scales established using the VTRK sum rule is estimated to be within ±5% [7]. It has recently been shown [7] that the S(-2) sum rule, which makes use of published experimental and theoretical dipole polarizabilities, can also be used

to normalize relative differential oscillator strength spectra or, alternatively, as a check of the absolute scales established by other methods, such as the VTRK sum-rule [7]. The S(-2) sum-rule is given by

$$S(-2) = \int_{E_n}^{\infty} \left(\frac{E}{E_H} \right)^{-2} \cdot \frac{df}{dE} \cdot dE = \alpha_{\infty} \qquad (2.4.2)$$

where α_{∞} is the static dipole polarizability and E_H is the Hartree atomic unit of energy. It can be seen that due to the $1/E^2$ weighting in equation 2.4.2 the dipole polarizability method of normalization depends overwhelmingly on the low energy region (typically $\leq$ 100 eV) of the valence shell spectrum, and thus has the advantage of relying on the region with the highest oscillator strength and typically the best signal-to-noise ratio. The S(-2) sum rule is used in the present work for normalization of the photoabsorption spectra of HBr and HI since the low lying transitions from the Br 3d and I 4d inner shells preclude the use of the VTRK sum rule. In addition, the accuracy of the oscillator strength scale in the VTRK sum rule normalized photoabsorption spectrum of HCl is evaluated by comparing the α_{∞} value derived using the S(-2) sum rule with directly measured and calculated values. The accuracy of measured dipole polarizabilities are generally considered to be accurate to within $\pm$1-2%.

Chapter 3

Experimental Methods

3.1 Introduction

Two instruments were used to collect the data: a low resolution (1 eV full-width half-maximum (fwhm)) dipole (e,e) and (e,e+ion) spectrometer, and a high resolution (0.048 eV fwhm) dipole (e,e) spectrometer. The energy loss data in each case were converted to relative photoabsorption cross sections by use of the Bethe-Born theory (see section 2.1). Each instrument has a known energy-loss-dependent Bethe-Born factor [3, 19], so the conversion is a simple matter of multiplying the intensity in the energy loss spectrum by the value of this factor (at each energy loss) to obtain relative photoabsorption data. The relative spectrum is then made absolute by use of sum rules (see section 2.4). In the case of HCl use of the VTRK $S(0)$ or the $S(-2)$ sum rules gives absolute scales which are in excellent agreement. For HBr and HI, where inner shell processes (Br 3d and I 4d respectively) at lower energy interfere with the curve fitting and extrapolation, use of the TRK sum rule is not possible, and the spectra in these cases were made absolute by using the $S(-2)$ sum rule and known values of the dipole polarizabilities. Partial photoionization oscillator strengths and photofragmentation branching ratios were obtained for HCl and HBr on the dipole (e,e+ion) instrument for valence and inner shell processes. The branching ratios were obtained from time-of-flight mass spectral studies. Partial oscillator strengths for molecular and dissociative photoionization were obtained by multiplying the branching ratios for each singly or doubly charged ionic species by the total photoabsorption oscillator strength and by the photoionization efficiency at each equivalent photon energy.

3.2 Low Resolution Dipole (e,e) and Dipole (e,e+ion) Spectrometer

The low resolution dipole (e,e) spectrometer (figure 3.1) is actually the non-coincident forward scattering portion of a dipole (e,e+ion) spectrometer which was initially built at the FOM institute in Amsterdam [20, 24, 25]. This instrument was moved to UBC in 1980, and further modified and refined [3, 7, 19, 26, 27] for use in absolute photoabsorption and photoionization studies. It has since been used with great success in studying a variety of molecules [2, 3, 4, 5, 7, 19].

The details of the construction and operation of the low resolution instrument can be found in a number of earlier publications [1, 24, 25, 26, 27]. An electron beam is produced by an indirectly heated barium oxide cathode in a black and white television gun (Phillips 6AW59) which is floated at a potential of -4 kV. The electrons are focussed with an einzel electron lens into the collision chamber which is floated at a potential of +4 kV. This provides acceleration of the incident electrons to 8 keV. The electron beam (typically $\sim2\times10^{-9}$ amps) inelastically scatters off the target molecule in the collision chamber, to excite electronic transitions to both neutral and ionic states, and in so doing loses energy. The forward scattered electrons (solid angle of acceptance of 1.4×10^{-4} sr) are selected by an angular selection aperture and then decelerated and focussed to a constant pass energy (typically 50 eV) using a series of five electron lenses. The electron beam is aligned through the various regions of the spectrometer using X,Y deflectors and apertures at which the current can be monitored. The energy loss is scanned by applying a linear ramp voltage to the last lens element in the deceleration lens, and to the whole analyzer and detector systems. Most of the electron beam which is not of the selected energy, is collected in the primary beam dump. The selected electrons are bent around the analyzer, pass
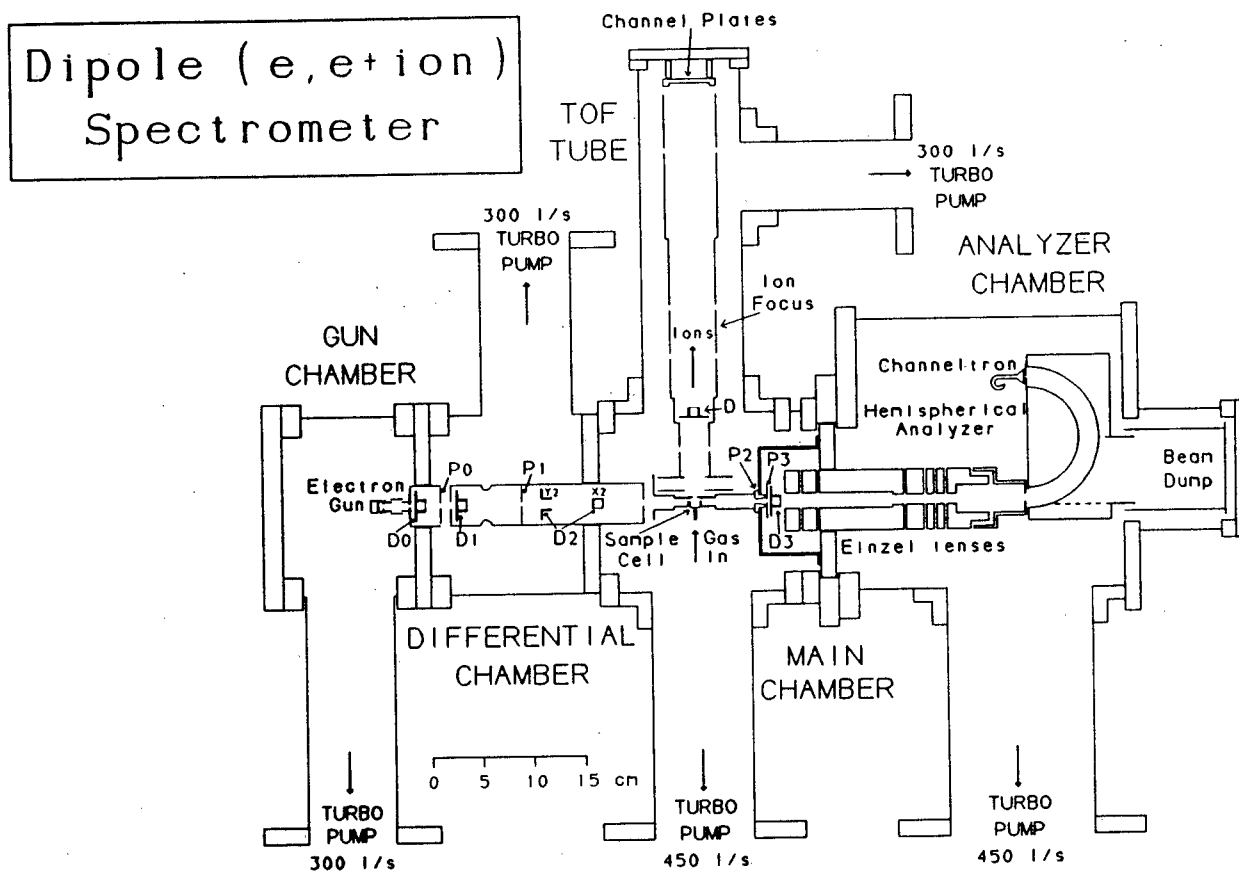
Figure 3.1. Schematic of the low resolution dipole (e,e) and dipole (e,e+ion) spectrometer. For photoabsorption work, this instrument has been used in the dipole (e,e) mode. For the photoionization studies, coincident detection of energy loss electrons and time of flight mass selected ions in the dipole (e,e+ion) mode has been employed.

through the exit aperture, and are detected by a channel electron multiplier (Mullard B419AL) which is operated in the saturated pulse counting mode. The system is initially tuned on the main unscattered beam at zero energy loss using an electrometer and the input cone of the channel electron multiplier as a Faraday cup. The energy scale is calibrated by comparison of the obtained spectrum with the convoluted (by 1 eV fwhm) high resolution spectrum obtained on the instrument described in section 3.3.

The various sections of the spectrometer are differentially pumped by five turbomolecular pumps. There are two stages of differential pumping to protect the electron gun and minimize "poisoning" of the oxide cathode when reactive substances are used [7, 27]. The electron guns must be replaced periodically due to gradual degradation in performance. In addition the collision region, the forward analyzer and the TOF detector region are separately pumped.

Positively charged ions that are formed during the electron scattering (ionization) events are extracted by an electrostatic field of 400 Vcm^{-1} across the collision region and accelerated to 6 keV. The ions travel down a time-of-flight tube, are focussed by ion lenses, and detected with a double chevron microchannel plate (40 mm diameter, model VUW-8920ES, Electro-Optical Sensors (Intevac)) ion detector, used in the saturated pulse counting mode. The TOF mass spectrometer has a mass resolution (m/Δm) of ~50.

This spectrometer is capable of running two different types of experiments, involving different modes of operation. In the dipole (e,e) mode the forward scattered electron beam is analyzed as a function of energy loss. The relative differential electron scattering cross sections obtained are converted to a relative optical photoabsorption oscillator strength spectrum by multiplying the signal by the known Bethe-Born conversion factor for the spectrometer [3, 19], as described earlier. As mentioned previously, the electron scattering signal decreases rapidly with

energy loss - approximately as the inverse third power of the energy loss. Therefore, in order to handle the very wide dynamic range of signal, the energy loss spectra are typically obtained from a series of overlapping data sets covering the wide energy loss range required for VTRK sum rule normalization. During both data acquisition and background subtraction allowance must be made for the different incident electron currents when matching the different overlapping ranges of energy loss. This change in current is necessary because of the very rapid drop-off of cross section with increase in energy loss. Background subtraction is required to eliminate any effects due to non-spectral electrons and to residual gases at the base pressure of $\sim 1 \times 10^{-7}$ Torr. Typical sample gas pressure, as measured by an ion gauge on the spectrometer housing, was 6×10^{-6} Torr, and this was reduced by 70% for background subtraction runs. At these pressures double scattering is negligible.

The second type of operation, the dipole (e,e+ion) mode, was used to obtain photoionization mass spectra by detection of the fast forward scattered electrons at each particular energy loss (photon energy) in coincidence with the TOF mass analyzed ions. The flight time is proportional to the square root of the mass to charge ratio (m/e) for each ion and is determined from a single-stop, time-to-amplitude converter using the ion signal as the "start" pulse and the delayed electron signal as the "stop" pulse. Attention must be given to the baseline of random coincidences, as this decays exponentially with increasing time. Since low mass ions from dissociative photoionization processes can carry significant kinetic energies of fragmentation, the TOF mass spectrometer has been designed with strong draw-out fields to ensure uniform collection of energetic fragment ions with excess kinetic energies of fragmentation up to 20 eV [25]. TOF mass spectra were obtained for HCl and HBr, at an energy resolution of 1 eV fwhm, from the first ionization threshold up to 260 eV and 90 eV respectively. The branching

ratios for the individual ions formed were obtained by integrating the baseline-subtracted TOF mass spectra which had been corrected for the response function of the ion multiplier (MCP) as a function of m/e [28].

Data acquisition in both the dipole (e,e) and dipole (e,e+ion) modes is controlled by a 286 personal computer. Scanning of the energy loss is achieved under computer control using a D/A converter to drive a voltage programmable power supply. Relative energy loss data are collected by the computer and are multiplied by the instrumental Bethe-Born factor. The data, collected in overlapping segments over different ranges of energy loss, are normalized to each other to give a continuous spectrum and then made absolute by use of either the VTRK (S(0)) or the S(-2) sum rule as described earlier (section 2.4). Analysis of the data is achieved by using a suite of programs written in PASCAL by Dr. G. Cooper of this laboratory.

3.3 High Resolution Dipole (e,e) Spectrometer

A detailed account of the construction and operation of the high resolution dipole (e,e) spectrometer can be found in earlier publications [3, 19, 29]. A brief description of the main features of this instrument, pictured in figure 3.2, follows. The instrument consists of four chambers, each differentially evacuated by a turbomolecular pump to a base pressure of $\sim10^{-7}$ Torr. The electron gun, an oscilloscope gun body (Cliftronics CE5AH) equipped with a thoriated tungsten filament, is used as the electron beam source, and is floated at -3 keV with respect to the collision chamber, which is at ground potential. The electron beam is decelerated (typically to 10 or 30 eV) to pass through the hemispherical monochromator, which serves to reduce the energy spread of the primary beam, thus selecting a narrow range (in the range 0.03-0.07 eV fwhm) of the initial Maxwell-Boltzmann distribution ($\sim$0.9 eV fwhm) of electron energies. The monochromated electron beam is re-accelerated to 3 keV and scattered off the sample gas in the

collision chamber. Typical sample gas pressures were ~ 7×10^{-6} Torr. Each data collection run was followed by a reduced pressure run with pressures of ~ 2×10^{-5} Torr to be used for background subtraction. After passing through the collision chamber, electrons scattered in the forward direction are retarded before energy-selection in the hemispherical electron analyzer at a constant pass energy. The overall energy resolution used for valence shell studies is 0.048 eV fwhm at 10 eV pass energy. For inner shell studies a resolution of 0.098 eV fwhm (at 30 eV pass energy) is used. Careful fine-tuning of the instrument is necessary to maintain the high resolution. The energy loss is added to the complete analyzer and detector systems using a computer controlled linear ramp voltage to drive a programmable power supply. The energy loss range of this spectrometer is presently limited to the region below 100 eV and this generally precludes use of the VTRK sum rule for normalization of high resolution data. The selected electrons pass through the analyzer exit aperture (with most of the remaining beam going to the beam dump) and are detected by a channel electron multiplier (Mullard B419AL) operating in the pulse counting saturated mode.

The energy scale of the high resolution instrument is calibrated by introducing approximately equal partial pressures of helium and the sample gas into the collision chamber and referencing to the $1\ ^1S \rightarrow 2\ ^1P$ transition of He which occurs at 21.218 eV [30]. Such corrections are normally less than 0.030 eV.

The high resolution data is collected by a 386 personal computer, multiplied by the known
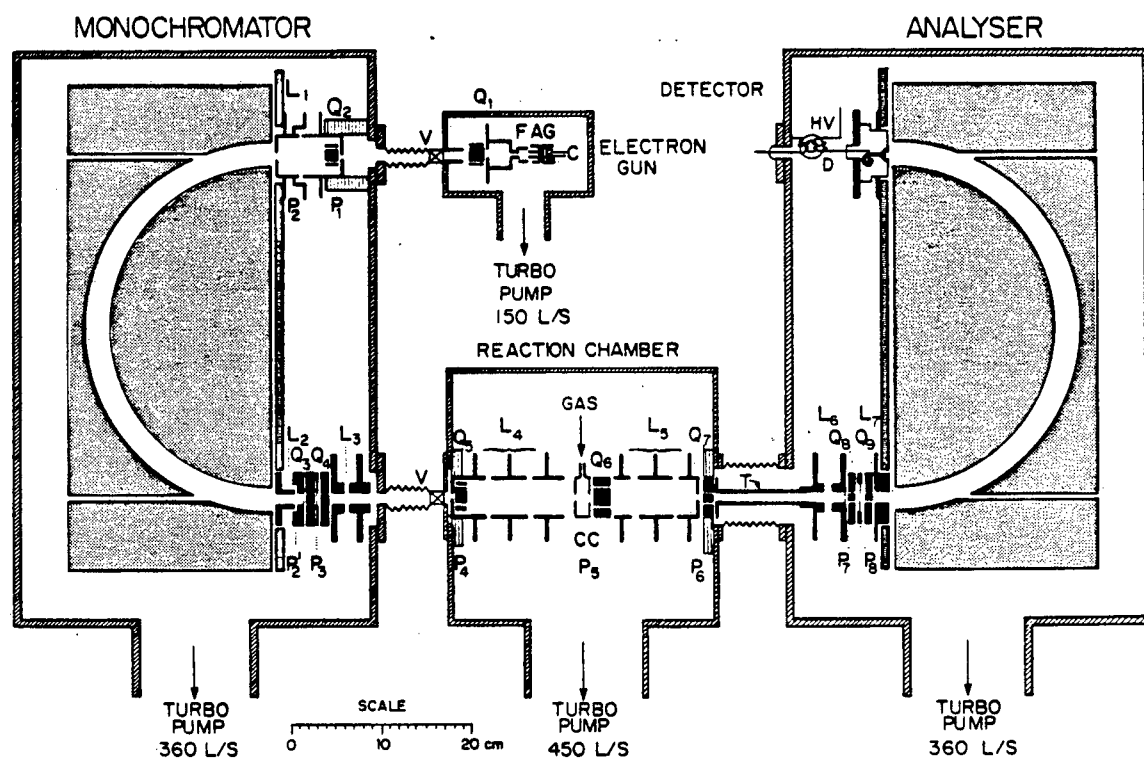
Figure 3.2. Schematic of the high resolution dipole (e,e) spectrometer

instrumental Bethe-Born factor, and background subtracted. This is achieved using software written by Dr. G. Cooper. Thus the collected high resolution EELS spectrum is converted to a relative photoabsorption oscillator strength spectrum, which is made absolute either by normalizing it in the smooth continuum region to the absolute low resolution oscillator strength spectrum obtained from the low resolution instrument, or by using the S(-2) sum rule [7, 21, 31] and a known value of the dipole polarizability.

Chapter 4

Photoabsorption and Photoionization Studies of Hydrogen Chloride

4.1 Introduction

Absolute cross-sections (oscillator strengths) for the photoabsorption and photoionization of hydrogen chloride in the vacuum UV and soft X-ray regions are of interest in many areas of science and technology. Various chloride compounds are involved in etching and growing, and hydrogen chloride is an important molecule in plasma processing [32]. Chloride compounds are also important in interstellar and atmospheric chemistry [33]. HCl is of interest as a major constituent or by-product of some gas discharge and chemical laser systems [34]. Previously published absolute photoabsorption measurements using direct optical methods cover only limited energies in the valence and Cl 2p regions. The present work is the only data set providing photoabsorption and photoionization oscillator strengths (cross sections) over the energy range from 5 to 280 eV, covering the valence shell and Cl 2p inner shell regions. Earlier low resolution dipole (e,e) absolute photoabsorption (5 to 60 eV) and photoionization (up to 40 eV) measurements (see below) have been reported [10], but the accuracy of the results is somewhat in doubt due to limitations in instrumentation and measurement procedures used at the time. These limitations have since been overcome [7, 27].

The electronic spectrum of HCl has been investigated in a variety of experimental studies using direct optical techniques. Previously published valence shell *absolute* photoabsorption oscillator strengths have been obtained in the 170 to 230 nm (5.4 - 7.3 eV) range [35, 36], in the 1050 - 2150 Å (5.8 - 11.8 eV) region [37], from 106 to 185 nm (6.7 - 11.7 eV) [33], and in the 980 - 720 Å (12.65 - 17.22 eV) range using synchrotron radiation [38]. The Cl 2p inner shell of HCl has also been investigated by Hayes and Brown [39], who used synchrotron radiation in the

$L_{3,2}$ edge region for HCl from 196 to 210 eV to obtain absolute cross sections. In other synchrotron radiation work Ninomiya et al. measured absolute cross sections of HCl in the range between 198 and 280 eV [40].

A number of *relative* photoabsorption studies of HCl have been previously published, using direct optical techniques in the valence shell region below 20 eV excitation energy [41, 42]. The absorption [43, 44] and emission [45] spectra of HCl have been the subject of several studies at photon energies below 10 eV. Relative intensities in electron energy-loss spectra below 20 eV have also been published by Wang et al. [34], who measured the electron energy-loss spectrum of HCl from 5 to 19 eV, with an incident electron energy of 200 eV and scattering angles of 0° to 19°. York and Comer [46] studied both dipole and non-dipole transitions in the energy range from 9 to 16.5 eV using a spectrometer with a range of impact energies from 10 to 120 eV and scattering angles from 0° to 90°. Shaw et al. [47] measured the energy-loss spectrum of HCl in the outer valence (8 - 18 eV) and Cl 2p (198 - 205 eV) regions with an incident energy of 1500 eV and 0° scattering angle.

HCl has been the subject of a previous photoionization study [48] in the energy range below 21 eV, but no absolute measurements were reported. Photoelectron spectroscopy (PES) studies of the binding energy spectrum of HCl, determined using the 584 Å resonance line of helium (HeI) have also been reported [49, 50]. More recently the photoelectron spectrum of HCl up to 40 eV binding energy was reported by Adam [51], by Svensson et al. [52] and by Will et al. [53] using synchrotron radiation. Faegri and Kelly [54] have reported calculations of absolute partial cross sections for photoionization from the 2π and 5σ orbitals of HCl.

In the earlier work on HCl in 1984 in this laboratory, the low resolution (1 eV fwhm) absolute photoabsorption (7-60 eV) oscillator strengths and partial photoionization oscillator

strengths for molecular and dissociative photoionization as well as for production of the electronic

ion states (up to 40 eV) have been obtained [10], using dipole (e,e), dipole (e,e+ion) and dipole

(e,2e) spectroscopy respectively. However, possible problems with a few [7] earlier low

resolution dipole (e,e) photoabsorption measurements have since been discovered in the cases of

SiH_4 [27], C_2H_4 [31], C_2H_2 [55], and freons [56]. In these cases the target gases have been found

to have had a significant pressure dependent effect on the electron gun emission characteristics,

due to a poisoning effect on the oxide cathode used in the low resolution dipole (e,e)

measurements. It is now known that when such spurious effects are present, serious errors can

occur in the background subtraction procedures (and thus in the shape and magnitude of the

resulting oscillator strength spectrum) due to the significant change in operating pressures. These

problems have since been overcome by the installation, in 1991, of an additional differential

pumping stage between the electron gun chamber and the collision chamber [27]. Similarly the

background subtraction procedures have been further refined and improved [3]. Thus there is

some doubt as to the reliability of the previous low resolution photoabsorption and

photoionization oscillator strength determinations for HCl [10]. An additional consideration in

the earlier HCl work [10] concerns the data analysis procedures and in particular the

normalization of the data, in which the VTRK sum rule was used without taking into account the

small correction (~ 4%) due to Pauli-excluded transitions (see section 2.4). Furthermore no

attempt was made to fit and extrapolate the data to infinite energy. Rather the spectrum was

simply integrated up to the rather low energy limit of the data at 60 eV. Extrapolation from 60

eV to infinity and the neglect of the Pauli excluded correction will have opposing effects on the

oscillator strength scale estimated by the VTRK sum rule. Thus the resulting absolute scale [10]

should have been reasonably accurate, although the magnitude of the Pauli excluded correction is expected to be somewhat smaller than the effect of data truncation at 60 eV. It is important to note that any errors in the total photoabsorption differential oscillator strength would also be reflected in the partial photoionization oscillator strengths (PPOS's) for molecular and dissociative photoionization (see equation 2.3.3) as well as those for producing electronic ion states (see equation 2.3.5). Furthermore the efficiencies of the ion detectors have since been calibrated [28] with respect to different m/e (i.e., mass to charge) values.

For the above reasons the previous dipole (e,e) and (e,e+ion) studies of HCl have been re-investigated in the present work with the modified (i.e. differential pumping and calibrated ion detector) low resolution dipole (e,e) and (e,e+ion) spectrometer and with improved data processing procedures, incorporating extrapolation to infinite photon energy and correction for Pauli excluded transitions. Furthermore the valence shell photoabsorption and photoionization data have been considerably extended to 195 eV and 85 eV respectively. In addition, photoabsorption and photoionization studies have also been carried out in the Cl 2p inner shell region from 195 to 280 eV. In further new work the absolute photoabsorption oscillator strength spectrum has been obtained in both the valence and Cl 2p inner shell regions with the high resolution (0.05 eV fwhm) dipole (e,e) spectrometer (see section 3.3) which was developed some years after the original low resolution studies were reported [10].

The interpretation of the electronic spectrum of HCl has been believed to be relatively simple with most states being assigned to Rydberg transitions [57]. The ground state vibrational structure has been investigated by Huber and Herzberg [58] and by Terwilliger and Smith [41]. The lowest four vibrational levels of the $B^1\Sigma^+$ state and their rotational structure have been recorded in emission studies [45] in the 2000Å region, i.e., transitions to high vibrational levels of

the $X^1\Sigma^+$ ground state. Tilford et al. [44] have identified the lowest Rydberg states $b^3\Pi_i$ and $C^1\Pi$ and higher Rydberg species [43], in particular the $f^3\Delta$ state. Hirst and Guest [59] and Bettendorf et al. [57] have reported ab initio calculations on the excited states of HCl below 12 eV. The present work addresses mainly the question of absolute transition probabilities (oscillator strengths) rather than assignments. The assignments shown in figures 4.4 and 4.6 are taken from references [41, 47]. Further progress on the assignments will require high quality calculations of both transition energies and oscillator strengths. The present work provides the latter data.

4.2 Results and Discussion

4.2.1 Electronic Structure

The ground state electron configuration of HCl in the independent particle approximation can be expressed as:

$$(1\sigma)^2 \quad (2\sigma)^2 \quad (3\sigma)^2(1\pi)^4 \quad (4\sigma)^2(5\sigma)^2(2\pi)^4 \quad (6\sigma)^0$$

| Cl 1s | Cl 2s | Cl 2p | Valence | Virtual Valence |
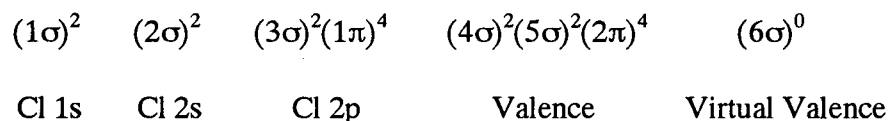
Lempka et al. [49] reported the values of the ionization potentials of the 2π and 5σ outer valence orbitals to be 12.74 ($X^2\Pi_{3/2}$), 12.82 ($X^2\Pi_{1/2}$), and 16.23 ($A^2\Sigma^+$) eV using HeI high resolution photoelectron spectroscopy. Svensson et al. [52] have reported the complete XPS valence shell binding energy of HCl up to 55 eV using monochromated Al K_α radiation at a resolution of ~0.6 eV fwhm. In other work, binary (e,2e) spectroscopy (i.e. electron momentum spectroscopy, or EMS) has been used by Suzuki et al. [60] to investigate the full valence shell binding energy spectrum of HCl, including the inner valence (4σ) region at low resolution (2 eV fwhm). Further slightly higher resolution EMS spectra have been reported by Hollebone et al. [61]. Shaw et al. [47] have reported ionization potentials for the Cl 2p inner shell to be 207.40 eV ($2p_{3/2}$) and 209.03 eV ($2p_{1/2}$).

4.2.2 Photoabsorption Oscillator Strengths

4.2.2.1 Low-Resolution Photoabsorption Measurements

The low resolution (1 eV fwhm) relative oscillator strength spectrum in the energy range 5 to 280 eV was obtained from the Bethe-Born converted EELS spectrum (see section 2.1) and was put on an absolute scale by using the VTRK sum-rule, as described in section 2.4. The resulting absolute photoabsorption oscillator strength spectrum covering extensive ranges of the valence and Cl 2p spectra is presented in figure 4.1. The low resolution oscillator strengths are given numerically in table 4.3. The higher energy region of the valence shell spectrum (85-198 eV) was fitted to a polynomial curve of the form:

$$df/dE = AE^{-2} + BE^{-3} + CE^{-4} \qquad (4.1)$$

where E is the energy loss, A, B, and C are the best-fit parameters which were determined to be

$$A = 1.6662 \times 10^4 \, eV^1 \qquad B = -9.9539 \times 10^5 \, eV^2 \qquad C = 1.3954 \times 10^7 \, eV^3.$$

Thus the contribution to the valence shell region above 198 eV was estimated by extrapolation of the fitted curve to infinite energy. The percentage of the total valence shell oscillator strength in the region from 198 eV to infinity was found to be 8.67%. The absolute oscillator strength scale of the photoabsorption spectrum in the valence shell was obtained by normalizing the area under the Bethe-Born converted EELS spectrum to the number of valence electrons (8) plus a small correction (0.309) for Pauli-excluded transitions, for a total integrated oscillator strength area of
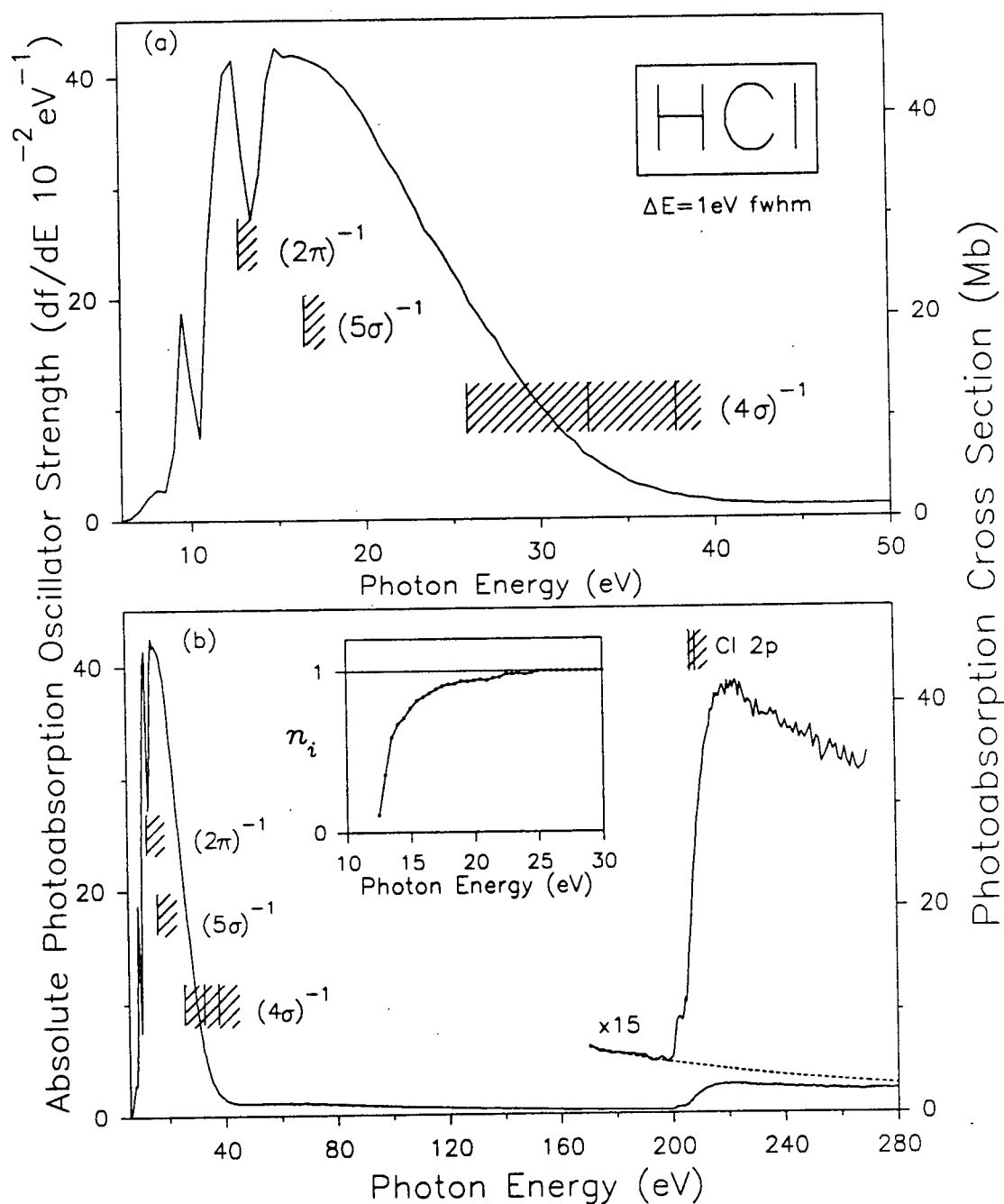
Figure 4.1. Absolute low resolution (1.0 eV fwhm) photoabsorption oscillator strength spectrum for HCl. (a) Valence shell region; (b) Long range spectrum showing the valence shell and Cl 2p inner shell regions. The inset shows the photoionization efficiency (η_i).

8.309. The Pauli excluded correction was obtained by using the value for the atom argon [62], which is isoelectronic with HCl (see section 2.4). The energy scale of the low resolution spectrum was set by comparison with the high resolution spectrum, convoluted with 1 eV fwhm (figure 4.2). It can be seen that the two spectra show very good quantitative agreement over the entire energy range.

As described in section 2.4 above, the S(-2) sum rule can be used to determine the absolute scale of the oscillator strength spectrum. Conversely, the S(-2) sum rule can also be used to obtain the dipole polarizability from the VTRK sum rule normalized absolute spectrum. Thus, from the absolute differential oscillator strength spectrum of HCl, a dipole polarizability of 16.97 a.u. was determined using the S(-2) sum rule. For greater accuracy, the high resolution (0.05 eV fwhm) valence shell spectrum, presented in section 4.2.2.2 below, was used for this determination in the discrete region. The value thus obtained is in good agreement (2.5%) with the experimental values for the static dipole polarizability (α_∞) of 17.4 a.u. [63, 64, 65, 66] and is also in excellent agreement ($\leq 1.5\%$) with values obtained from theory (17.24 a.u. [67], 16.86 a.u. [68]).

In a comparison (see figure 4.3 below) with the present work, the earlier photoabsorption data reported by Daviel et al. [10] using dipole (e,e) spectroscopy are ~20% higher than the oscillator strengths obtained in the present work. This discrepancy is consistent with the differing treatments in the two measurements, of integration to infinite energy and consideration of the Pauli excluded transitions (see comments near the beginning of section 4.1). It has been found in the present work that the Pauli excluded transitions contribute less than 4% to the total integrated oscillator strength, compared to the ~26% contribution from the integration from 60 eV (the limit
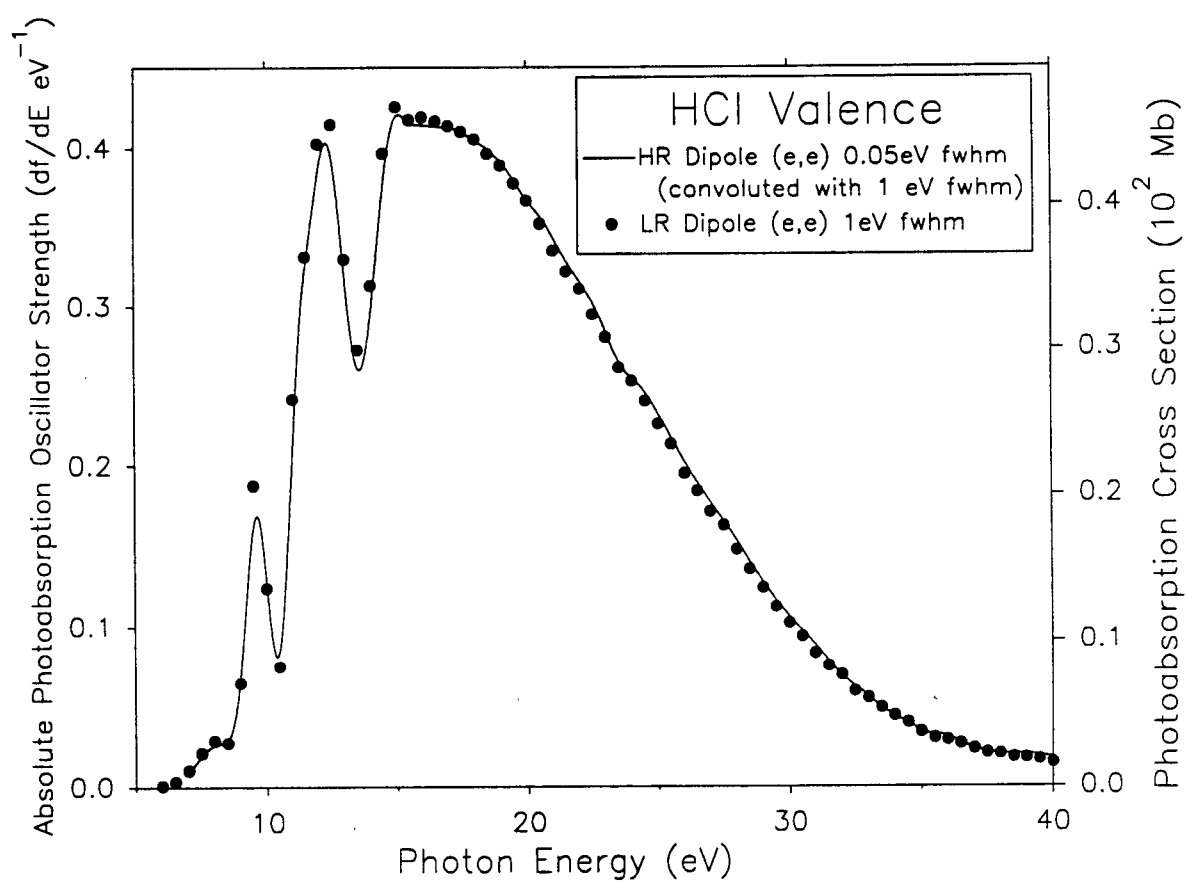
Figure 4.2. Comparison of low resolution (1.0 eV fwhm) and high resolution (0.05 eV fwhm, convoluted with 1 eV fwhm) valence shell photoabsorption measurements obtained in the present work.
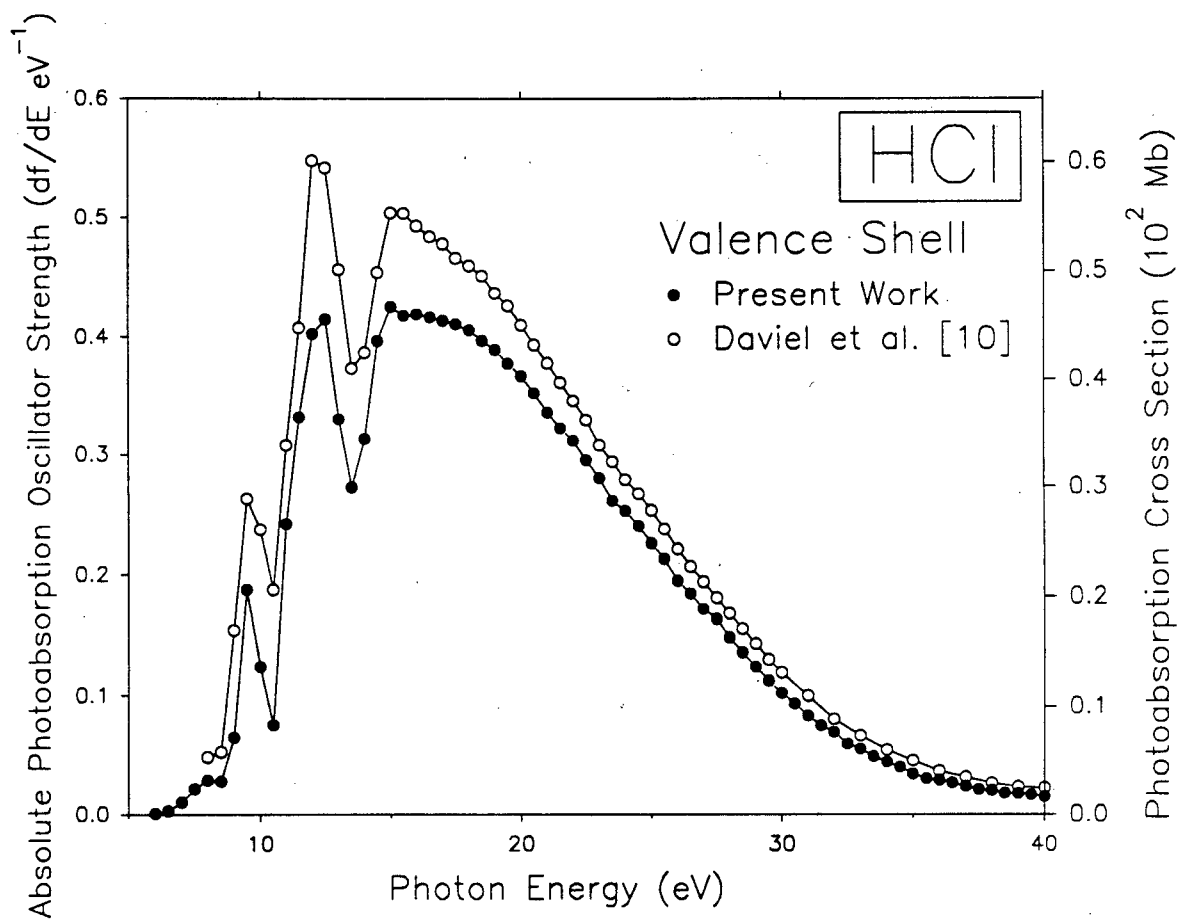
Figure 4.3. Comparison of low resolution absolute photoabsorption oscillator strengths for HCl obtained in the present work and by Daviel et al. [10].

of the earlier data [10]) to infinite energy. Neglect of both these latter contributions would have the net effect of increasing the absolute oscillator strength for the data of reference [10] by ~22% relative to the present work.

Due to the low energy resolution (1 eV fwhm), the spectrum presented in figure 4.1(a) exhibits very little discrete structure. Three broad peaks are observed with maxima at approximately 9, 13, and 15 eV, respectively. Also, a shoulder is visible ~ 8 eV. The discrete region is shown in much greater detail in the high resolution spectrum discussed in section 4.2.2.2 below. A large percentage (70 %) of the valence shell oscillator strength is located below the Cooper minimum, which is at ~40 eV [69]. Figure 4.1(b) also shows the Cl 2p inner shell spectrum in the region above ~ 200 eV. The pre-edge discrete structure is shown in detail in the significantly higher resolution spectrum in figure 4.6 below and discussed in section 4.2.2.3. The oscillator strength rises steeply at the Cl $2p_{3/2,1/2}$ ionization edges and the continuum levels off out to the limit of the data at 280 eV.

4.2.2.2 Valence Shell High Resolution Photoabsorption Measurements for HCl

The valence shell absolute photoabsorption oscillator strength spectrum is shown at higher resolution (0.050 eV fwhm) from 5 to 18 eV and from 5 to 40 eV in figures 4.4(a) and 4.4(b) respectively. The assignments shown for the discrete transitions on figure 4.4(a) are from reference [41] and the ionization potentials are from high resolution PES measurements [49]. The spectrum was placed on an absolute scale by normalizing the Bethe-Born converted energy-loss data to the low resolution absolute photoabsorption oscillator strength in the smooth ionization continuum region (see figure 4.4(b) and table 4.3). It can be seen from a comparison of the spectra obtained at high and low resolution (figure 4.4(b)), that the shapes of the two spectra are
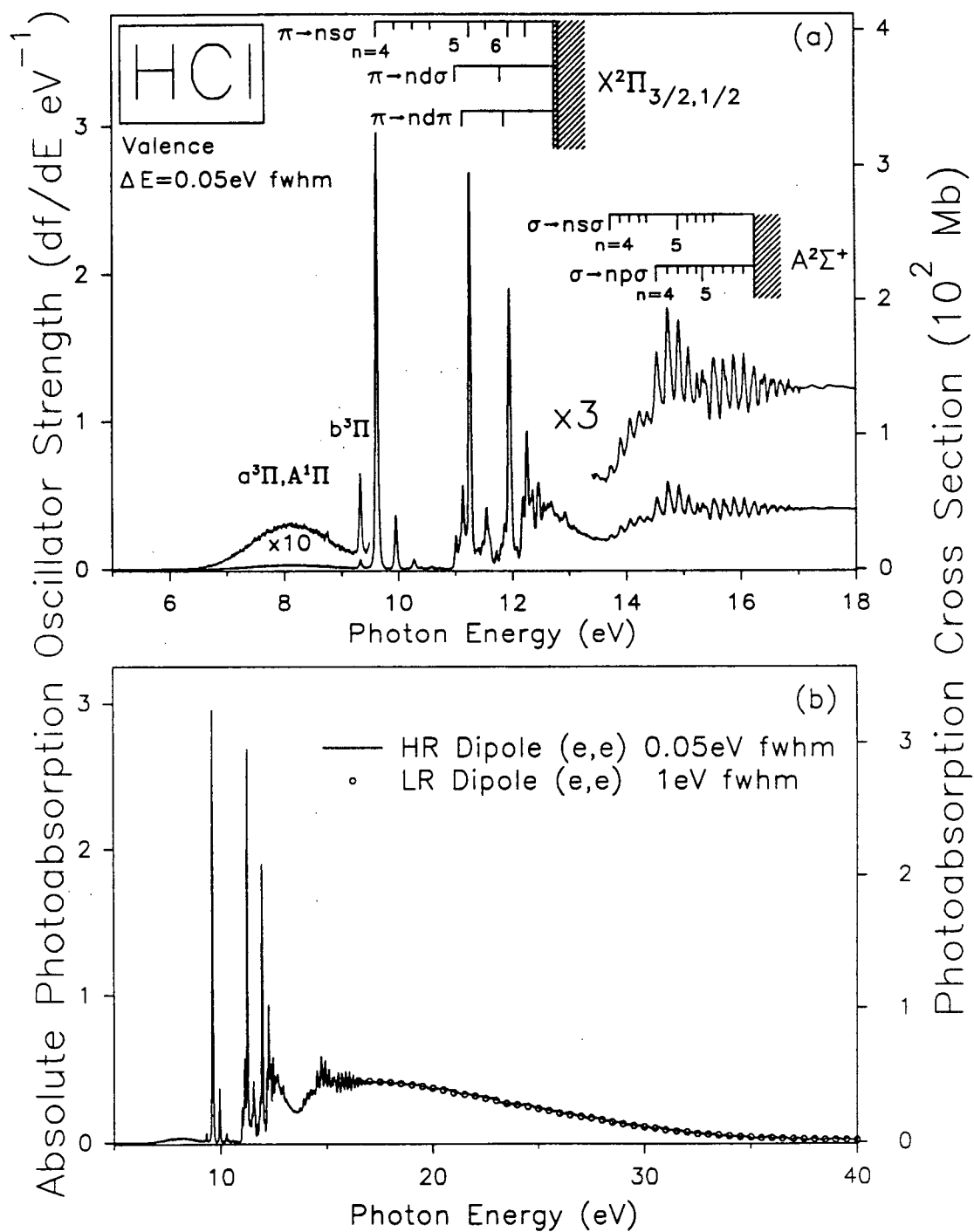
Figure 4.4: Absolute high resolution (0.05 eV fwhm) and low resolution (1.0 eV fwhm)

photoabsorption oscillator strengths (cross sections) for the valence shell of HCl.

the same over the smooth continuum region from 20 to 40 eV. This is a good consistency check of the results, since the high and low resolution dipole (e,e) spectrometers have different impact energies and scattering geometries, and thus different Bethe-Born factors.

As discussed in the introduction, only a few previous studies of the valence shell *absolute* oscillator strength spectrum have been reported, and these only cover small ranges at low energies. Using a Xe_2 discharge lamp Roxlo and Mandl [35] measured the absolute photoabsorption spectrum of HCl from 5.8 to 7.3 eV, and reported absolute cross sections which are significantly (33%) lower than those in the present work, as shown in figure 4.5(a) and table 4.1. Roxlo and Mandl also showed the work of Romand [36], who had earlier reported very similar results. Myer and Samson [37] used direct optical techniques to measure the absolute cross sections of HCl in the region 5.77-11.81 eV, at a resolution of 0.25Å (ΔE ~0.002 eV fwhm). A detailed comparison with the present work is not possible due to the difficulty of integrating the spectrum reported by Myer and Samson [37], which showed a non-linear baseline (due to stray light effects) and truncated peaks as well as large line-saturation errors. The intensity of the broad peak at ~8 eV reported by Myer and Samson [37] is only 5% higher than that found in the present work. However the intensities reported by Myer and Samson [37] in the region of the much narrower Rydberg transitions up to 11.8 eV (the limit of the data in reference [37]) are very different from those in the present work, particularly in the region ~ 11.3 eV where there is clear indication of severely attenuated intensities due to line saturation (i.e. line width/bandwidth interaction) effects in the Beer-Lambert law optical work. The intensities [37] in the region of ~11.3 eV are only a few percent of those obtained in the present work where line saturation effects cannot occur. It is noteworthy in this regard that these large line-saturation
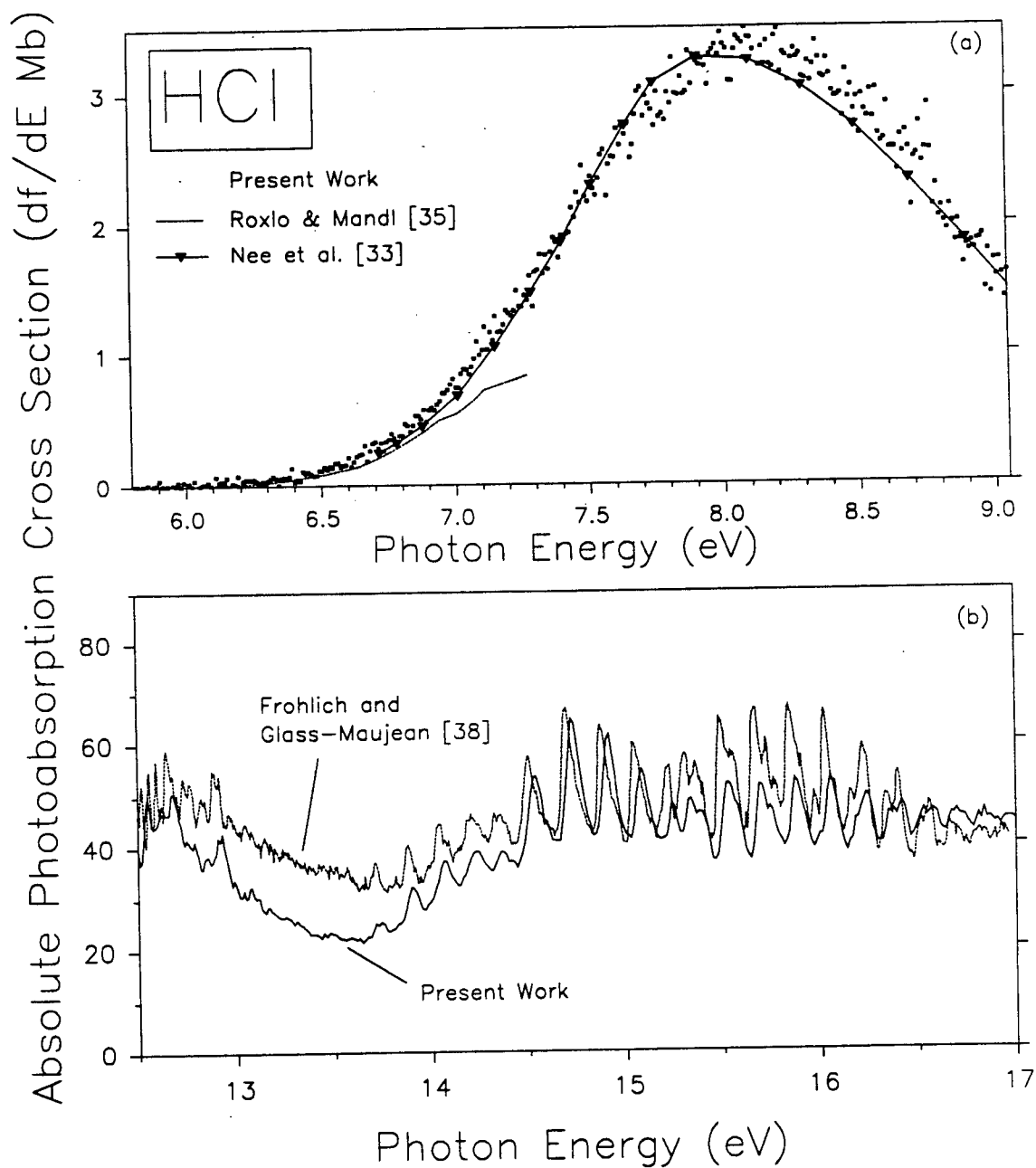
Figure 4.5. Comparison of the present absolute cross sections in the valence shell photoabsorption of HCl with the digitized data from (a) Roxlo and Mandl [35] and Nee et al. [33] and (b) Frohlich and Glass-Maujean [38].

Table 4.1: Integrated oscillator strengths for selected energy regions of the valence and Cl 2p inner shell photoabsorption spectrum of HCl.

Energy Region (eV)	Present Work (Mb)	Literature Values (Mb)	Ref.
5.80- 7.27	0.52	0.31	[35]
		0.31	[36]
6.20- 9.5[a]	5.27	5.11	[33]
9.25-10.8	20.96		
9.3- 9.4	0.40	0.0026[b]	[33]
9.5- 9.7	16.90	0.133	[33]
9.87-10.00	2.22	0.0173	[33]
10.10-10.35	0.62		
10.35-10.80	0.46		
10.90-12.11	46.20		
10.93-11.05	1.37	0.01	[33]
11.05-11.18	4.59	0.0213	[33]
11.18-11.34	15.37	0.032	[33]
11.44-11.67	5.24	0.0056	[33]
11.77-12.11	17.23		
12.11-12.42	14.82		
12.11-17.2	208.1		
198 - 210	11.8	18.06	[39]
200 - 211	13.7	16.97	[40]

[a] Integrated area excluding small peak at 9.32 eV.
[b] This and the following values from Nee et al. [33] are sums of reported oscillator strengths obtained at much higher resolution than in the present work.

errors occur even though the resolution (ΔE ~0.002 eV fwhm) in the optical work [37] is much better than that in the presently reported dipole (e,e) work (0.05 eV fwhm).

In 1986, Nee et al. [33] reported the photoabsorption and fluorescence cross sections of HCl in the valence shell region from 6.7 to 11.7 eV using synchrotron radiation, with an optical monochromator resolution of 0.05 nm (ΔE ~0.005 eV fwhm). It is clear from a comparison of integrated peak areas (Mb) at selected energies (table 4.1) that the cross sections reported by Nee et al. are very much lower (typically by two orders of magnitude) than those obtained in the present work despite the further improved resolution.Evidently the cross sections of the peaks observed by Nee et al. are dramatically reduced by Beer-Lambert law line-saturation effects (see section 1.2 above). Comparison of the broad band between 7 and 9 eV shows a 3% difference between the work by Nee et al. [33] and the present work; this is not surprising since line-saturation effects well not perturb the intensity of such a broad band. A more recent study by Frohlich and Glass-Maujean [38] has reported absolute cross sections with high resolution from 12.65 to 17.22 eV using synchrotron radiation. Their measured cross sections are from ~3 to 50% higher than those reported in the present work (see figure 4.5(b) and table 4.1 above).

4.2.2.3 Inner Shell (Chlorine 2p) High Resolution Photoabsorption Measurements for HCl

The absolute photoabsorption spectrum of the Cl 2p inner shell of HCl was obtained from 198 to 213 eV at 0.1 eV fwhm (figure 4.6(a)) using the high resolution dipole (e,e) spectrometer, in order to examine the discrete excitation region in some detail. The high resolution spectrum was normalized to the low resolution spectrum (figure 4.1(b)) at 198 eV below the first Cl 2p electronic excitation threshold as shown on figure 4.6(a). The assignments on figure 4.6(a) are taken from the work of Shaw et al. [47].
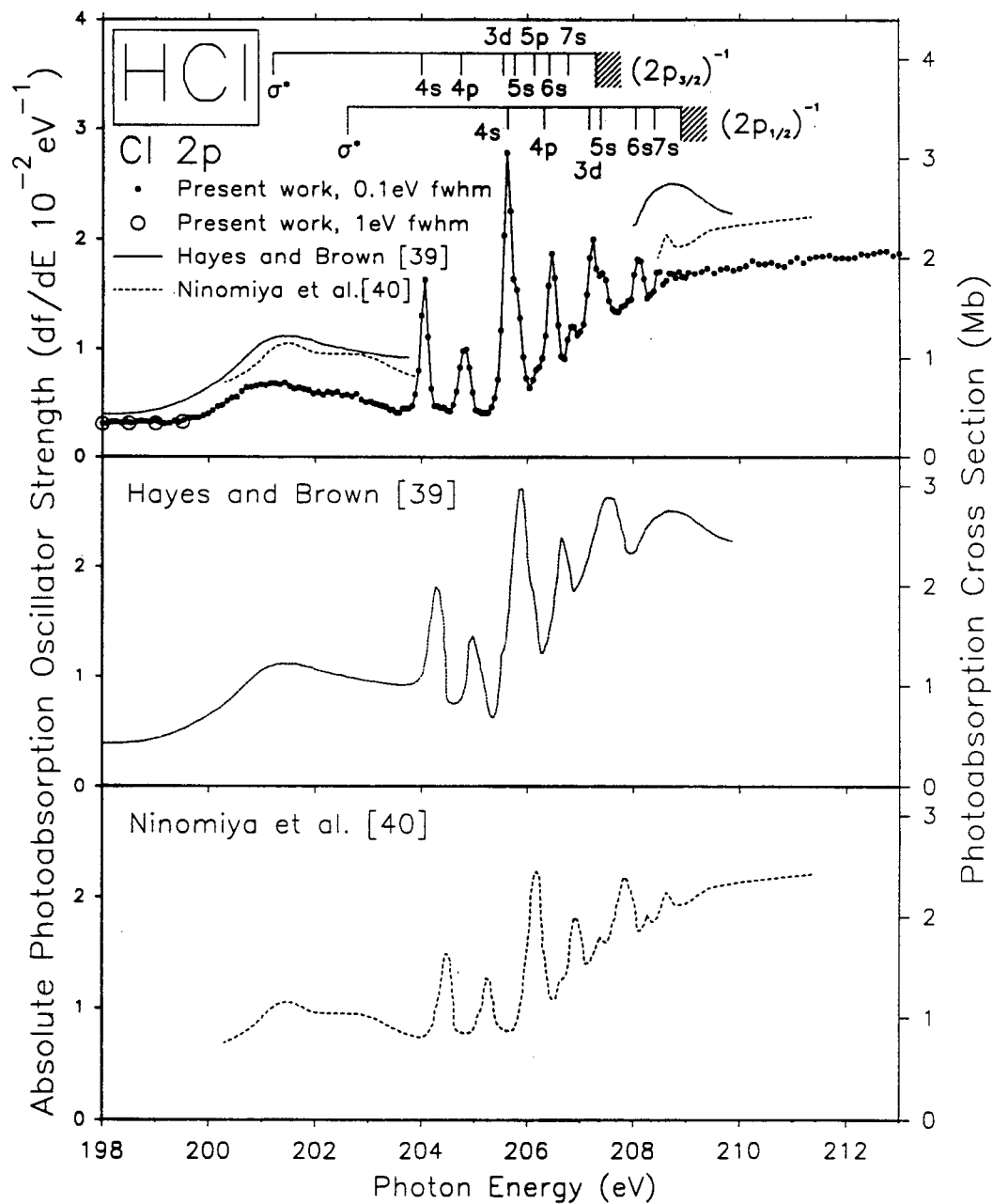
Figure 4.6. Absolute photoabsorption oscillator strength (cross section) for the Cl 2p inner shell

of HCl obtained in the (a) present work and digitized from data reported by (b) Hayes and Brown

[39], and (c) Ninomiya et al. [40]. Peak assignments in (a) are taken from reference [47].

Two previous studies [39, 40] of the *absolute* photoabsorption cross-sections in the inner

shell region of HCl have been reported. Hayes and Brown [39] obtained absolute cross sections

from 198 to 210 eV at 0.16 eV fwhm. The *shape* of the spectrum [39] agrees quite well with that

obtained in the present slightly higher resolution (0.1 eV fwhm) work. However the absolute

cross sections reported by Hayes and Brown [39] typically are 35% higher than those measured

in the present work, as can be seen from the broader features and continuum region in figure

4.6(a,b) and from the numerical data in table 4.1. The results obtained by Hayes and Brown [39]

included corrections for stray light which may have contributed to some of the differences in cross

section, as well as differences in shape with respect to the present work. The second study, by

Ninomiya et al. [40], using synchrotron radiation, reported absolute photoabsorption cross-

sections for HCl between 198 and 280 eV. Although the general shape of the spectrum and

relative intensities agree reasonably well with the spectrum obtained in the present work, (figure

4.6), this data is typically 10-20% lower than the data of Hayes and Brown [39] but still 20-50%

higher in cross section than the present work. Significant differences are also observed in the

energy scales between the spectrum of Hayes and Brown [39], that of Ninomiya et al. [40], and

that obtained in the present work (figure 4.6). The presently reported energy scale is based on the

very accurate valence shell energy calibration (see section 3.3). Ninomiya et al. [40] quote an

uncertainty of ±20% in the cross section at the Cl $L_{2,3}$ edge. It should be noted that the absolute

oscillator strength scale of the presently reported Cl 2p inner shell spectrum has been established

by use of the VTRK (S(0)) sum rule normalization of the valence shell, which gives a very

accurate (within 2%) value of the dipole polarizability of HCl (see section 4.2.2.1) via the S(-2)

sum rule.

4.2.3 Photoionization Studies of HCl in the Valence Regions

Time of flight (TOF) mass spectra for HCl were obtained from 12 to 85 eV in the valence

shell region (figure 4.7) and from 195 to 250 eV in the Cl 2p inner shell region (shown in figure

4.15 below) using the dipole (e,e+ion) spectrometer at 1 eV (fwhm). The relative intensities of

chlorine containing peaks are consistent with the natural relative abundances of ^{35}Cl and ^{37}Cl

(~3:1). The doubly charged ion Cl^{2+} is observed with a (double) ionization potential of 48 eV.

No stable HCl^{2+} is detected in the valence shell photoionization spectra. Table 4.2 shows a list of

the positive ions that were detected in the TOF mass spectra (figure 4.7), together with their

respective mass to charge ratios and appearance potentials. Photoion branching ratios for the

molecular and dissociative ions were determined as percentages of the total photoionization from

integration of the background subtracted TOF peaks. Figure 4.8 presents the photoionization

branching ratios as a function of photon energy for the valence and inner shell, and table 4.4 gives

the photoion branching ratios. As can be seen in figure 4.8, the HCl^+ branching ratio decreases

steeply initially, and levels off around 50 eV. This steep decrease correlates with steep increases

observed in the Cl^+ and H^+ branching ratios, with a similar leveling above 50 eV. The doubly

charged Cl^{2+} appears at 48 eV and likewise levels off above 50 eV. These trends confirm that in

the valence shell continuum the ionic fragmentation pattern of HCl remains constant above the

upper limit of the Franck-Condon region [60, 74] of the $B^2\Sigma$ state of HCl^+. A large change is

observed in the branching ratios in the region of Cl 2p excitation and ionization, indicating the

onset of different ionic photofragmentation processes, which are discussed in section 4.2.5 below.

The branching ratios determined (only up to 40 eV) in the earlier dipole (e,e+ion) study

reported by Daviel et al. [10] are compared with the present results in figure 4.9. The ion

Table 4.2. Appearance potentials (in eV) for molecular and fragment ions resulting from photoionization of HCl.

Appearance Potentials (eV)						
		Dipole (e,e)		**Calculated**	**Experiment**		
Ion	**m/e**	**Present Work**	**Daviel et al.**	**Ref [70]**			
HCl$^+$	37	12.5	13 ± 1	12.474	12.748^a ($^2\Pi_{3/2}$)	12.828^a ($^2\Pi_{1/2}$)	16.254^a ($^2\Sigma^+$)
Cl$^+$	35,36	17.5	17 ± 1	17.44	17.34^b		
H$^+$	1	19	18 ± 1	18.071	14.5^c		
Cl^{++}	17,18	197					
HCl^{++}	19	211			35.5^d		

a: photoelectron spectroscopy [50]
b: photoionization [71]
c: retarding potential difference threshold experiment [72]
d: nth root extrapolation threshold experiment [73]
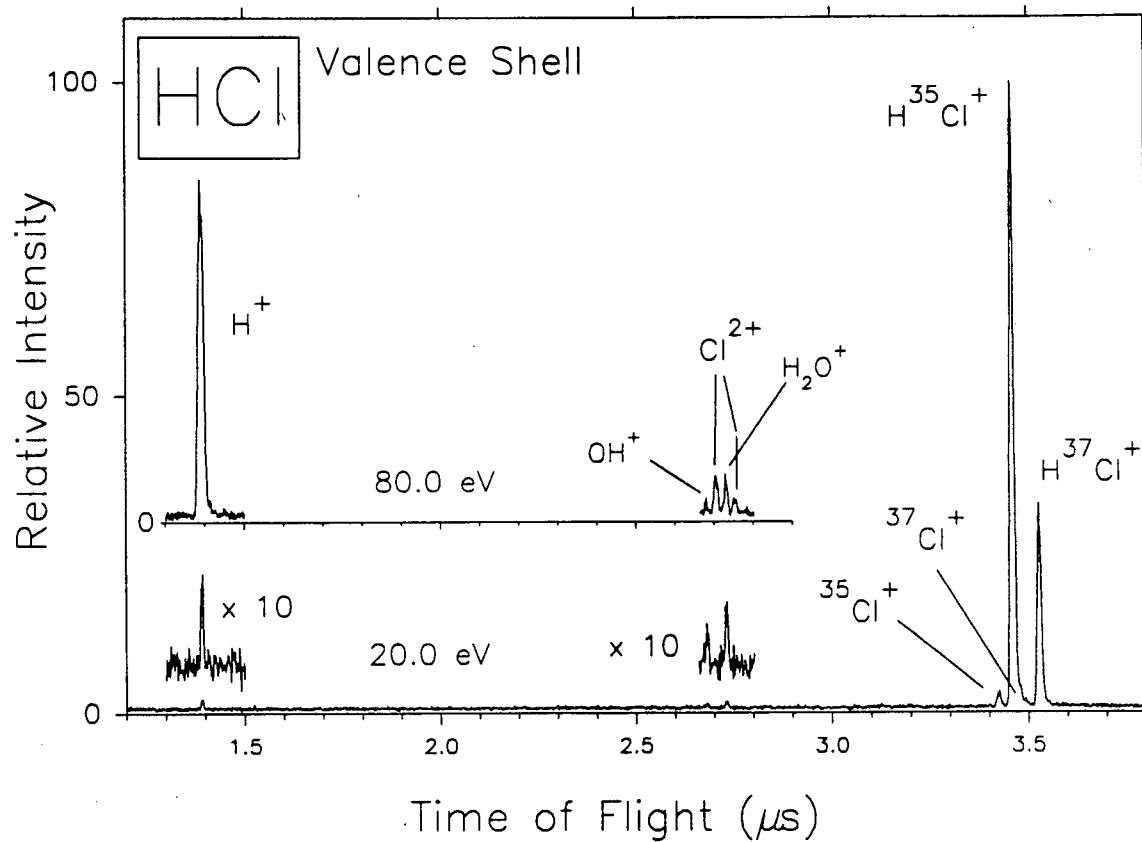
Figure 4.7. Time-of-flight (TOF) mass spectra for valence shell photoionization of HCl at 20.0

eV (lower trace) and 80.0 eV (upper trace).
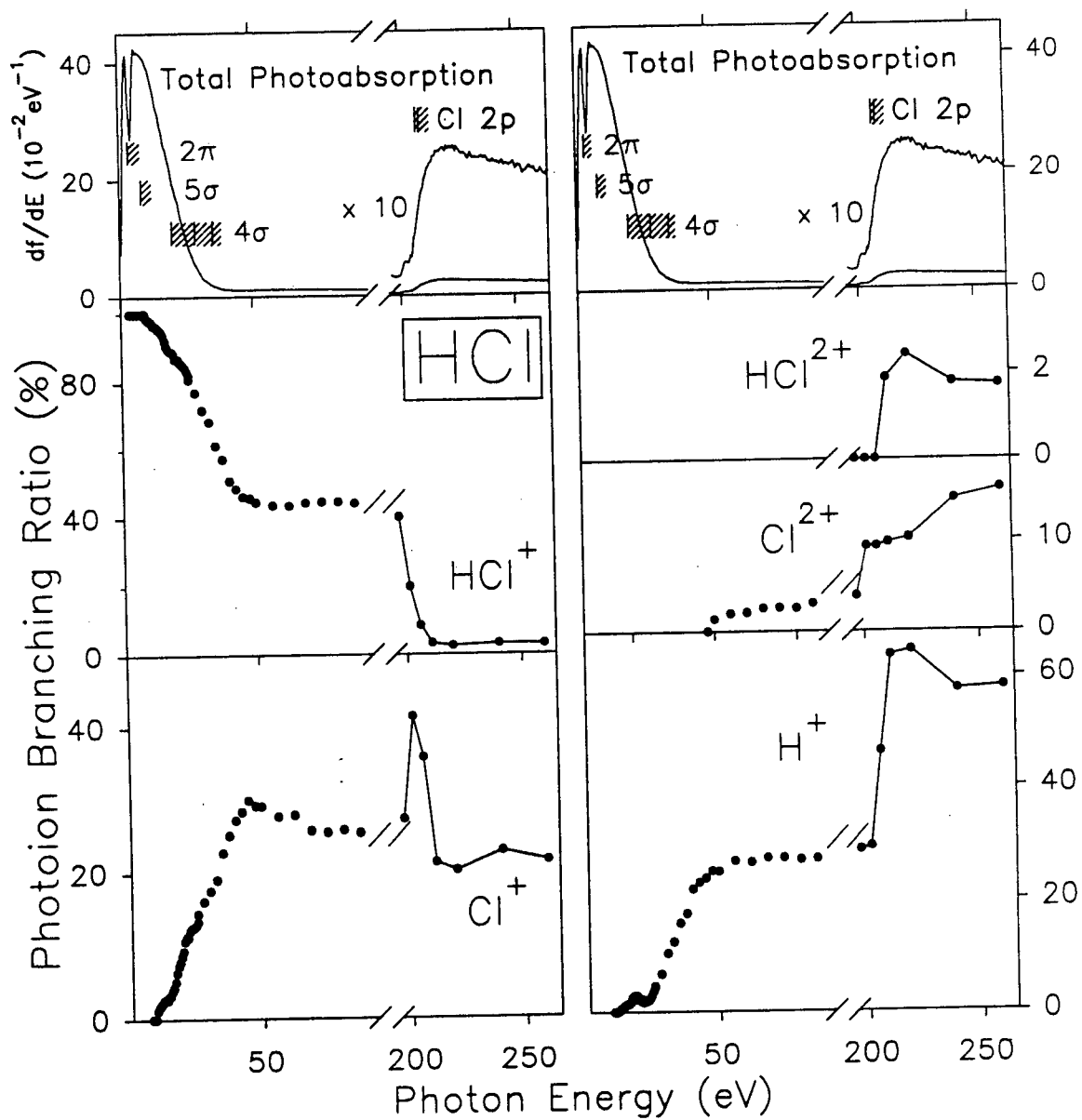
Figure 4.8. Photoion branching ratios (1eV fwhm) for molecular and dissociative ions from photoionization of HCl, as a percentage of total photoionization.
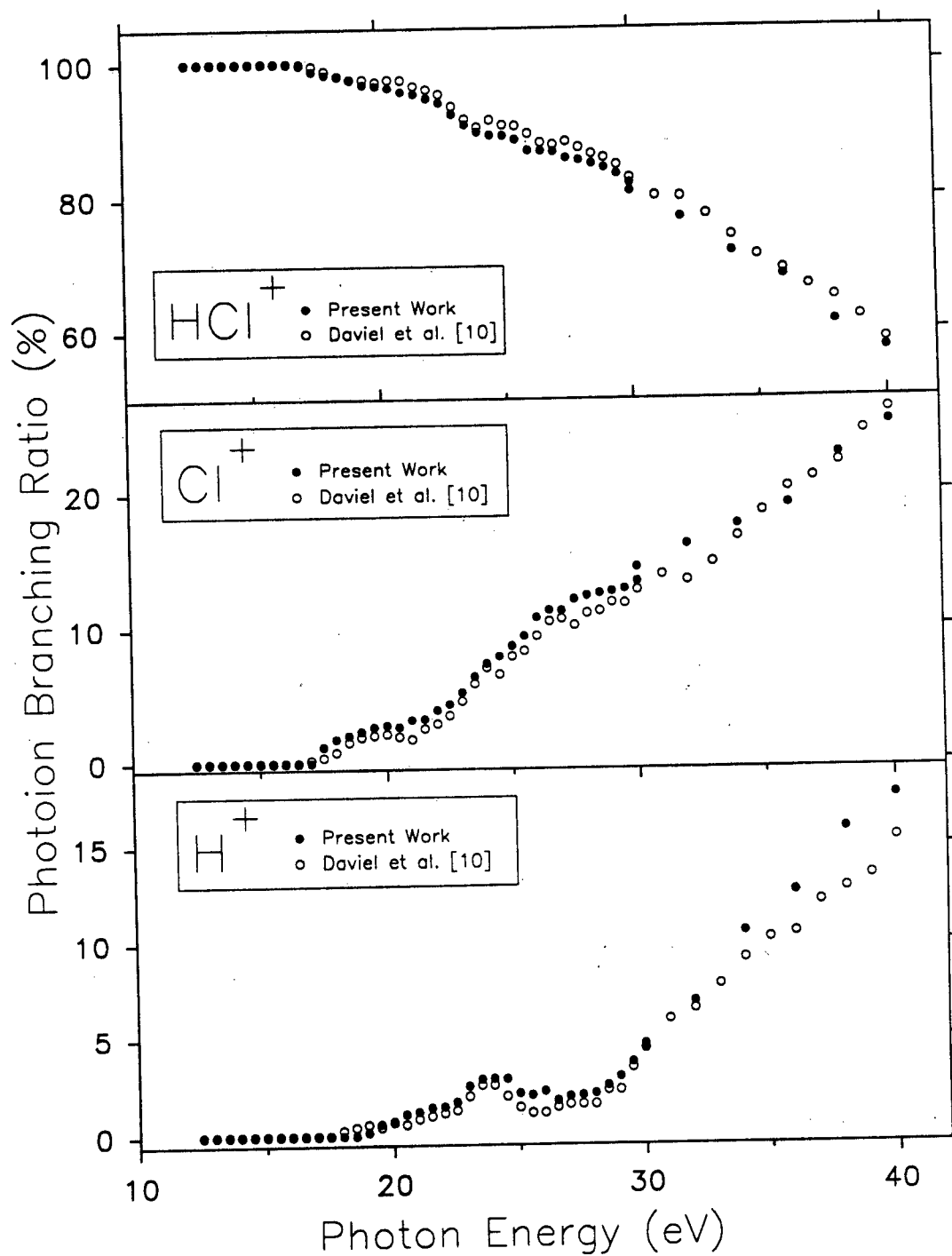
Figure 4.9. Comparison of photoion branching ratios (1 eV fwhm) obtained in the present work and by Daviel et al. [10]. The photoion branching ratios obtained by Daviel et al have been corrected for detector response (see text).

detector used in the previous dipole (e,e+ion) TOF MS studies (a Johnston focused mesh multiplier) was calibrated some considerable time after the 1984 study was published and found to exhibit a slow decrease in sensitivity above m/e = ~ 30 [28]. A correction factor was therefore applied to the previously obtained data for purposes of comparison with the branching ratios obtained in the present work. It can be seen from figure 4.9 that the data from the two studies agree reasonably well. The largest difference can be seen in the branching ratio data for the H^+ ion. The ion detector has since been replaced with a calibrated [28] double microchannel plate (MCP) ion detector which shows considerably improved mass resolution. The MCP ion detector was used for the present work.

Absolute partial photoionization oscillator strengths (PPOS's) for the molecular and each dissociative ion were obtained by taking the triple product of the photoionization efficiency, the photoion branching ratio and the total photoabsorption oscillator strength (see equation 2.3.3) at each photon energy. These PPOS's are shown in figure 4.10 and the numerical values are given in table 4.5. The relative photoionization efficiency, as obtained from the ratio of the total photoionization to the forward scattered energy loss counts at each photon energy, making the reasonable assumption that the ratio of ionic products becomes unity above 25 eV, is shown in the inset to figure 4.1(b). From the valence shell branching ratios, appearance potentials, and the PPOS's for molecular and dissociative photoionization, information regarding the dipole induced breakdown pathways has been obtained.
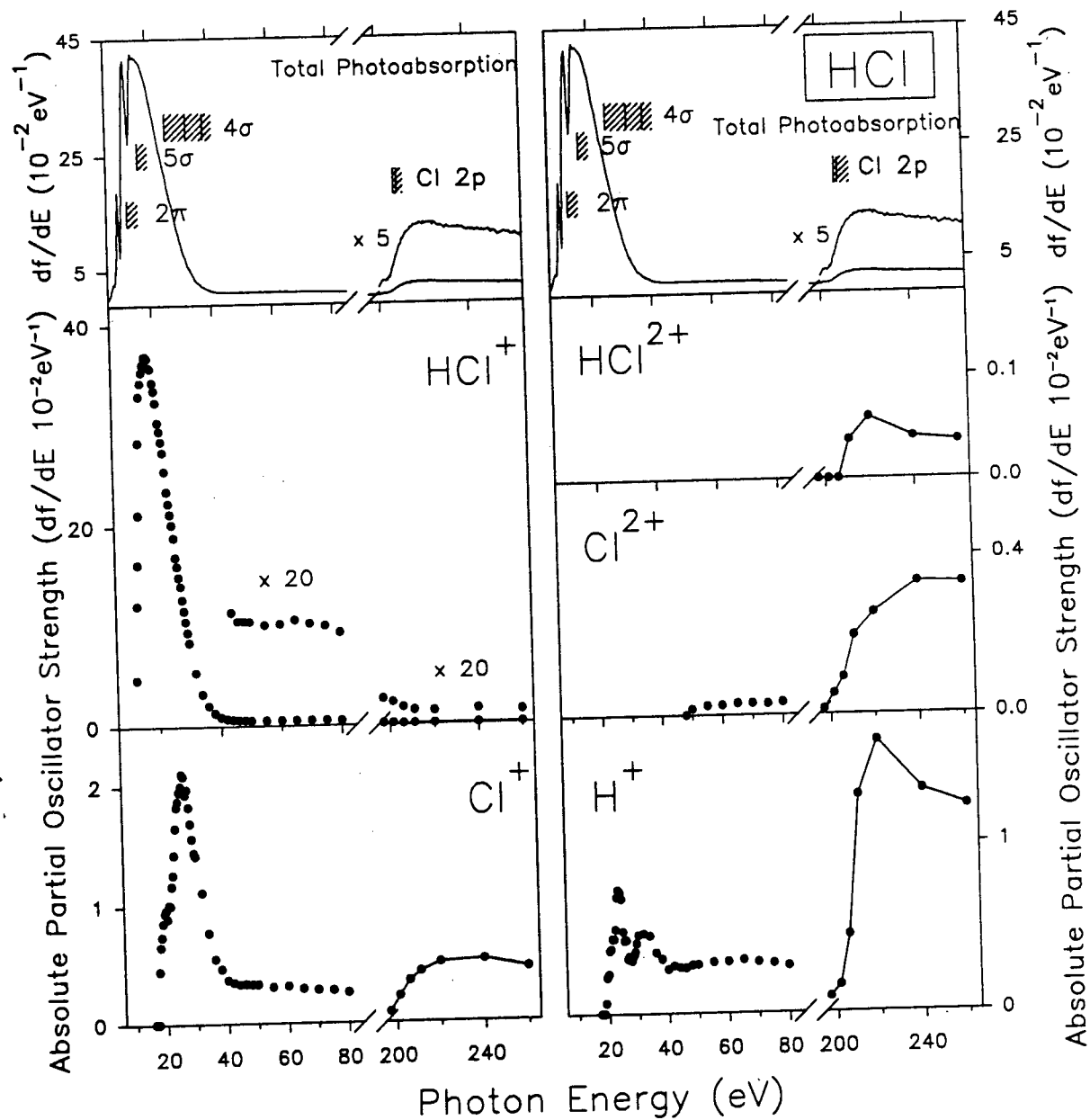
Figure 4.10. Absolute partial oscillator strengths for molecular and dissociative photoionization of HCl from 6 to 265 eV at 1 eV fwhm resolution.

4.2.4 Dipole-Induced Breakdown of HCl

As discussed in section 2.3 (see equations 2.3.4 and 2.3.6), the total absolute photoionization oscillator strength distribution can be partitioned into contributions from the partial oscillator strengths for molecular and dissociative photoionization or into contributions from the electronic ion state partial photoionization oscillator strengths [8]. The latter quantities can be obtained from tunable energy photoelectron spectroscopy (PES), or the equivalent technique of dipole (e,2e) spectroscopy [2, 75]. It has previously been discussed [10] how given ion partial photoionization oscillator strengths can be described as linear combinations of the electronic ion state partial photoionization oscillator strengths or vice-versa. These procedures operate under the assumption that the fragmentation pattern arising from a given ionic state is constant above the upper limit of the Franck-Condon region for a given electronic ion state [8]. The validity of this assumption has been discussed in earlier publications [8, 76], along with a discussion of the conditions under which the assumption breaks down. Complicating factors can arise from (energy localized) autoionization of neutral states, or in the presence of significant direct multiple photoionization processes [8]. The partial oscillator strengths for production of each particular molecular or dissociative ion involve appropriate contributions from the breakdown of the initially formed electronic states of the molecular ion [2, 8, 77], and hence the dipole-induced breakdown for a molecule can be investigated in the valence shell above ~40 eV (the upper limit of the $B^2\Sigma$ Franck-Condon region corresponding to ionization of the most tightly bound valence orbital of HCl). The earlier study [10] in this laboratory investigated the dipole induced breakdown of HCl in the valence shell up to 40 eV by a joint consideration of the absolute photoabsorption and partial photoionization oscillator strengths derived from dipole (e,2e) and (e,e+ion) measurements. For purposes of comparison, in the present work the dipole

(e,2e) photoelectron branching ratios obtained by Daviel et al. [10] have been multiplied by the photoionization efficiencies (see figure 4.1(b)) and the absolute total photoabsorption oscillator strengths (figure 4.1(a)) obtained in the present work. The resulting PPOS's for production of the $X^2\Pi$, $A^2\Sigma^+$ and $B^2\Sigma$ electronic states (figure 4.11 and table 4.6) were then examined together with those for production of HCl^+, Cl^+ and H^+, and from this quantitative information on the dipole-induced breakdown pathways of HCl can be deduced. Also shown in the top panel of figure 4.11 is the complete valence shell low resolution binding energy spectrum as obtained by Suzuki et al. [60] using electron momentum spectroscopy (EMS).

By considering together the appearance potentials (table 4.2) and electronic ion state PPOS's, an attempt has been made to partition the ion PPOS's into contributions from the decomposition of the various ion electronic states. Figure 4.12 shows the best fit for such contributions to the molecular (figure 4.12(b)) and total dissociative ($Cl^+ + H^+$, figure 4.12(c)) photoionization oscillator strengths. The best fit for the molecular ion PPOS is given by the sum ($X^2\Pi + 0.905\ A^2\Sigma^+ + 0.55\ B^2\Sigma$). Below 16.5 eV, formation of the molecular ion HCl^+ is due solely to the $X^2\Pi$ state, whereas at higher energies the $A^2\Sigma^+$ and $B^2\Sigma$ states make further contributions. The PPOS for the total photoionization (i.e. $Cl^+ + H^+$) is well matched by the remaining oscillator strength ($0.095\ A^2\Sigma^+ + 0.45\ B^2\Sigma$) as shown in figure 4.12(c). There is a 1.5 eV difference in the initial onsets of the ionic and electronic state PPOS's, which is to be expected, as can be seen by referring to the binding energy spectrum of HCl [60] shown in the top panel of figure 4.12(a). The predicted contribution from the $A^2\Sigma^+$ state to the total dissociative photoionization cross section is very small (less than 10%), and it can be seen in figure 4.12 that
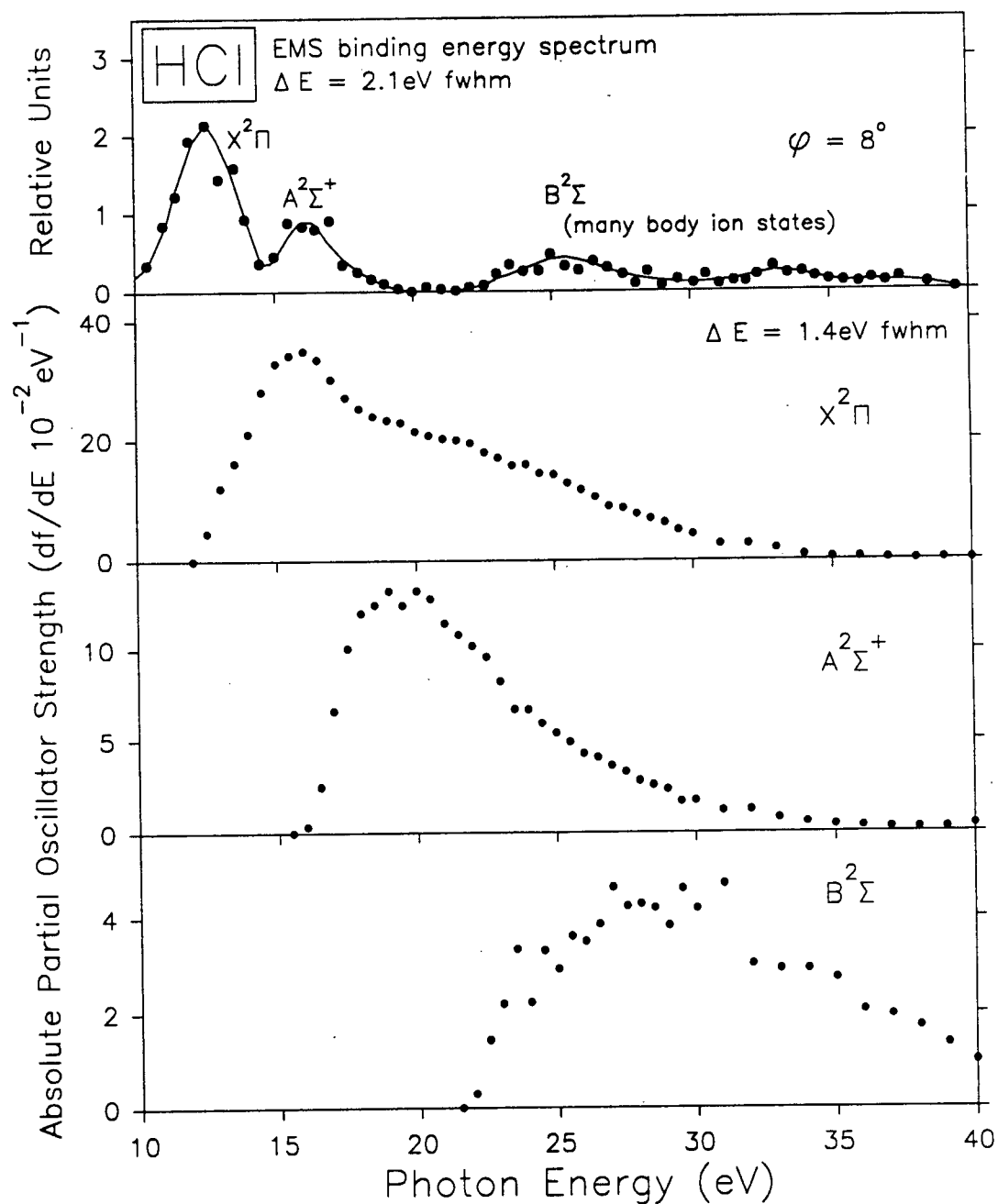
Figure 4.11. Absolute partial photoionization oscillator strengths for production of the $X^2\Pi$, $A^2\Sigma^+$, and $B^2\Sigma$ electronic ion states of HCl^+ (lower three panels). This data has been obtained from the dipole (e,2e) "photoelectron" branching ratios of Daviel et al. [10] together with the presently reported total photoabsorption oscillator strengths and photoionization efficiencies. The top panel shows the valence shell EMS binding energy spectrum of HCl on the same energy scale [60].
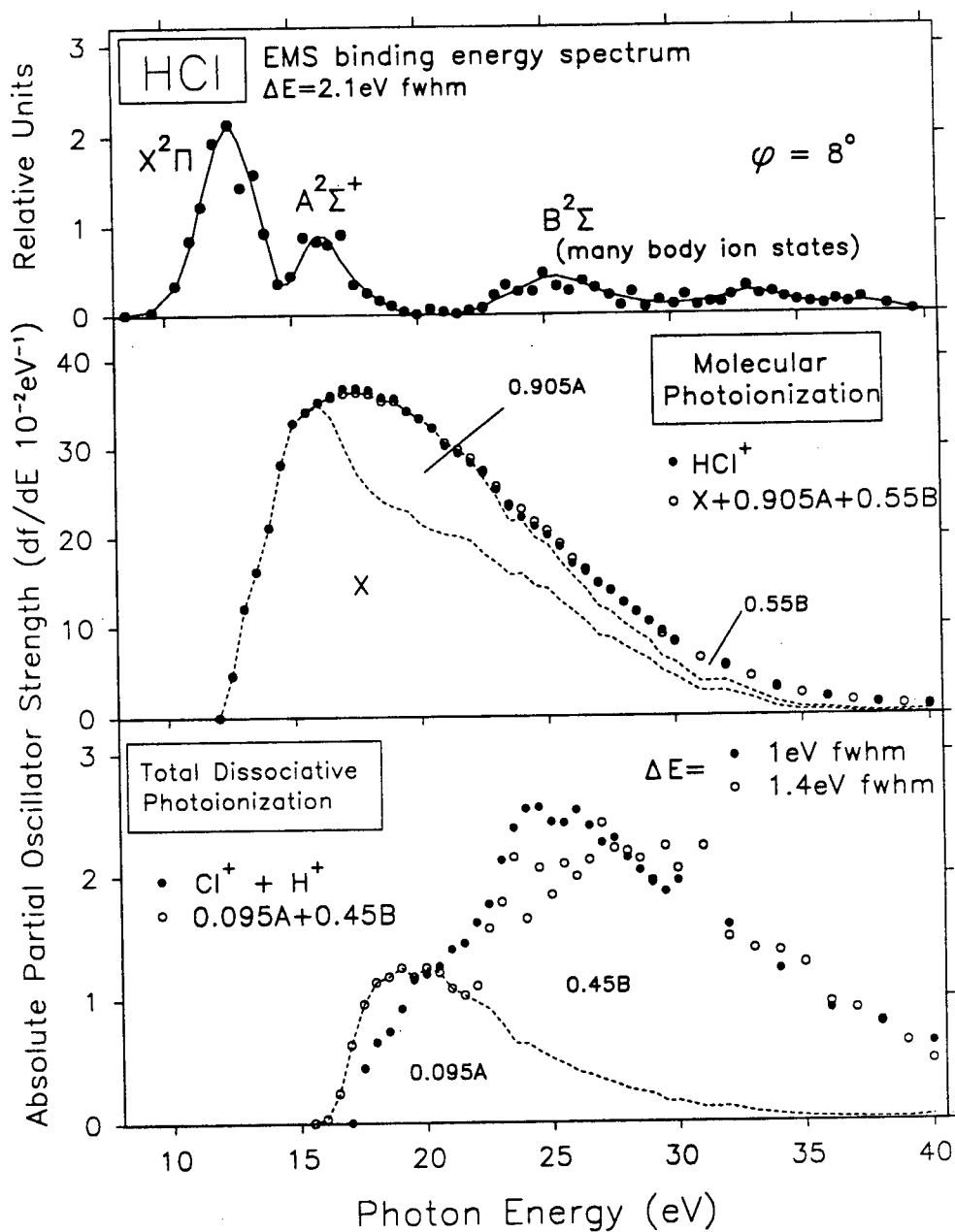
Figure 4.12. Absolute partial oscillator strengths for molecular and total dissociative photoionization of HCl, with best linear combination fits of contributions from the $X^2\Pi$, $A^2\Sigma^+$, and $B^2\Sigma$ electronic state partial oscillator strengths. The top panel shows the EMS binding energy spectrum from reference [60].

this is consistent with the onset of the dissociative ionization oscillator strength coming from the upper tail end of the Franck-Condon region for production of the $A^2\Sigma^+$ state (figure 4.12(a)).

The partitioning of the separate Cl^+ and H^+ partial oscillator strengths into electronic ion state contributions is more difficult, as can be seen in figure 4.13(b,c). For the dissociative ion Cl^+, the best linear combination of electronic states was given by $(0.065\ A^2\Sigma^+ + 0.33\ B^2\Sigma)$. It can be seen that there is a small difference (~1 eV) between the onsets of the Cl^+ and the $A^2\Sigma^+$ PPOS's. Clearly the onset of the dissociative ion Cl^+ is in the upper portion of the $A^2\Sigma^+$ Franck-Condon region, consistent with the major (lower energy) portion going to the molecular ion as discussed above. The sharp rise in Cl^+ oscillator strength above 20 eV clearly corresponds with the onset of the $B^2\Sigma$ electronic state oscillator strength, shown in the binding energy spectrum in figure 4.13(a). As can be seen from figure 4.13(b), there is a significant difference between the Cl^+ PPOS and the $B^2\Sigma$ electronic ion state contribution in the 23 to 30 eV region, which could be due to dissociative autoionization of neutral excited states of HCl down to dissociative states leading to $H + Cl^+$. Above ~30 eV the proposed breakdown linear combination fits very well, as might be expected [8].

The remaining linear combination of electronic ion state contributions, $(0.03\ A^2\Sigma^+ + 0.12\ B^2\Sigma)$, can be seen in figure 4.13(c) to fit the H^+ partial oscillator strength quite well above ~30 eV. The initial onset of H^+ does not correspond with the onset of the $A^2\Sigma^+$ state of HCl^+, similar to the situation for Cl^+ in figure 4.13(b). Again, this is not unreasonable since the H^+ appearance potential indicates that it comes only from the upper energy portion of the $A^2\Sigma^+$ Franck-Condon zone. This is consistent with the small fraction $(0.03\ A^2\Sigma^+)$ predicted by the model. Further contributions to H^+ come from the $B^2\Sigma$ state of HCl^+.
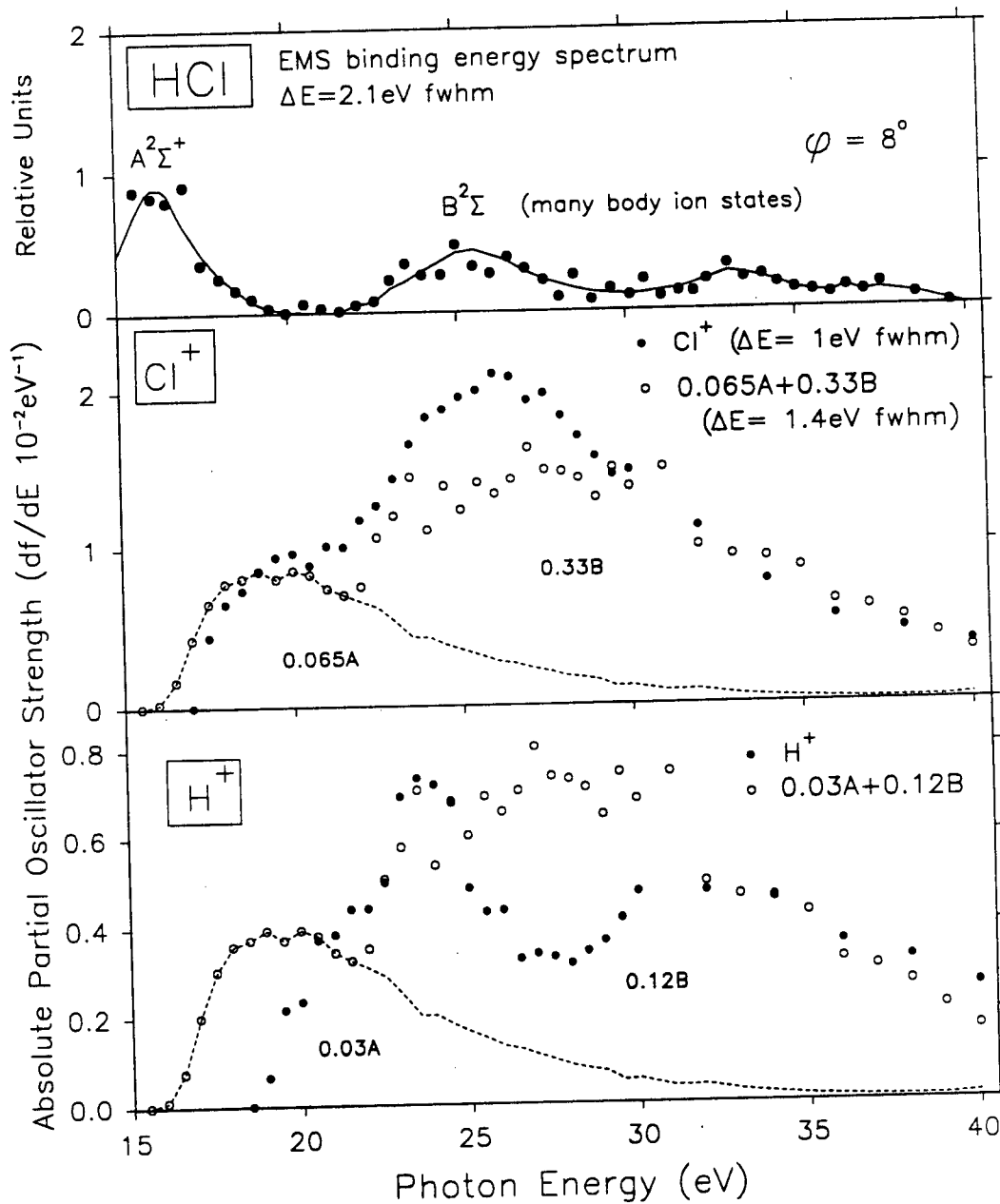
Figure 4.13. Absolute partial oscillator strengths for dissociative photoionization of HCl, with best fit linear combinations of contributions from the $A^2\Sigma^+$ and $B^2\Sigma$ electronic state partial oscillator strengths. The top panel shows the EMS binding energy spectrum from reference [60].

The sharp peak at ~24 eV is most likely due to dissociative autoionization of neutral excited states of HCl, converging on the $B^2\Sigma$ ion state, to give H^+ + Cl. The differences in the 23-30 eV region are understandable due to the "extra" oscillator strength in the Cl^+ PPOS in this region (see figure 4.13(b) and preceding discussion). It is possible that dissociative autoionization processes are the reason for the differences below 30 eV in figures 4.13(b,c). For figure 4.12(c), it can be seen that the overall agreement is much better below 30 eV when the *total* dissociative photoionization is considered. However it should be remembered (see figure 4.13) that the 25-30 eV range corresponds to the Franck-Condon region of the main $B^2\Sigma$ peak of HCl^+, and the breakdown model is therefore not likely to apply strictly in these circumstances [8]. A summary of the dipole breakdown pathways, detailing the electronic ion state contributions to the formation of the molecular and dissociative ions, is shown in figure 4.14.

In the earlier work reported by Daviel et al. [10], the dipole breakdown pathways of HCl were examined, with similar results to those reported in the present work. The $A^2\Sigma^+$ and $B^2\Sigma$ electronic ion state contributions to the molecular ion (HCl^+) PPOS, as reported by Daviel et al. [10], were 3% and 5% *higher*, respectively, than in the present work, while contributions to the total dissociative (Cl^+ + H^+) PPOS were 3% and 5% *lower* than in the present work. These slight differences are understandable in light of the possible problems encountered in the earlier work [10], as discussed above in sections 4.2.2.1 and 4.2.3. In particular, the branching ratio for H^+ obtained in the earlier work [10] was reduced due to decreased response of the ion detector (see section 4.2.3 and figure 4.9). Since the branching ratios are used to determine the PPOS's for production of the ions, a lower PPOS for H^+ was obtained, which thus required smaller contributions from the $A^2\Sigma^+$ and $B^2\Sigma$ electronic ion states. In the present work, more accurate
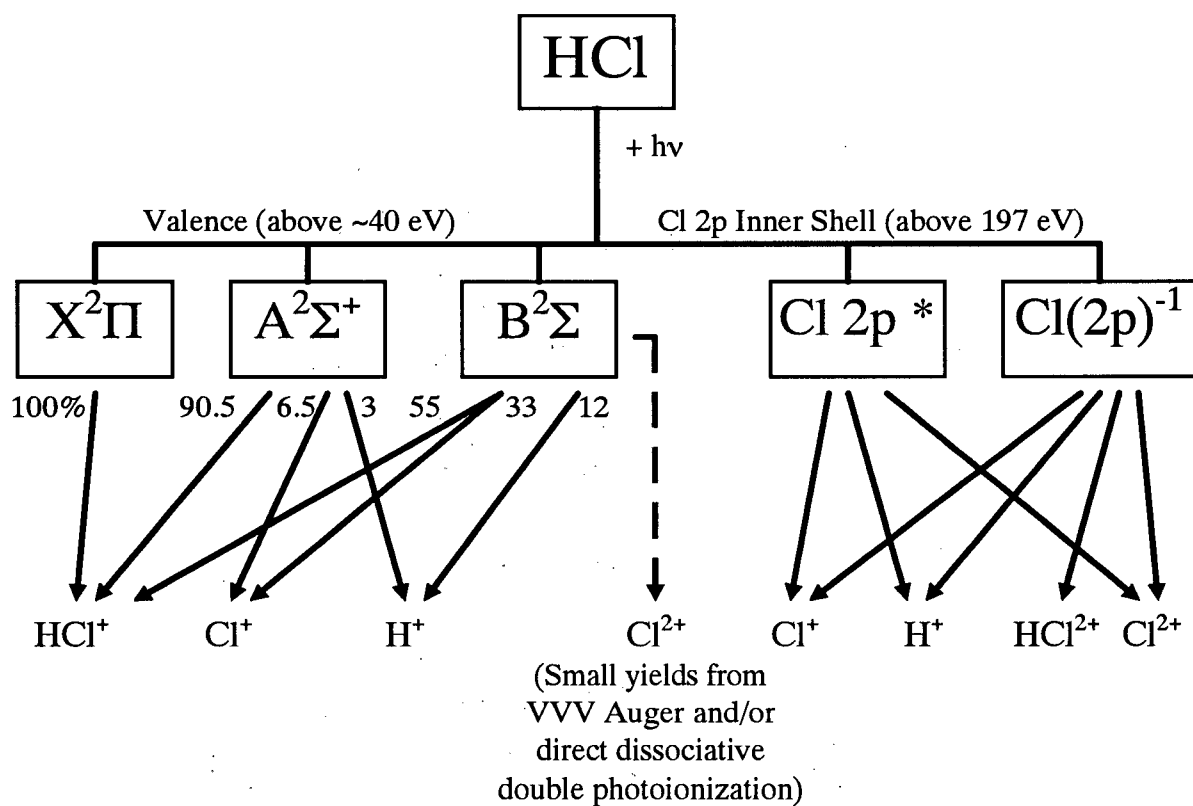
Figure 4.14. Dipole ionic photofragmentation breakdown pathways of HCl in the VUV and soft

X-ray regions.

photoionization data were obtained, and thus slightly different fits of electronic ion state contributions to molecular and dissociative ion PPOS's were found. The differences between Cl^+ and H^+ oscillator strengths and the electronic ion state contributions (figures 4.13(b,c)) in the 25-30 eV range, which have been observed in the present work, were also seen in the earlier work by Daviel et al. [10].

4.2.5 Photoionization Studies of HCl in the Cl 2p Region

Time-of-flight (TOF) mass spectra at selected energies in the Cl 2p inner shell region, and in the valence shell at 197 eV just below the onset of Cl 2p excitation, are shown in figure 4.15. In this region (see figure 4.1) the total photoabsorption, and thus the photoionization, is dominated by Cl 2p processes, with only ~10% being due to valence shell photoionization. The intensity scale for each panel of figure 4.15 is relative to the tallest (i.e. the height of the most intense) peak in each spectrum. As can be seen in the top panel, at 197.0 eV, below the first 2p excitation edge, the most intense peak is the $H^{35}Cl^+$, consistent with this being due only to the valence shell. As the equivalent photon energy increases, i.e. as the Cl 2p σ^* excitation threshold is reached (201.5 eV), the relative intensity of the HCl^+ peaks (two isotopes) decreases with respect to the Cl^+ peaks, indicating an increasing role for dissociative ionization. At 197 eV, in the valence continuum, the doubly charged ion Cl^{2+} is formed, but there are still no discernible HCl^{2+} ions. As the energy increases further into the Cl 2p inner shell Rydberg excitation region (206 eV), the intensity of the Cl^{2+} peaks increases, and HCl^+ decreases markedly. In the 2p ionization continuum (220 and 260 eV), HCl^{2+} appears while HCl^+ is dramatically reduced. The H^+ peak increases in relation to the other ion peaks as the energy increases.
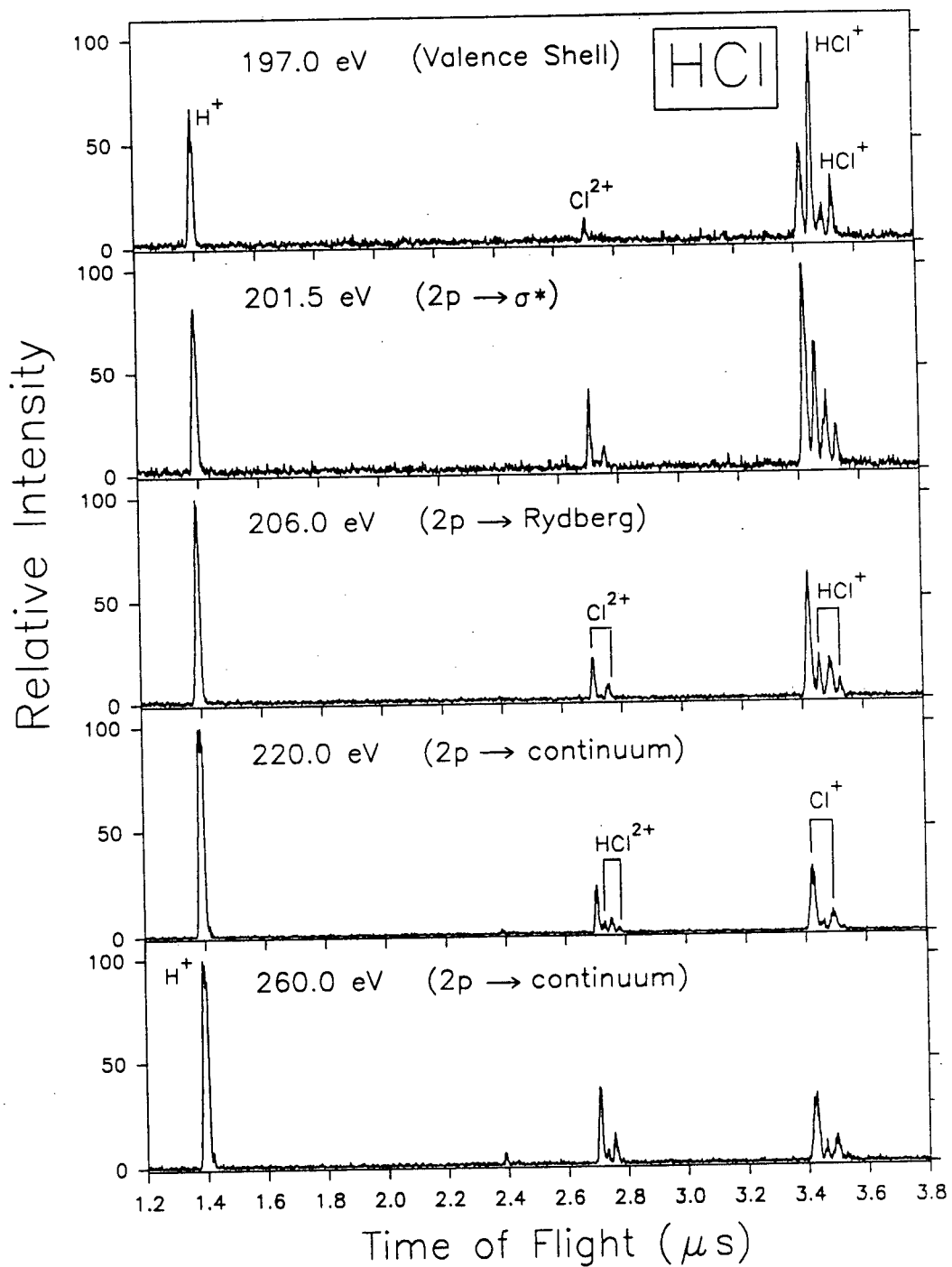
Figure 4.15. Time-of-flight (TOF) mass spectra at selected energy losses in the valence shell and Cl 2p inner shell regions for the photoionization of HCl.

The trends outlined above are consistent with what is observed in the photoabsorption studies. As can be seen in figure 4.1(b), above the Cl 2p ionization edge, the valence shell cross section represents only a small fraction of the total cross section. Thus the molecular ion, HCl^+, is formed mostly from valence shell processes and drops off significantly above the Cl 2p edge with respect to the other ion peaks. The formation of Cl^{2+} in the valence shell could result from dissociative Auger decay of inner valence ion states ($B^2\Sigma$), i.e. VVV Auger processes, or by dissociative double photoionization. Clearly the relative yield of Cl^{2+} increases significantly in the Cl 2p excitation and ionization regions. In the Cl 2p σ^* and Rydberg excitation regions this could be due to dissociative autoionization (i.e. Resonance Auger [56]) of neutral, Cl 2p, excited states of HCl down to H + Cl^{2+} with ejection of two electrons. In the Cl 2p continuum, Cl^{2+} can be formed by dissociative (LVV) Auger processes. Furthermore, the increase of H^+ as well as Cl^+ with respect to HCl^+ is likely due to Coulomb explosion of doubly charged (HCl^{2+}) ions to give H^+ + Cl^+. The increased width of the H^+ peaks (see figure 4.15) at 220 and 260 eV is consistent with the high kinetic energy of H^+ ions expected from Coulomb explosions. The doubly charged HCl^{2+}, which appears in the Cl 2p continuum, could be the result of a competing Auger process in which ionization of HCl results in a 2p hole state, which then decays, without dissociation, to form HCl^{2+}.

Photoion branching ratios for the Cl 2p inner shell region are shown in the higher energy portions of figure 4.8 and given numerically in table 4.4. It should be noted that the branching ratios, obtained from TOF mass spectra, are relative to the peak with the greatest integrated *area*, as opposed to the *height* of the most intense peak in the case of the TOF spectra presented in figure 4.7. As discussed in section 4.2.3 above, the branching ratios of all ions present in the

valence shell level off above 50 eV and up to 197 eV, as expected by the ionic photofragmentation model [8]. However, not surprisingly some changes occur above 197 eV in the Cl 2p inner shell region. Most noticeably, the amount of HCl^+ decreases sharply with respect to the other ions, then levels off above 210 eV. This is expected, since as discussed above HCl^+ is formed mostly from valence shell processes. The very small yield of HCl^+ in the Cl 2p region indicates that when a 2p hole occurs in the molecule due to excitation or ionization, then the molecular ion has a very high probability of break-up (i.e. dissociation) by non-radiative processes such as autoionization (resonance Auger) and Auger decay. The relative yield of the Cl^+ ion increases sharply (figure 4.8) near 200 eV, just below the Cl 2p ionization edge, then drops and levels off above 210 eV. The resulting spike is apparently due to dissociative autoionization of Cl 2p neutral (valence and/or Rydberg) excited states down to $H + Cl^+$, which would account for both the sharp drop in HCl^+ as well as the spike in Cl^+. The photoion branching ratio for Cl^{2+} rises sharply at the Cl 2p excitation edge. Similarly the relative yields of HCl^{2+} and H^+ increase dramatically at the Cl 2p ionization edge. HCl^{2+} is formed only from Cl 2p ionization with no detectable contribution from valence shell or Cl 2p excitation processes.

Partial oscillator strengths for photoionization of HCl in the Cl 2p inner shell region (derived from the product of the branching ratios, the photoionization efficiency and the total photoabsorption) are shown in figure 4.10 and given numerically in table 4.5. The photoionization efficiency has been assumed to be unity in the Cl 2p inner shell region. The trends observed in the PPOS's in the Cl 2p inner shell correspond to those already observed in the TOF mass spectra and in the photoion branching ratios, but in this case (figure 4.10) absolute, rather than relative, yields are shown. The PPOS for HCl^+ drops dramatically in the Cl 2p region, corresponding with increases in the yields of the other four (dissociative) ionic species. The

PPOS's conclusively show that in the soft X-ray region above ~198 eV, Cl 2p excited HCl molecules or singly charged cations (HCl^+) with a Cl 2p hole are extremely unstable and very rapidly decay to give a range of singly or doubly charged fragment ions as well as neutral fragments. The overall breakdown pathways of HCl in the VUV and soft X-ray regions above ~40 eV (i.e. above the Franck-Condon limits of all valence shell ionization processes) resulting from the present measurements and analysis are summarized in figure 4.14 above. Further information and confirmation of the dipole breakdown pathways described above could be obtained from photoelectron-photoion coincidence experiments as a function of energy.

Table 4.3: Absolute differential photoabsorption oscillator strengths of HCl for the valence shell and Cl 2p inner shell regions (1 eV fwhm).

Total Photoabsorption Oscillator Strength (df/dE)							
eV	$10^{-2}eV^{-1}$	eV	$10^{-2}eV^{-1}$	eV	$10^{-2}eV^{-1}$	eV	$10^{-2}eV^{-1}$
6.0	0.10	18.5	39.66	31.0	8.29	47.0	1.11
6.5	0.33	19.0	38.94	31.5	7.48	48.0	1.13
7.0	1.04	19.5	37.79	32.0	6.90	49.0	1.12
7.5	2.12	20.0	36.73	32.5	5.89	50.0	1.14
8.0	2.87	20.5	35.25	33.0	5.46	51.0	1.13
8.5	2.75	21.0	33.60	33.5	4.85	52.0	1.11
9.0	6.43	21.5	32.24	34.0	4.37	53.0	1.12
9.5	18.76	22.0	31.16	34.5	3.94	54.0	1.15
10.0	12.37	22.5	29.51	35.0	3.36	55.0	1.12
10.5	7.48	23.0	28.04	35.5	3.00	56.0	1.17
11.0	24.16	23.5	26.15	36.0	2.86	57.0	1.13
11.5	33.21	24.0	25.29	36.5	2.63	58.0	1.14
12.0	40.29	24.5	24.02	37.0	2.34	59.0	1.17
12.5	41.50	25.0	22.58	37.5	2.08	60.0	1.13
13.0	33.05	25.5	21.30	38.0	2.02	61.0	1.13
13.5	27.26	26.0	19.50	38.5	1.81	62.0	1.15
14.0	31.36	26.5	18.42	39.0	1.76	63.0	1.15
14.5	39.69	27.0	17.16	39.5	1.66	64.0	1.11
15.0	42.57	27.5	16.30	40.0	1.47	65.0	1.14
15.5	41.77	28.0	14.78	41.0	1.35	66.0	1.10
16.0	41.92	28.5	13.55	42.0	1.27	67.0	1.12
16.5	41.68	29.0	12.37	43.0	1.19	68.0	1.13
17.0	41.39	29.5	11.23	44.0	1.16	69.0	1.12
17.5	41.06	30.0	10.22	45.0	1.12	70.0	1.10
18.0	40.57	30.5	9.35	46.0	1.12	71.0	1.09

Table 4.3 (continued): Absolute differential photoabsorption oscillator strengths of HCl for the valence shell and Cl 2p inner shell regions (1 eV fwhm).

Total Photoabsorption Oscillator Strength (df/dE)							
eV	$10^{-2}eV^{-1}$	eV	$10^{-2}eV^{-1}$	eV	$10^{-2}eV^{-1}$	eV	$10^{-2}eV^{-1}$
72.0	1.06	114.0	0.70	164.0	0.41	203.5	0.55
73.0	1.08	116.0	0.69	166.0	0.40	204.0	0.59
74.0	1.08	118.0	0.66	168.0	0.39	204.5	0.68
75.0	1.08	120.0	0.65	170.0	0.40	205.0	0.66
76.0	1.07	122.0	0.64	172.0	0.38	205.5	0.77
77.0	1.03	124.0	0.64	174.0	0.37	206.0	0.98
78.0	1.00	126.0	0.61	176.0	0.37	206.5	1.05
79.0	1.02	128.0	0.59	178.0	0.35	207.0	1.18
80.0	1.01	130.0	0.59	180.0	0.36	207.5	1.35
82.0	0.99	132.0	0.57	182.0	0.36	208.0	1.46
84.0	0.97	134.0	0.55	184.0	0.35	208.5	1.56
86.0	0.94	136.0	0.55	186.0	0.35	209.0	1.70
88.0	0.92	138.0	0.54	188.0	0.34	209.5	1.78
90.0	0.91	140.0	0.52	190.0	0.35	210.0	1.83
92.0	0.89	142.0	0.50	192.0	0.31	210.5	1.96
94.0	0.87	144.0	0.51	194.0	0.31	211.0	2.00
96.0	0.85	146.0	0.50	196.0	0.33	211.5	2.08
98.0	0.83	148.0	0.48	198.0	0.30	212.0	2.17
100.0	0.82	150.0	0.48	200.0	0.33	212.5	2.20
102.0	0.79	152.0	0.46	200.5	0.39	213.0	2.24
104.0	0.76	154.0	0.47	201.0	0.47	213.5	2.27
106.0	0.76	156.0	0.43	201.5	0.54	214.0	2.29
108.0	0.74	158.0	0.43	202.0	0.56	214.5	2.38
110.0	0.72	160.0	0.43	202.5	0.57	215.0	2.38
112.0	0.71	162.0	0.41	203.0	0.56	215.5	2.41

Table 4.3 (continued): Absolute total photoabsorption oscillator strengths of HCl for the valence and Cl 2p inner shell regions.

Total Photoabsorption Oscillator Strength (df/dE)					
eV	$10^{-2}eV^{-1}$	eV	$10^{-2}eV^{-1}$	eV	$10^{-2}eV^{-1}$
216.0	2.48	232.0	2.35	257.0	2.20
216.5	2.46	233.0	2.36	258.0	2.15
217.0	2.48	234.0	2.35	259.0	2.18
217.5	2.47	235.0	2.35	260.0	2.09
218.0	2.50	236.0	2.39	261.0	2.08
218.5	2.53	237.0	2.35	262.0	2.16
219.0	2.53	238.0	2.37	263.0	2.08
219.5	2.50	239.0	2.30	264.0	2.04
220.0	2.47	240.0	2.27	265.0	2.13
220.5	2.56	241.0	2.32	266.0	2.05
221.0	2.51	242.0	2.27	267.0	2.02
221.5	2.52	243.0	2.28	268.0	2.05
222.0	2.56	244.0	2.24	269.0	2.06
222.5	2.52	245.0	2.30	270.0	2.13
223.0	2.55	246.0	2.22	271.0	2.10
223.5	2.56	247.0	2.25	272.0	2.13
224.0	2.54	248.0	2.22	273.0	2.09
224.5	2.46	249.0	2.25	274.0	2.10
225.0	2.55	250.0	2.29	275.0	2.13
226.0	2.49	251.0	2.16	276.0	2.13
227.0	2.42	252.0	2.23	277.0	2.08
228.0	2.45	253.0	2.21	278.0	2.04
229.0	2.42	254.0	2.08	279.0	2.17
230.0	2.34	255.0	2.11	280.0	2.10
231.0	2.44	256.0	2.15		

Table 4.4: Photoion branching ratios for the molecular and dissociative photoionization of HCl, as a percentage of total photoionization.

Photon Energy (eV)	Photoion Branching Ratio (%)				
	HCl^+	Cl^+	HCl^{2+}	Cl^{2+}	H^+
12.5	100.00				
13.0	100.00				
13.5	100.00				
14.0	100.00				
14.5	100.00				
15.0	100.00				
15.5	100.00				
16.0	100.00				
16.5	100.00				
17.0	100.00				
17.5	98.80	1.20			
18.0	98.26	1.74			
18.5	97.99	2.01			
19.0	97.50	2.33			0.18
19.5	96.74	2.66			0.61
20.0	96.54	2.79			0.67
20.5	96.24	2.66			1.11
21.0	95.59	3.19			1.21
21.5	95.32	3.25			1.43
22.0	94.63	3.90			1.47
22.5	93.94	4.35			1.72
23.0	92.28	5.20			2.51
23.5	90.75	6.41			2.84
24.0	89.73	7.38			2.89
24.5	89.24	7.90			2.87
25.0	89.20	8.66			2.15
25.5	88.59	9.39			2.03
26.0	86.99	10.78			2.23
26.5	86.94	11.30			1.76
27.0	86.79	11.26			1.96
27.5	85.88	12.11			2.02

Table 4.4 (continued): Photoion branching ratios for the photoionization of HCl, as a percentage of total photoionization.

Photon Energy (eV)	Photoion Branching Ratio (%)				
	HCl^+	Cl^+	HCl^{2+}	Cl^{2+}	H^+
28.0	85.51	12.37			2.12
28.5	84.98	12.52			2.51
29.0	84.39	12.66			2.95
29.5	83.43	12.88			3.69
30.0	82.15	13.40			4.45
30.0	80.92	14.45			4.62
32.0	77.04	16.11			6.85
34.0	71.92	17.57			10.51
36.0	68.39	19.06			12.55
38.0	61.37	22.78			15.85
40.0	57.30	25.13			17.57
42.0	50.88	27.19			21.94
44.0	48.58	28.29			23.13
46.0	46.24	29.89			23.87
48.0	45.80	29.10			25.10
50.0	46.00	28.91			25.09
50.0	45.36	29.16			25.49
55.0	44.75	28.11			27.15
60.0	44.49	28.15			27.37
65.0	45.96	26.31			27.73
70.0	46.11	25.94			27.94
75.0	46.03	26.33			27.64
80.0	45.95	26.17			27.88
197.0	40.05	27.23		3.88	28.84
201.5	19.82	41.43		9.33	29.43
206.0	8.59	35.78		9.29	46.35
211.0	3.37	21.35	1.86	9.74	63.68
220.0	2.53	20.23	2.41	10.22	64.62
240.0	3.18	22.95	1.76	14.54	57.57
260.0	3.03	21.54	1.71	15.66	58.07

Table 4.5: Absolute partial differential oscillator strengths for the molecular and dissociative photoionization of HCl.

Photon Energy (eV)	Partial Differential Oscillator Strength ($10^{-2}eV^{-1}$)				
	HCl^+	Cl^+	HCl^{2+}	Cl^{2+}	H^+
12.5	4.63				
13.0	12.06				
13.5	16.20				
14.0	21.13				
14.5	28.27				
15.0	32.90				
15.5	34.20				
16.0	35.28				
16.5	36.06				
17.0	36.86				
17.5	36.87	0.45			
18.0	36.69	0.65			
18.5	35.81	0.74			
19.0	35.68	0.85			0.07
19.5	34.24	0.94			0.22
20.0	33.45	0.97			0.23
20.5	32.28	0.89			0.37
21.0	30.27	1.01			0.38
21.5	29.44	1.00			0.44
22.0	28.40	1.17			0.44
22.5	27.28	1.26			0.50
23.0	25.40	1.43			0.69
23.5	23.44	1.66			0.73
24.0	22.25	1.83			0.72
24.5	21.20	1.88			0.68
25.0	20.14	1.96			0.49
25.5	18.87	2.00			0.43
26.0	16.96	2.10			0.44
26.5	16.02	2.08			0.33
27.0	14.89	1.93			0.34

Table 4.5 (continued): Absolute partial differential oscillator strengths for molecular and dissociative photoionization of HCl.

Photon Energy (eV)	Partial Differential Oscillator Strength ($10^{-2}\,eV^{-1}$)				
	HCl^+	Cl^+	HCl^{2+}	Cl^{2+}	H^+
27.5	14.00	1.97			0.33
28.0	12.64	1.83			0.31
28.5	11.52	1.70			0.34
29.0	10.44	1.57			0.36
29.5	9.37	1.45			0.42
30.0	8.27	1.48			0.47
32.0	5.32	1.11			0.47
34.0	3.14	0.77			0.46
36.0	1.96	0.55			0.36
38.0	1.24	0.46			0.32
40.0	0.84	0.37			0.26
42.0	0.65	0.35			0.28
44.0	0.57	0.33			0.27
46.0	0.52	0.34			0.27
48.0	0.52	0.33			0.28
50.0	0.52	0.33			0.29
55.0	0.50	0.31			0.30
60.0	0.50	0.32			0.31
65.0	0.52	0.30			0.32
70.0	0.51	0.28			0.31
75.0	0.50	0.28			0.30
80.0	0.46	0.26			0.28
197.0	0.13	0.09		0.01	0.09
201.5	0.11	0.22		0.05	0.16
206.0	0.08	0.35		0.09	0.45
211.0	0.07	0.43	0.04	0.20	1.28
220.0	0.06	0.50	0.06	0.25	1.60
240.0	0.07	0.52	0.04	0.33	1.31
260.0	0.06	0.45	0.04	0.33	1.21

Table 4.6: Partial photoionization differential oscillator strengths for production of the electronic ion states of HCl.

Photon Energy (eV)	Partial Oscillator Strength[a] $(10^{-2}eV^{-1})$		
	$X^2\Pi$	$A^2\Sigma^+$	$B^2\Sigma$
12.5	4.63		
13.0	12.06		
13.5	16.20		
14.0	21.13		
14.5	28.27		
15.0	32.90		
15.5	34.20		
16.0	34.93	0.35	
16.5	33.53	2.52	
17.0	30.22	6.63	
17.5	27.24	10.08	
18.0	25.39	11.95	
18.5	24.12	12.43	
19.0	23.42	13.18	
19.5	23.01	12.39	
20.0	21.48	13.17	
20.5	20.80	12.75	
21.0	20.26	11.40	
21.5	20.08	10.81	
22.0	19.51	10.21	0.30
22.5	18.01	9.58	1.45
23.0	17.07	8.26	2.20
23.5	15.75	6.71	3.36

a. These values have been obtained from photoelectron branching ratios [10] using the presently reported photoabsorption differential oscillator strengths and photoionization efficiencies.

Table 4.6 (continued): Partial photoionization differential oscillator strengths for production of

the electronic ion states of HCl.

Photon Energy (eV)	Partial Oscillator Strength $(10^{-2}eV^{-1})$		
	$X^2\Pi$	$A^2\Sigma^+$	$B^2\Sigma$
24.0	15.87	6.69	2.23
24.5	14.49	5.94	3.33
25.0	14.24	5.42	2.94
25.5	12.55	4.81	3.56
26.0	11.87	4.35	3.56
26.5	10.57	4.08	3.90
27.0	8.86	3.58	4.60
27.5	8.48	3.20	4.16
28.0	7.69	2.81	4.29
28.5	6.91	2.57	4.20
29.0	6.19	2.35	3.84
29.5	4.94	1.69	4.61
30.0	4.29	1.74	4.19
31.0	2.65	1.20	4.71
32.0	2.69	1.24	3.04
33.0	1.92	0.79	2.93
34.0	0.87	0.57	2.93
35.0	0.47	0.40	2.75
36.0	0.49	0.31	2.06
37.0	0.24	0.24	1.95
38.0	0.08	0.22	1.72
39.0	0.16	0.23	1.36
40.0	0.07	0.40	1.00

a. These values have been obtained from photoelectron branching ratios [10] using the presently
reported photoabsorption differential oscillator strengths and photoionization efficiencies.

Chapter 5

Photoabsorption and Photoionization Studies of Hydrogen Bromide

5.1 Introduction

Hydrogen bromide is of interest in molecular spectroscopy, as well as in other areas of scientific research. Hydrogen halides, including HBr, exist in the Earth's upper atmosphere, and thus quantitative spectroscopic data for HBr are needed for the understanding of atmospheric photochemistry [78]. Since HBr absorbs light at a longer wavelength than HCl or HF, it is more subject to solar photodissociation, which is believed to be an important chemical process in destroying HBr in the upper atmosphere [79]. HBr is also of interest in the chemical etching of semiconductor material, since photodissociation of HBr is an important process for the Br source [80]. In biochemistry, the photodissociation cross section of HBr is needed to determine the concentration of Br atoms produced by photolysis [78]. The present work is, to the best of our knowledge, the only study measuring absolute photoabsorption (5-300 eV) and photoionization (10-91 eV) oscillator strengths (cross sections) over a very wide range of the valence and Br 3d inner shell regions. A much earlier study of HBr [11] in this laboratory reported absolute photoabsorption (7-100 eV) and photoionization (11-40 eV) measurements using low resolution dipole (e,e) and (e,e+ion) spectroscopies at low resolution (1 eV fwhm). However, limitations in the earlier instrumentation and measurement procedures as well as in the calibration of the absolute scale, similar to the situation discussed in chapter 4 for HCl, place some doubt on the reliability of these results. This suggests that new absolute measurements should be performed for HBr.

There are few previously published *absolute* photoabsorption studies of HBr. Nee et al [78] reported the absolute photoabsorption and fluorescence cross sections of HBr in the 105-235

nm (5.3-11.8 eV) region, using synchrotron radiation. Earlier works by Roxlo and Mandl [35], by Huebert and Martin [81], by Roman [36], and by Goodeve and Taylor [82] reported absolute photoabsorption cross sections in the pre-edge region below 8 eV. Apart from the earlier low resolution dipole (e,e) study, no absolute photoabsorption studies have been reported for the valence shell in the VUV (11-80 eV) and beyond, nor are there any absolute results for the Br 3d inner shell spectrum of HBr.

Qualitative photoabsorption studies (i.e. limited range spectra without absolute intensity scales) of HBr have been reported in a number of papers. Photographic spectrophotometry was used by Ginter and Tilford [83, 84, 85], by Baig et al. [86] below 12 eV, and by Terwilliger and Smith [87] from 12.5 to 15.5 eV. Puttner et al. [88] used synchrotron radiation to investigate ligand-field splitting of the Br 3d inner shell levels in the region 69-79 eV at high resolution.

Photoelectron spectroscopy has also been used to study the photoionization of HBr. Carlson et al. [69] measured angular distribution parameters as a function of photon energy from the outer valence photoelectron spectrum of HBr. Morin and Nenner [89] used synchrotron radiation to study the HBr photoelectron spectrum at photon energies on and off the 3d→σ* resonance in HBr (see section 5.2.2.3). The high resolution valence shell photoelectron spectra of HBr and DBr have been measured by Adam et al [90] using an AlK$_\alpha$ X-ray source. Salzmann et al. [91] have obtained spin-resolved photoelectron spectra of HBr in the region 12-15 eV using circularly polarized synchrotron radiation. Liu et al. [92, 93] have investigated resonance Auger spectroscopy of HBr with the photon energy tuned to the HBr Br *3d* → *5p*π resonance.

Other studies of the electronic excitation spectra of HBr have been reported using electron impact techniques. England et al. [94] obtained energy-loss spectra of HBr and DBr between 8 and 16 eV with a resolution of 30 meV fwhm, using different combinations of scattered electron

energy and angle, from 0.5 eV and 90° to 35 eV and 2°. Electron energy loss spectroscopy has also been used by Shaw et al. [47] to measure the energy loss spectrum of HBr in the valence (7-15 eV) and Br 3d inner shell (69-79 eV) regions, using an electron impact energy of 1.5 keV and 0° scattering angle.

In the present work the photoabsorption and photoionization of HBr have been re-investigated using dipole (e,e) and dipole (e,e+ion) spectroscopies with the improved instrumentation [7, 27] and the refined data collection and analysis techniques [7,22]. The range of the low resolution photoabsorption data has also been considerably extended to 300 eV, and photoionization data have been extended to 91 eV on the low resolution dipole (e,e), dipole (e,e+ion) spectrometer. In addition, high resolution (0.05-0.1 eV fwhm) absolute photoabsorption spectra have been obtained from 5 to 100 eV on the high resolution dipole (e,e) spectrometer (see references [3, 19, 29] and section 3.3) developed after the original low resolution [11] studies of HBr were reported.

5.2 Results and Discussion

5.2.1 Electron Structure

The ground state electron configuration of HBr in the independent particle model can be expressed as:

$$\text{core} \quad (3d)^{10} \quad (7\sigma)^2(8\sigma)^2(4\pi)^4 \quad (9\sigma)^0$$

$$\text{Br 3d} \qquad \text{Valence} \qquad \text{Virtual Valence}$$
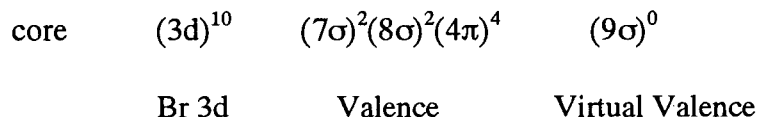
The electronic states of HBr$^+$ produced by removal of an electron from each of the valence orbitals are $X^2\Pi_{3/2,1/2}$, $(4\pi)^{-1}$; $A^2\Sigma^+$, $(8\sigma)^{-1}$; and $B^2\Sigma$, $(7\sigma)^{-1}$ [11, 49]. Ionization potentials for these states have been found by PES and the analogous method of electron momentum spectroscopy. Lempka et al [49] have reported values of 11.67 and 12.00 eV for the spin-orbit

split doublet $X^2\Pi_{3/2,1/2}$, and a value of 15.27 eV for the $A^2\Sigma^+$ state using HeI high resolution PES. These values are in good agreement with other PES studies [95, 96]. Electron momentum spectroscopy has been used at low resolution by Brion et al. [74], who reported values of 11.9 eV $(X^2\Pi_{3/2,1/2})$, 15.6 eV $(A^2\Sigma^+)$, and 24.3, 30.3 eV $(B^2\Sigma$ manifold). The valence shell photoelectron spectrum, including the HBr^+ $B^2\Sigma$ inner valence region has been studied in detail by Adam et al. [90] using AlK_α radiation. The Br 3d inner shell ionization potentials have been found by Shaw et al. [47] to be 77.12 eV and 78.23 eV for the $3d_{5/2}$ and $3d_{3/2}$ states respectively.

5.2.2 Photoabsorption Oscillator Strengths

5.2.2.1 Low-Resolution Photoabsorption Measurements

Figures 5.1(a,b) show the low resolution (1 eV fwhm) absolute differential photoabsorption oscillator strength spectrum (5-50 eV and 5-300 eV) obtained in the present work by S(-2) sum-rule normalization of the relative oscillator strength spectrum, as described in section 2.4. The relative spectrum was obtained from the Bethe-Born converted EELS spectrum (see section 2.1) measured on the low resolution dipole (e,e) spectrometer. The absolute total photoabsorption oscillator strengths are given numerically in table 5.4. The ionization potentials shown on figure 5.1 are taken from experimental measurements [49, 74, 90]. The low energy onset (~70 eV) of the Br 3d inner shell spectrum causes the VTRK sum rule normalization procedures to be extremely unreliable. In particular, curve fitting and extrapolation of the higher energy region is not possible. Therefore, the S(-2) sum rule was used to place the spectrum on an
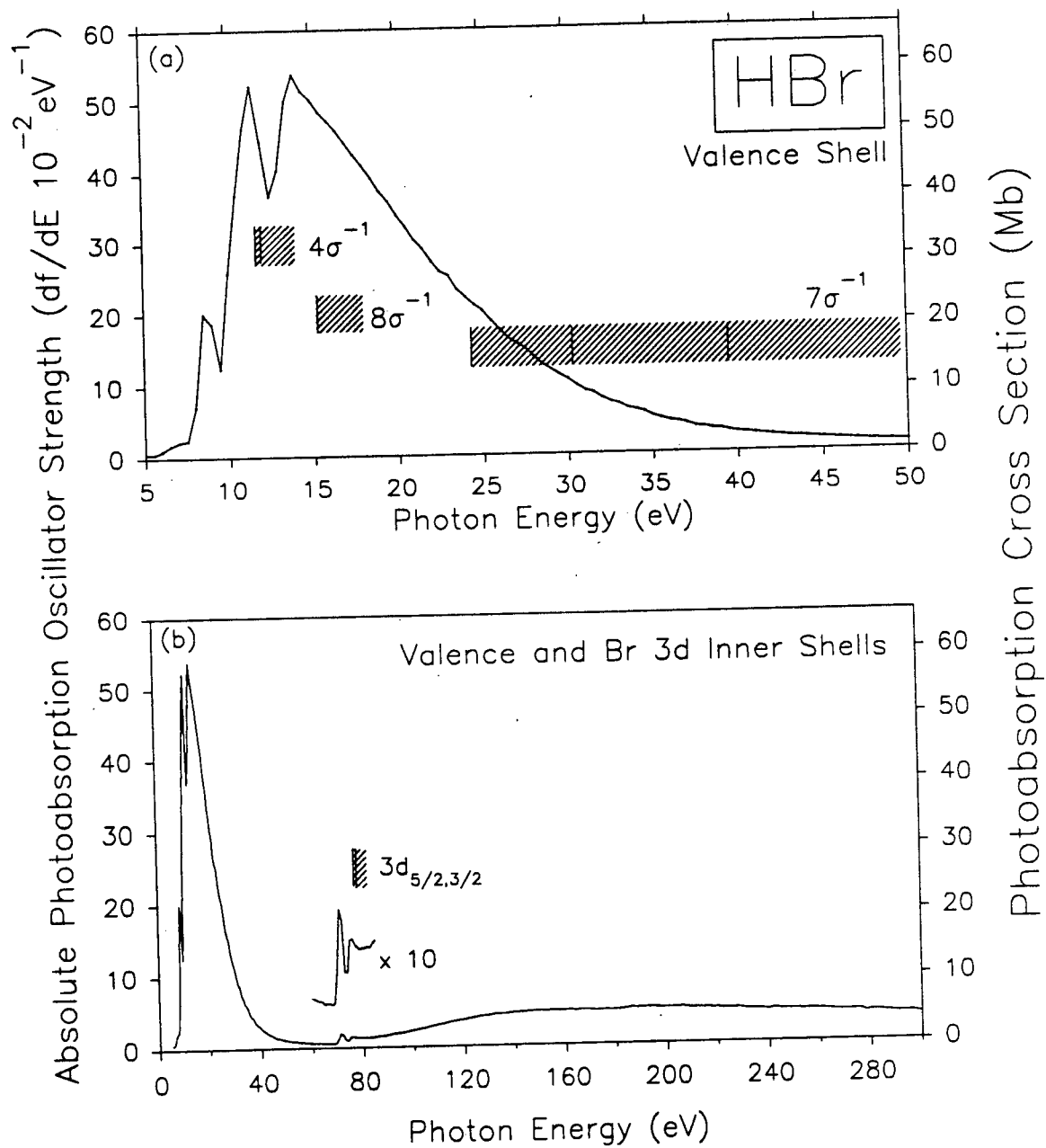
Figure 5.1: Absolute low resolution photoabsorption oscillator strengths (cross sections) for the valence and Br 3d inner shell regions of HBr.

absolute scale by using an experimental dipole polarizability (α_N) value of 23.7 a.u. [65]. The energy scale of the low resolution spectrum, as in the case of HCl (see section 4.2.2.1), was set by comparison with the high resolution spectrum convoluted with 1 eV fwhm (see section 3.3 and 5.2.2.2). As a consistency check, a comparison was made between the low resolution spectrum and the high resolution data convoluted with 1 eV fwhm and excellent agreement is obtained, as can be seen in figure 5.2(a).

In the earlier dipole (e,e) work on HBr [11], the absolute oscillator strength scale was obtained using the VTRK sum rule, without however taking into account the small correction factor due to Pauli-excluded transitions (see sections 2.4 and 4.1). Furthermore, the normalization took into account only the spectrum below 100 eV (i.e. the upper limit of the experimental measurements), with no attempt to fit and extrapolate the spectrum to infinite energy. It should be noted (see also the discussion on HCl in section 4.2.2.1) that these two considerations, i.e. the Pauli-excluded correction and the extrapolation to infinite energy, have opposing (and thus offsetting) effects on the magnitude of the resulting oscillator strength scale. However, as was found for HCl (section 4.1), neglect of the extrapolation to infinite energy is expected to have the major effect (see section 4.1 for the situation in HCl). However, in the case of HBr, the higher energy valence shell portion cannot be estimated due to the presence of the Br 3d continuum region (see figure 5.1(b)). The contribution of Pauli excluded transitions is expected to constitute less than 4% of the total valence shell oscillator strength [22]. It is therefore to be expected that the magnitudes of the previously determined oscillator strengths will differ from that obtained in the present work and this can be seen in figure 5.2(b). The differences in shape can be attributed to the improved background subtraction procedures in the present work
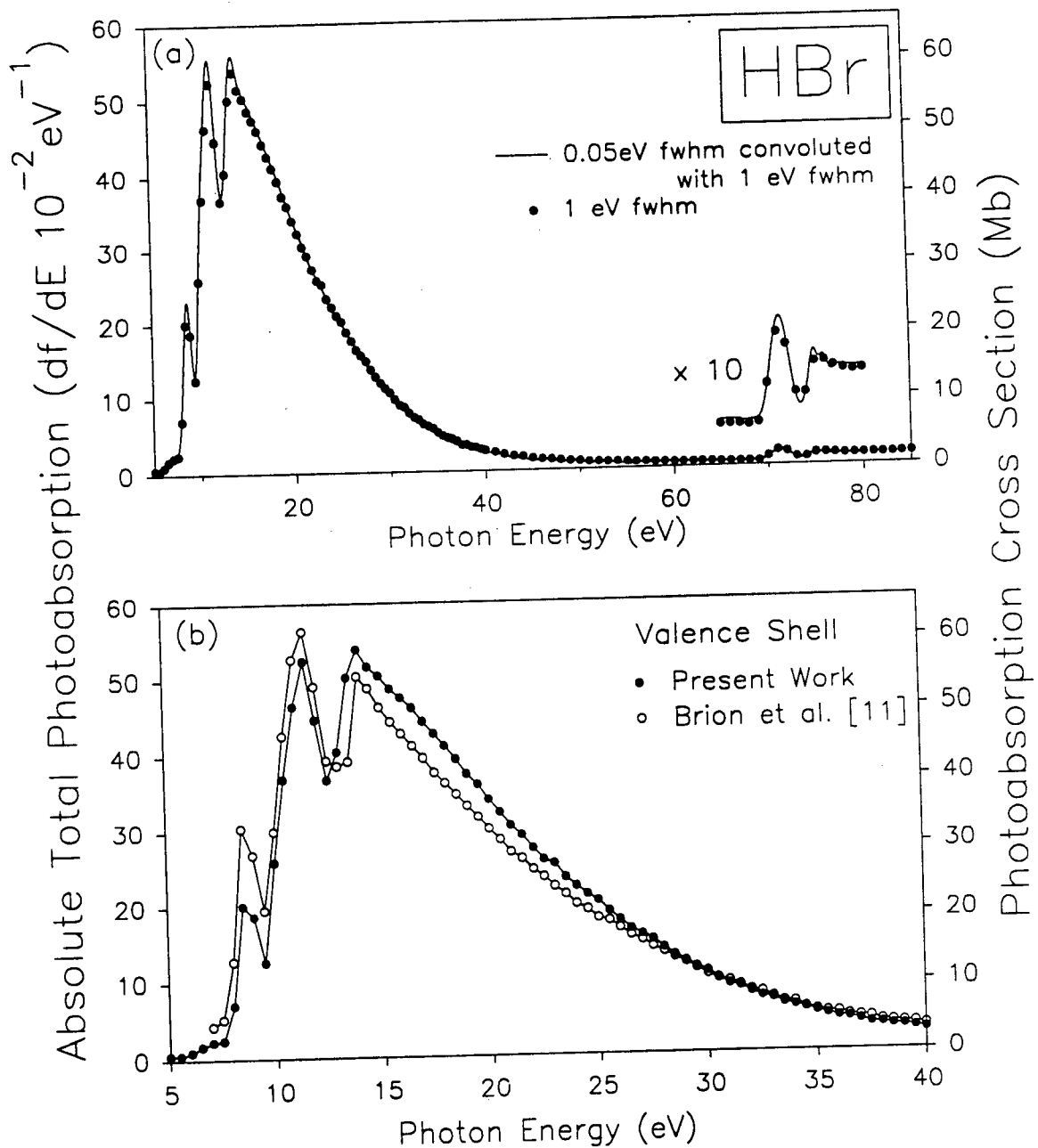
Figure 5.2: Comparisons of the low resolution (1.eV fwhm) absolute oscillator strength spectrum obtained in the present work with: (a) the high resolution (0.05 eV fwhm) spectrum obtained in the present work, convoluted with 1 eV fwhm; and (b) the absolute photoabsorption spectrum reported by Brion et al. [11].

(see discussion in section 4.2.2.1 for HCl).

At the low resolution of the spectrum in figure 5.1(a), very little discrete structure is observable in the valence shell region. Three broad peaks with maxima at ~ 8.5, 11.5, and 14.5 eV are evident, with a slight shoulder below 8 eV. The Br 3d inner shell spectrum is also distinguished by a peak with maximum at ~ 71 eV, corresponding to the 3d→σ* transition. The high resolution (0.05-0.1 eV fwhm) spectra, presented in the following sections, show much more detailed structure in the valence and the inner shell photoabsorption spectra of HBr.

5.2.2.2 Valence Shell High Resolution Photoabsorption Measurements for HBr

The valence shell high resolution (0.05 eV fwhm) absolute photoabsorption oscillator strength spectrum, shown in figure 5.3(a) from 5 to 16 eV, and in figure 5.3(b) from 5 to 25 eV, was normalized by the S(-2) sum rule using an experimental value of 23.7 a.u. for the static dipole polarizability (α_N) [65]. The high resolution valence shell shows much discrete structure. Below 8 eV, a low broad peak has been assigned to the $a^3\Pi,A^1\Pi$ electronic state [78]. The higher energy structures present above 8 eV can be assigned to Rydberg series, as represented by the assignments given in figure 5.3(a), taken from references [87, 94]. Above the $A^2\Sigma^+$ ionization limit at 15.3 eV, no discrete structures are visible in the valence shell photoabsorption continuum (see figure 5.3(b)).

As summarized above, very few absolute photoabsorption spectra of HBr have been previously published. The most recent study is by Nee et al. [78], who measured the photoabsorption and fluorescence spectra of HBr in the 5.3-11.8 region using synchrotron radiation. The absorption cross sections in the region between 5 and 8 eV reported by Nee et al. are about 16% lower than those reported in the present work, as shown in figure 5.4 and table
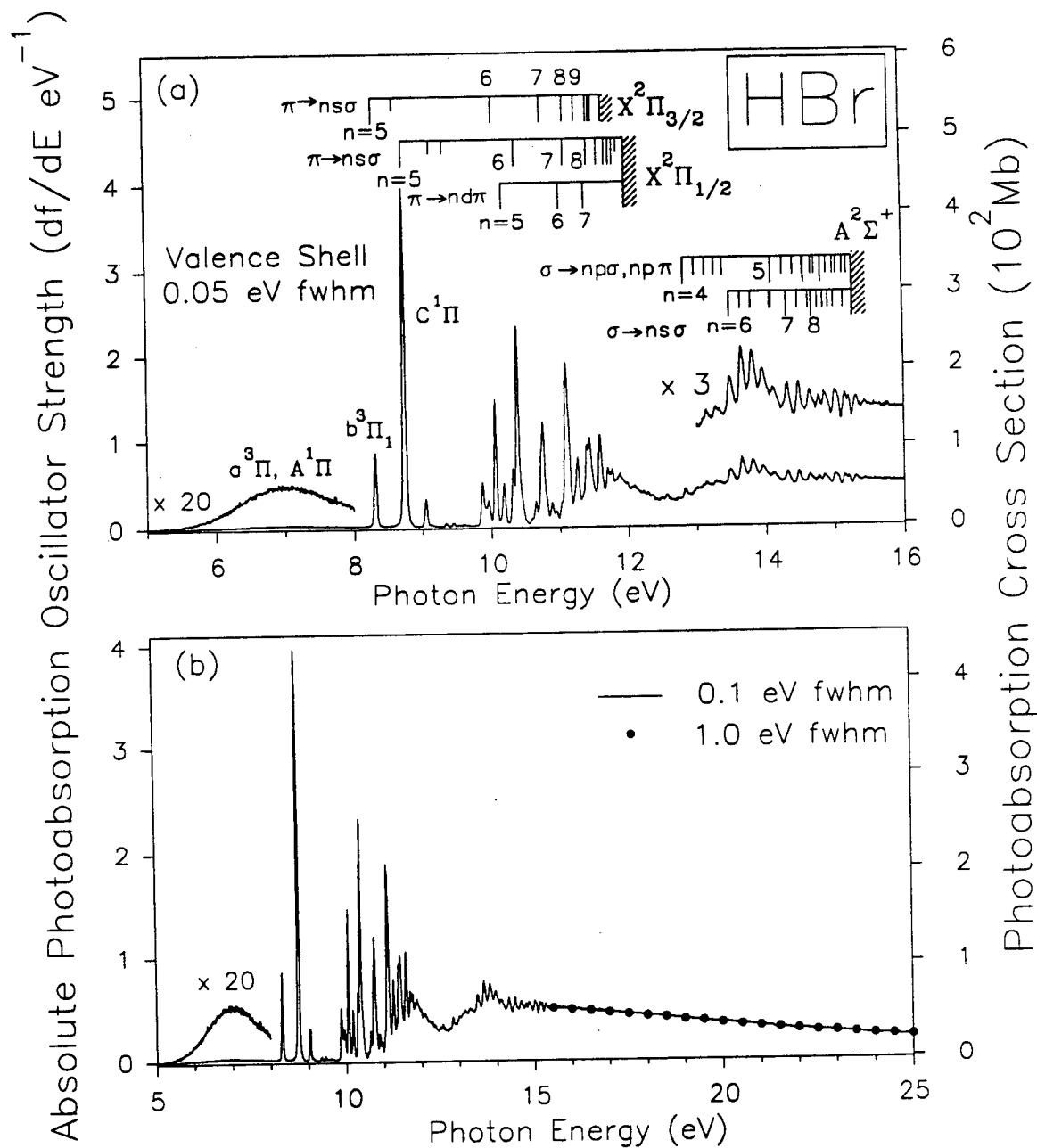
Figure 5.3: Absolute total photoabsorption oscillator strengths for the valence shell of HBr with

high resolution (0.05eV fwhm): (a) 5-16 eV with peak assignments from references [87, 94]; (b)

5-25 eV showing agreement with low resolution (1eV fwhm) measurements.

5.1. Part of the discrepancy can be accounted for by the ±20% uncertainty in the absorption cross section reported by Nee et al. [78]. In the energy range from 8 to 12 eV (the limit of their data [78]), the spectrum reported by Nee et al. [78] appears to be quite different from the spectrum obtained in the present work. As can be seen in table 5.1, integrated oscillator strengths reported by Nee et al. [78] are significantly (~ 2 orders of magnitude) lower than those obtained in the present work. This large difference is evidence of line-saturation (i.e. bandwidth-linewidth) effects that result from use of the Beer-Lambert law, as discussed in section 1.3. An attempt was made by Nee et al. to minimize this effect by taking measurements at very low sample pressures (below 2 mTorr) [78], but errors still occurred in this discrete region (8-12 eV) of the spectrum. A comparison was also reported [78] with earlier work by Huebert and Martin [81], who measured extinction coefficients for HBr in the region below 7.1 eV. The latter data [81] are ~3% higher [78] than the oscillator strengths obtained in the present work.

Roxlo and Mandl [35] have reported absolute photoabsorption cross sections in the energy region 5.4 to 7.3 eV. There is a large difference in their data when compared to the present work, as shown in figure 5.4 and table 5.1. The reported cross sections by Roxlo and Mandl are much lower than those reported in the present work. In earlier studies, Roman [36] and Goodeve and Taylor [82] also measured the absorption spectrum of HBr below 8 eV using photographic spectrophotometry. Both of these studies [36, 82] reported cross section which are considerably lower than those obtained in the present work, as can be seen in figure 5.4 and table 5.1. Agreement in this lower energy range below 7.9 eV is somewhat better in the case of the absolute spectra reported by Nee et al. [78].
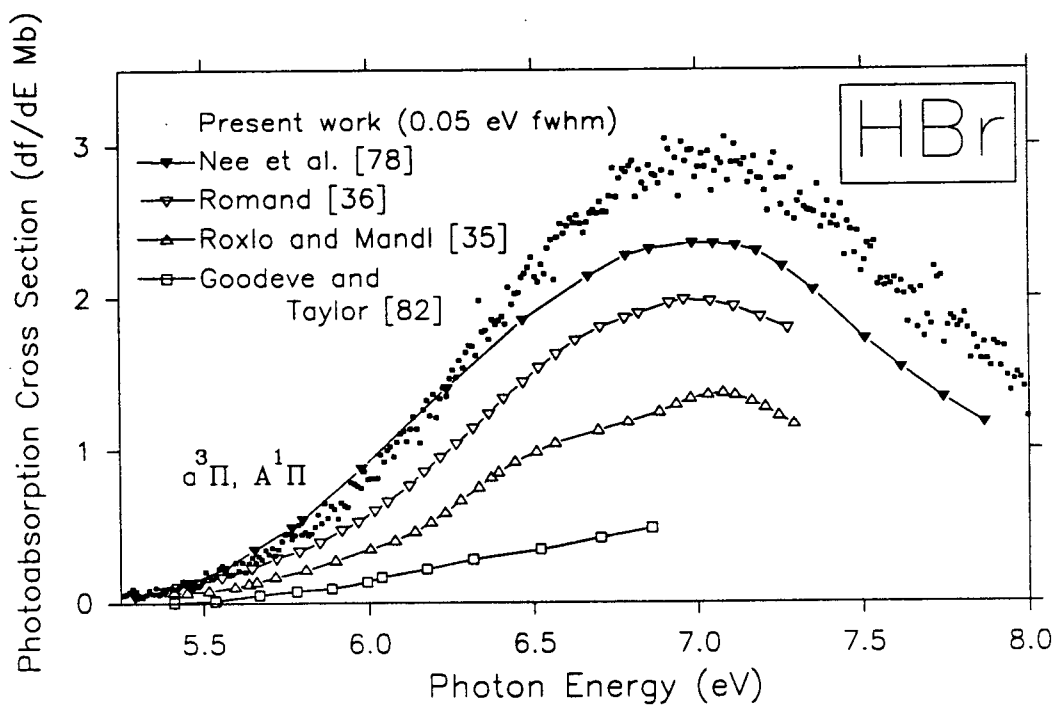
Figure 5.4: Comparison of absolute photoabsorption spectra obtained in the present work with reported spectra from the literature.

Table 5.1: Comparison of integrated oscillator strengths (cross sections) for HBr reported in the literature with selected energy ranges from the present work measurements.

Energy Range	Present Work (Mb)	Previous Work	
		(Mb)	Ref.
5.40-6.9	2.00	0.305	[82]
5.40-7.3	3.13	1.383	[35]
		2.11	[36]
5.30- 7.9	4.41	3.69	[78]
8.25- 8.35	4.31	0.0323	[78]
8.69- 8.79	20.08	0.172	[78]
8.99- 9.08	1.60	0.013	[78]
9.80-10.00	4.94		
10.00-10.11	6.91	0.0124	[78]
10.11-10.25	3.06	0.018	[78]
10.25-10.34	3.47		
10.34-10.50	13.94	0.010	[78]
10.55-10.98	14.71	0.0335	[78]
10.98-11.19	17.45	0.0512	[78]
11.19-11.31	6.38		
11.31-11.52	14.49		
11.52-11.65	9.61		
11.65-11.79	8.43		

5.2.2.3 Br 3d Inner Shell High Resolution Photoabsorption Measurements for HBr

The absolute photoabsorption oscillator strength spectrum for the Br 3d inner shell from 68 to 80 eV, obtained on the high resolution dipole (e,e) spectrometer at 0.1 eV fwhm, is shown in figure 5.5. The Br 3d relative oscillator strength spectrum was normalized to the S(-2) sum rule normalized valence shell spectrum (see previous section). The good agreement with the low resolution measurements below the Br 3d excitation region (figure 5.5) provides a consistency check on the accuracy of the absolute scale of the spectrum. A significant portion of the oscillator strength in the inner shell is contained in the broad peak with a maximum at ~71.5 eV, which corresponds to the strong $3d \rightarrow \sigma^*$ transition. The peaks at higher energies have been assigned to Rydberg states converging on the $(3d_{5/2,3/2})^{-1}$ limits. The peak assignments and ionization potentials in figure 5.5 are taken from reference [47]. Integrated oscillator strengths for selected energy ranges are given in table 5.2.

The sharp structures in the 73.5-78 eV photon energy region, particularly the peak at ~76 eV, show slight separation, which is most likely due to spin-orbit and ligand-field splitting. Puttner et al. [88] have reported a high resolution (10 meV fwhm) relative photoionization spectrum in the Br 3d excitation and ionization region (69-79 eV), obtained using synchrotron radiation. Their much higher resolution spectrum shows clear evidence of ligand-field splitting of both the Br $3d_{5/2}$ and Br $3d_{3/2}$ levels.

5.2.3 Photoionization Studies of HBr in the Valence Shell Region

Time-of-flight (TOF) mass spectra were obtained using the low resolution dipole (e,e) spectrometer in the dipole (e,e+ion) mode (see section 3.2) from 10.5 to 66 eV in the valence shell. The positively charged ionic species resulting from photoionization of HBr are listed in
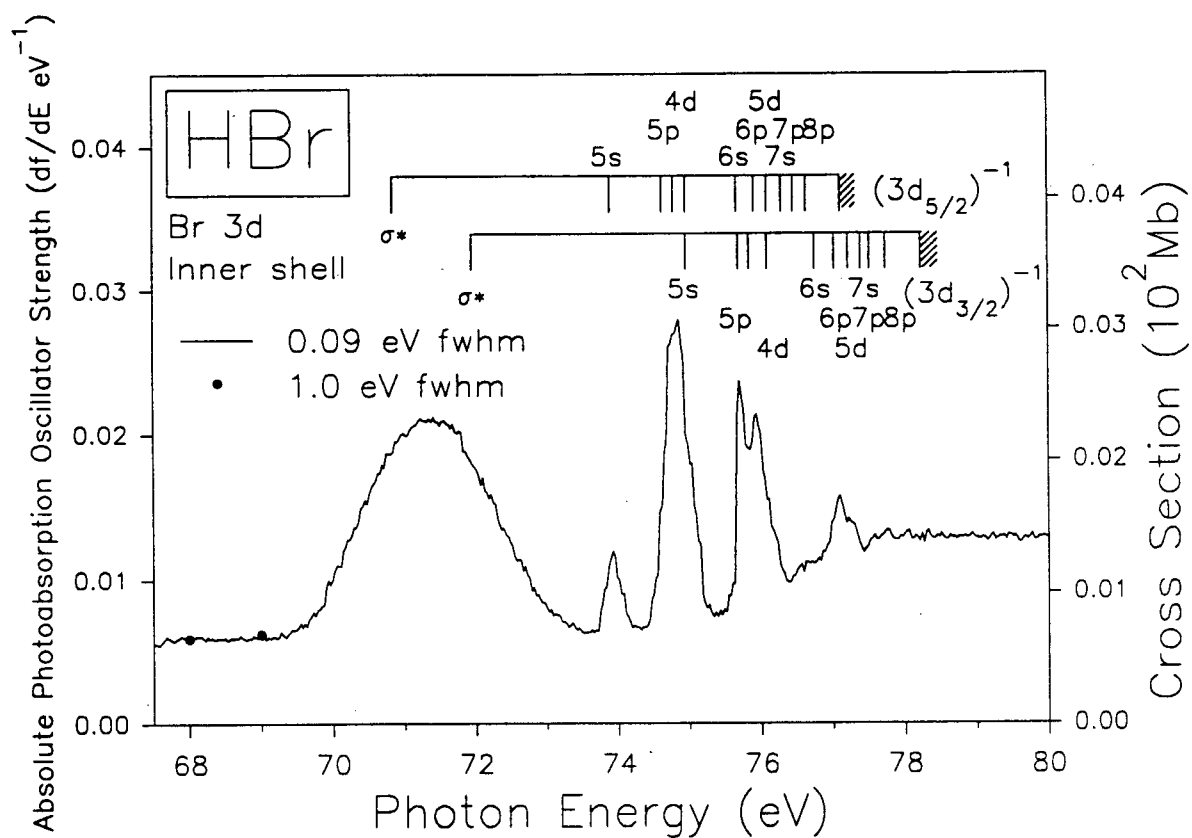
Figure 5.5: Absolute photoabsorption oscillator strengths for the Br 3d inner shell region of

HBr, obtained with high resolution (0.1 eV fwhm). Peak assignments are from reference [47].

Table 5.2: Integrated oscillator strengths (cross sections) for selected energy ranges in the Br 3d

inner shell of HBr, with and without estimated contributions from the valence shell continuum.

Energy Range	df/dE (Mb)	
	With Valence	Without Valence
69.19-73.52	6.38	3.57
73.64-74.31	0.62	0.19
74.31-75.37	1.77	1.07
75.48-76.40	1.54	0.95
76.40-77.44	1.43	0.75
77.44-80.02	3.66	1.99

Table 5.3: Appearance potentials for the molecular and dissociative ions produced from HBr.

Ion	Appearance Potential			
	Experiment		Calculated	
	Present Work	ref. [11]	ref. [97][a]	ref. [98][a]
HBr^+	10.0	10.0	11.66	
Br^+	14.0	15.0	15.606	15.669
H^+	19.0	21.0	17.39	17.37
Br^{2+}	36.0			

[a] Derived from heats of formation of the ionic and neutral species

table 5.3, together with their appearance potentials. The two isotopes of bromine (masses 79 and 81) occur with nearly equal natural abundance (49% and 51%, respectively). The close spacing of the two Br^+ and the two HBr^+ peaks (all between masses 79-82) precluded complete resolution at the low mass resolution of the instrument. However with careful peak fitting procedures it was possible to separate and integrate the individual peaks. Two gaussian peaks (necessary to model the asymmetric TOF peaks) of equal width were fitted to each isotopic peak of HBr^+ and Br^+. The resulting peak areas reflected the bromine natural abundances. Typical peak fits are shown in figure 5.6 at equivalent photon energies of 12 eV (figure 5.6(a)), below, and at 20 eV (figure 5.6(b)), above the Br^+ appearance potential respectively. For each Br containing ion the 79 Br and 81 Br contributions were summed. The ions detected below 66 eV are H^+, Br^+, Br^{2+}, and HBr^+, as can be seen in the TOF mass spectra shown in figure 5.7 at 20 and 51.5 eV.

Photoion branching ratios, as a percentage of total photoionization, were obtained from integration of the peaks in the baseline subtracted TOF mass spectra. The resulting ratios are shown in figure 5.8 and given numerically in table 5.5. The branching ratios for the molecular ion HBr^+ show (figure 5.7) an initially steep decrease, with some levelling off occurring above 25 eV. The opposite is observed for Br^+, where there is an initially steep increase above the appearance potential and a second rise in the region of the $B^2\Sigma$ (i.e. $(7\sigma)^{-1}$) onset. The Br^+ branching ratios then appear to level off somewhat above 30 eV. The dissociative ions H^+ and Br^{2+} both show slow increases from their appearance potentials up to the Br 3d threshold. No doubly charged HBr^{2+} is observed. In marked contrast to the situation for HCl the photoion branching ratios for HBr do not level off. This is to be expected since the EMS [74] studies clearly show that the $B^2\Sigma$ ionization manifold extends to at least 50 eV and possibly beyond. In this regard it should be
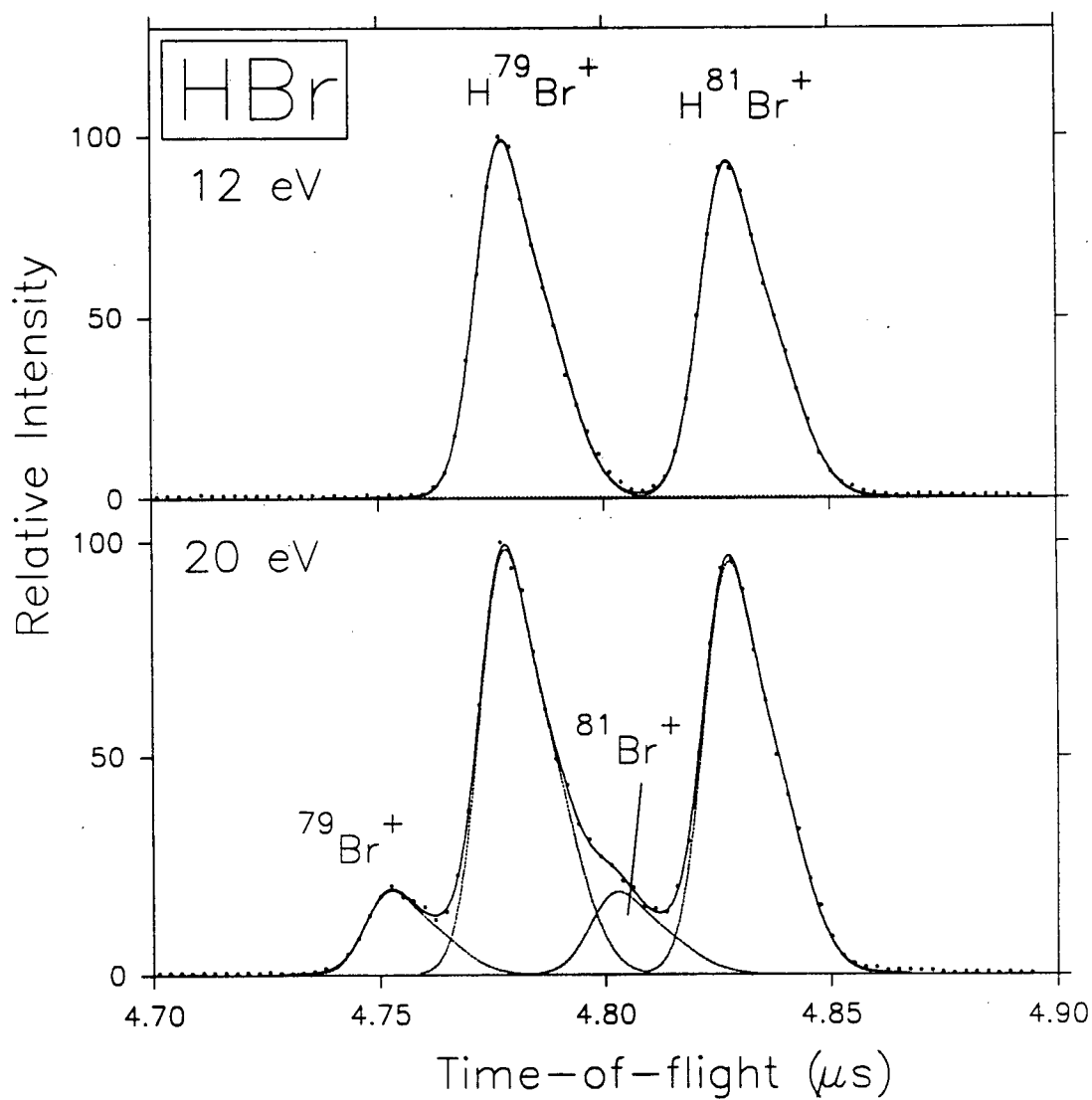
Figure 5.6: Typical peak fits used to resolve isotopic HBr⁺, Br⁺ peaks in the HBr time-of-flight

mass spectra, at equivalent photon energies of (a) 12 eV, and (b) 20 eV.
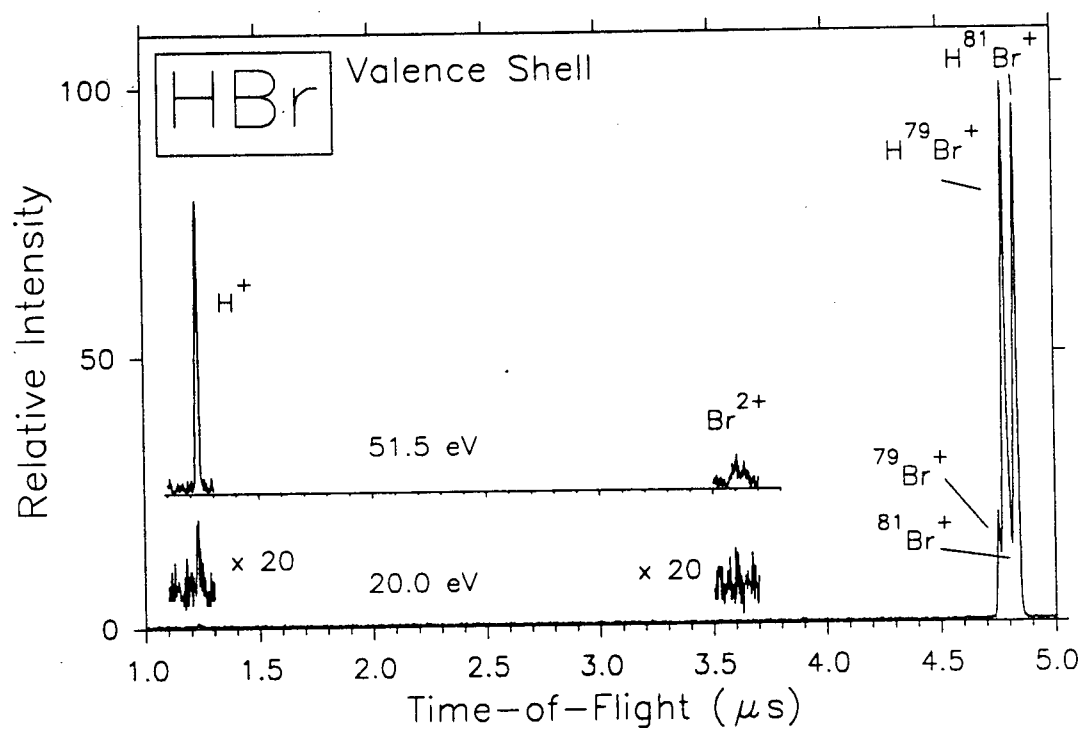
Figure 5.7: Time-of-flight mass spectra at 20 and 51.5 eV energy loss in the valence shell region

of HBr
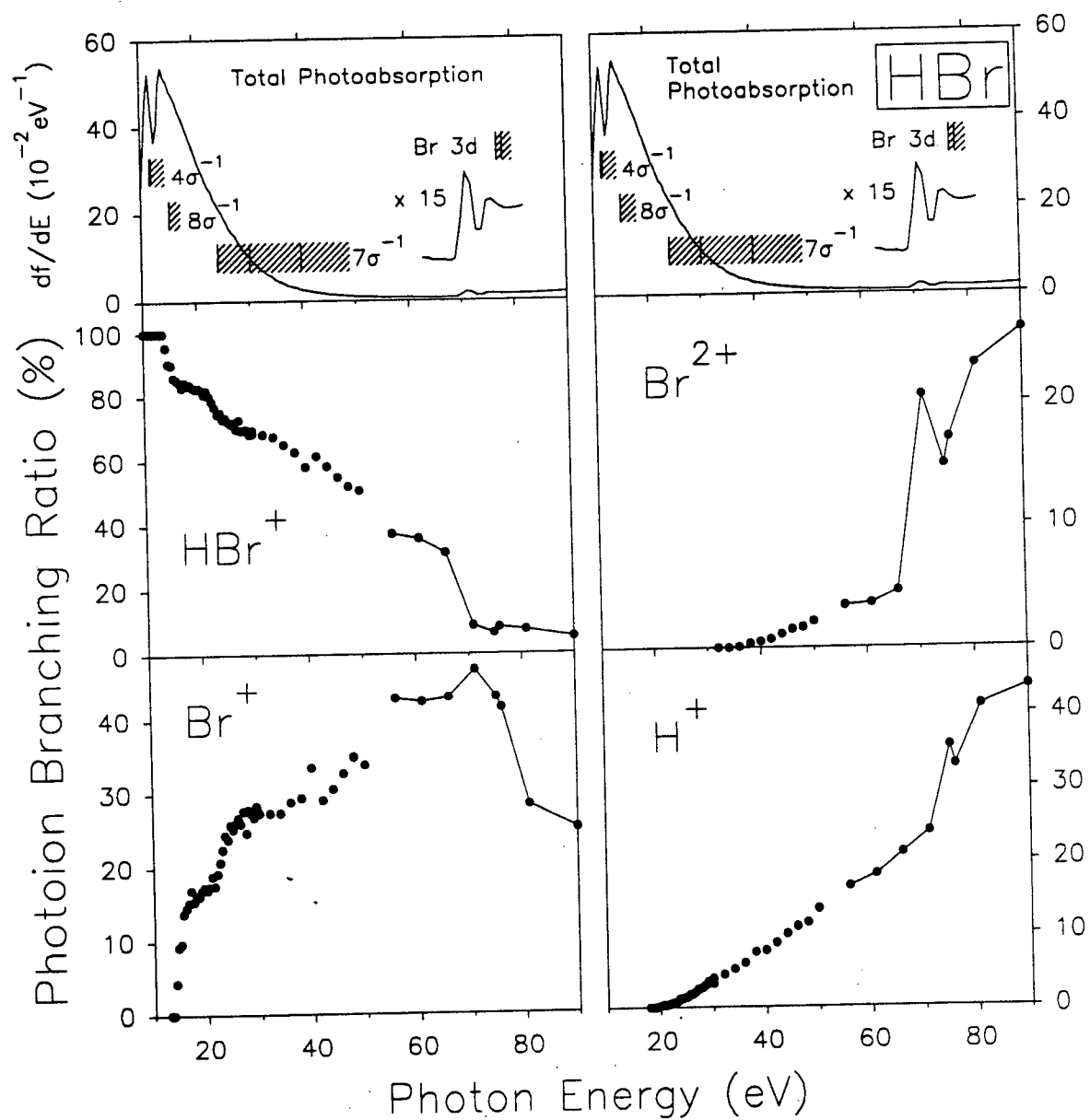
Figure 5.8: Photoion branching ratios for the molecular and dissociative photoionization of HBr, as a percentage of total photoionization. The top panes show the absolute photoabsorption spectrum.

noted that the breakdown model [8] predicts that the fragmentation ratios will only level off at photon energies *above* the upper limit of the Franck-Condon region for the most tightly bound orbital.

In the previous work on HBr in this laboratory [11], photoion branching ratios were obtained up to 40 eV. As discussed in the case of HCl (section 4.2.3), there are some concerns with the reliability and accuracy of the results from the earlier work, especially with regard to the efficiency of the ion detector as a fucntion of m/e. This detector has since been replaced by a microchannel plate device [28] (see section 4.2.3). The photoion branching ratios obtained earlier [11] have been appropriately corrected for the response of the Johnston multiplier and compared with the photoion branching ratios obtained in the present work. As can be seen in figure 5.9, the two sets of branching ratios for the molecular ion agree reasonably well, while there are significant differences in the dissociative ion branching ratios. For HBr^+ and Br^+, the large local differences in the 16-23 eV region and of H^+ at all energies are surprising and not understood.

Absolute partial photoionization oscillator strengths were obtained above 20 eV (where η_i can reasonbly be assumed to by unity) from the product of the absolute photoabsorption and the photoion branching ratio for the molecular and each dissociative ion. Difficulties were encountered in determining the photoionization efficiency during the HBr TOF measurements due to an intermittent computer problem which creates an inconsistency in the time scale over long data collection runs. This problem (only discovered after the measurements were completed) does not however affect the relative peak areas in the TOF mass spectra, and thus does not affect the photoion branching ratios. For these reasons, partial photoionization oscillator strengths have only been obtained above 20 eV (where η_i =1). The absolute partial oscillator strengths thus
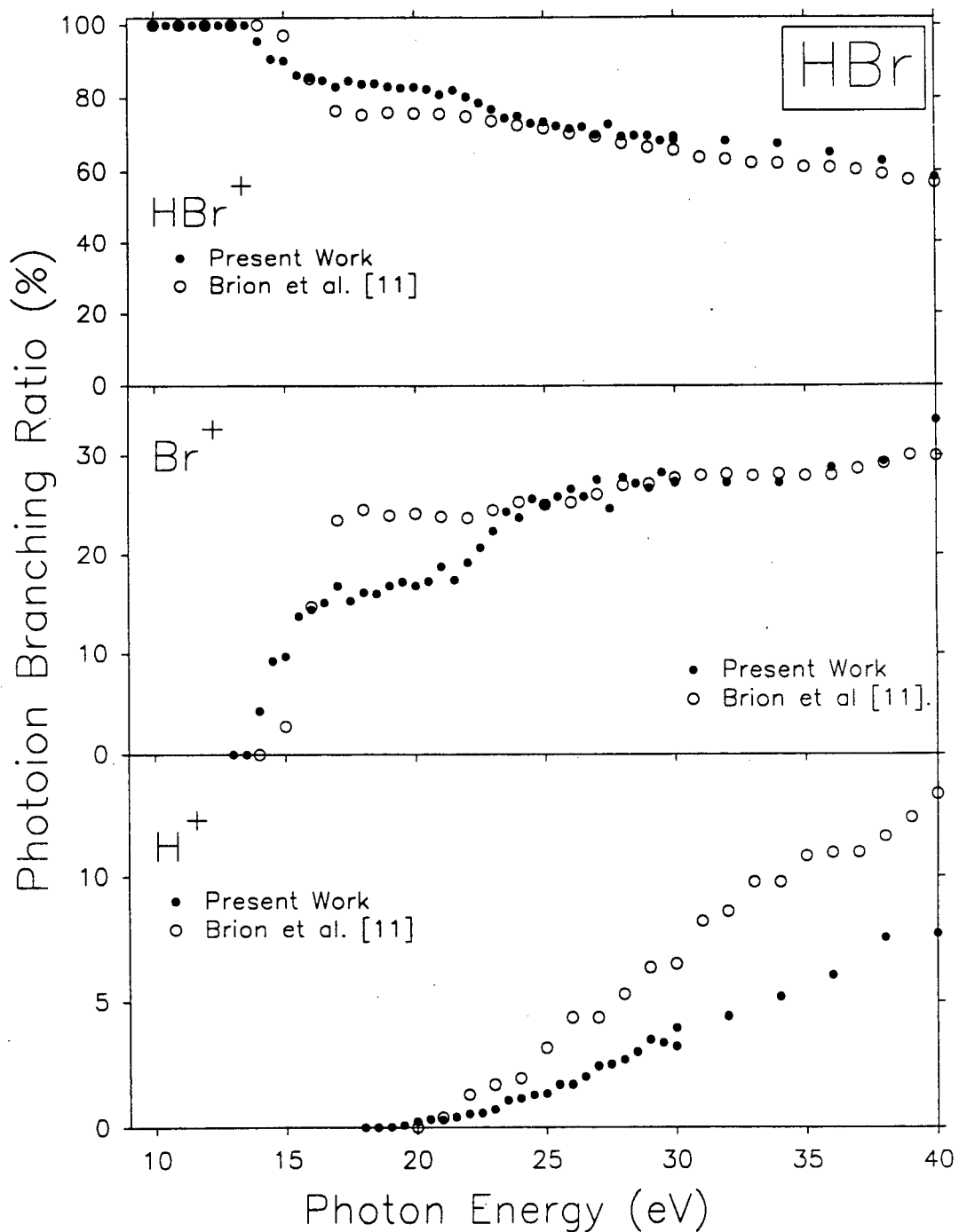
Figure 5.9: Comparison of photoion branching ratios obtained in the present work with those reported in the previous dipole (e,e+ion) study by Brion et al. [11].

obtained are presented graphically in figure 5.10, and numerically in table 5.6. As can be seen

from figure 5.10, the PPOS's for HBr^+ and Br^+ decrease steeply above 20 eV, while H^+ has a

broad peak with a maximum at 29 eV. Only a very small amount of Br^{2+} oscillator strength is

present in the valence shell above 35 eV. The Br^{2+} is formed in the valence shell region by direct

dissociative double photoionization and/or via VVV Auger processes. These trends will be

discussed further in section 5.2.4 below.

5.2.4 Dipole-Induced Breakdown Pathways of HBr

As discussed previously (section 4.2.4), the dipole induced breakdown of a molecule can

be investigated by considering together the partial oscillator strengths for the molecular and

dissociative photoionization with those for production of the electronic ion states. This is because

the total absolute photoionization oscillator strength distribution can be partitioned into the partial

oscillator strengths for molecular and dissociative photoionization or into the contributions from

the electronic ion state partial oscillator strengths (see equations 2.3.4 and 2.3.6 respectively).

Also, the partial oscillator strengths for the molecular or any dissociative ion can be partitioned

into contributions from the various electronic ion state PPOS's [2, 8, 77]. The dipole induced

breakdown of HBr has therefore been investigated in the present work by attempting to fit linear

combinations of the electronic ion state partial oscillator strengths to the partial oscillator strength

spectra for the molecular and each dissociative ion. In order to accomplish this, the electronic

state PPOS's from the previous work [11] were re-evaluated above 20 eV by taking the triple

product of the absolute photoabsorption from the present work, the photoelectron branching

ratios from the previous work, and an ionization efficiency equal to unity. The electronic state

PPOS's thus obtained are shown in figure 5.11 and numerically in table 5.7.
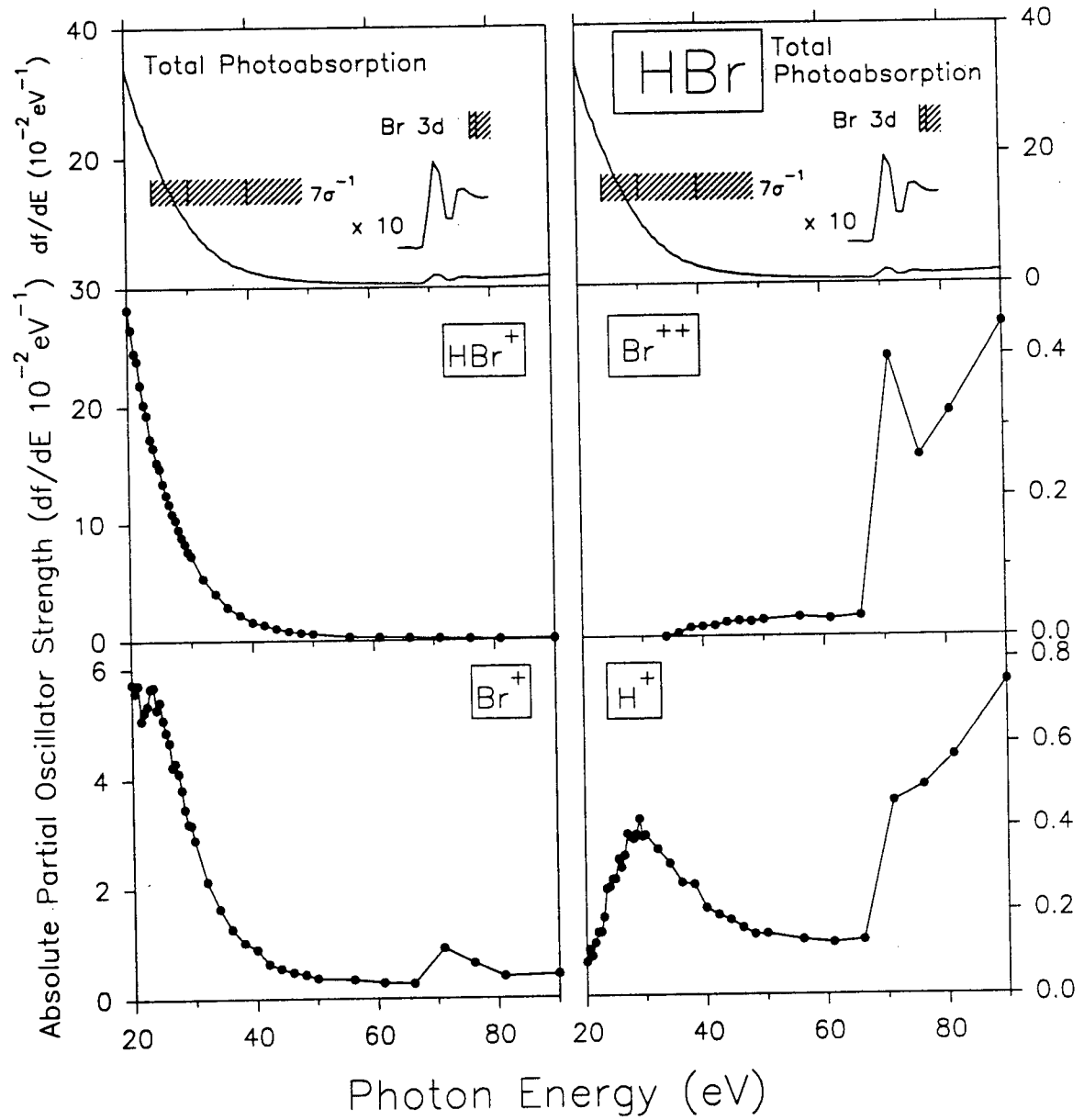
Figure 5.10: Absolute partial photoionization oscillator strengths for the molecular and dissociative ionic states produced by photoionization of HBr. The top panels show the absolute photoabsorption spectrum.
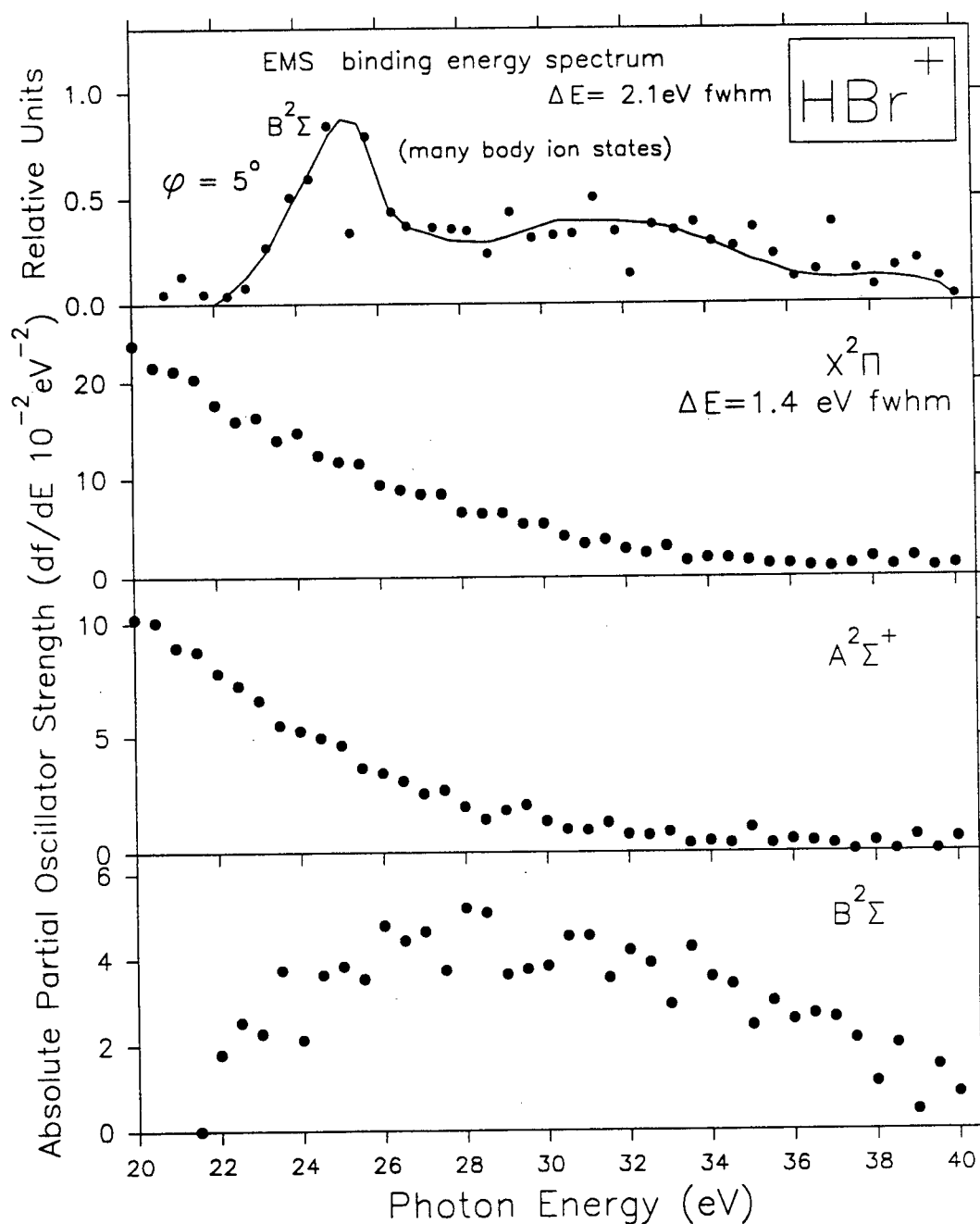
Figure 5.11: Electronic ion state partial oscillator strengths obtained from photoelectron dipole (e,2e) branching ratios reported by Brion et al. [11] and the presently reported photoabsorption oscillator strengths. The binding energy spectrum (top panel), in the region of the HBr^+, $B^2\Sigma$ many body manifold, is taken from low resolution EMS measurements [74].

The spectra in figure 5.12 show the best fit linear combinations of the electronic state PPOS's to the molecular (HBr$^+$, figure 5.12(b)) and total dissociative (Br$^+$ + H$^+$, figure 5.12(c)) ion state PPOS's. For HBr$^+$, the best linear combination was given by (1.0X$^2\Pi$ + 0.4A$^2\Sigma^+$ + 0.4B$^2\Sigma$). Thus the molecular ion partial oscillator strength arises mostly from the X$^2\Pi$ state, with small contributions from the A$^2\Sigma^+$ and B$^2\Sigma$ states. Considering the fragment ion appearance potentials (see table 5.3) and the ionization potentials (see section 5.2.1), Br$^+$ must first arise from the A$^2\Sigma^+$ state of HBr$^+$. Similarly, H$^+$ can only be formed from the B$^2\Sigma$ ionization manifold. Given the statistics in the two different measurements, the remaining electronic state PPOS is fairly well matched by the total dissociative (Br$^+$ + H$^+$) ion state PPOS, as can be seen in figure 5.12(c).

The total dissociative photoionization can be partitioned into individual contributions from Br$^+$ and H$^+$, as can be seen in figure 5.13(b) and (c). The best fit linear combination for Br$^+$ is given by (0.6A$^2\Sigma^+$ + 0.5B$^2\Sigma$). As can be seen in figure 5.13(b), below 21.5 eV Br$^+$ arises only from the A$^2\Sigma^+$ electronic state. Again it is observed that the contribution from the B$^2\Sigma$ state corresponds to the B$^2\Sigma$ state onset in the PES spectrum [74] shown in figure 5.13(a). For the partial oscillator strength of H$^+$, the remaining oscillator strength (10%) from the B$^2\Sigma$ electronic state gives a reasonable fit, considering the small magnitude of the partial oscillator strength and the respective data statistics. The breakdown pathways above 40 eV in the valence shell and in the Br 3d region suggested by the present work are summarized in figure 5.14. Photoelectron-photoion coincidence studies would enable a more detailed and accurate analysis of the processes involved in photoionization in this region.
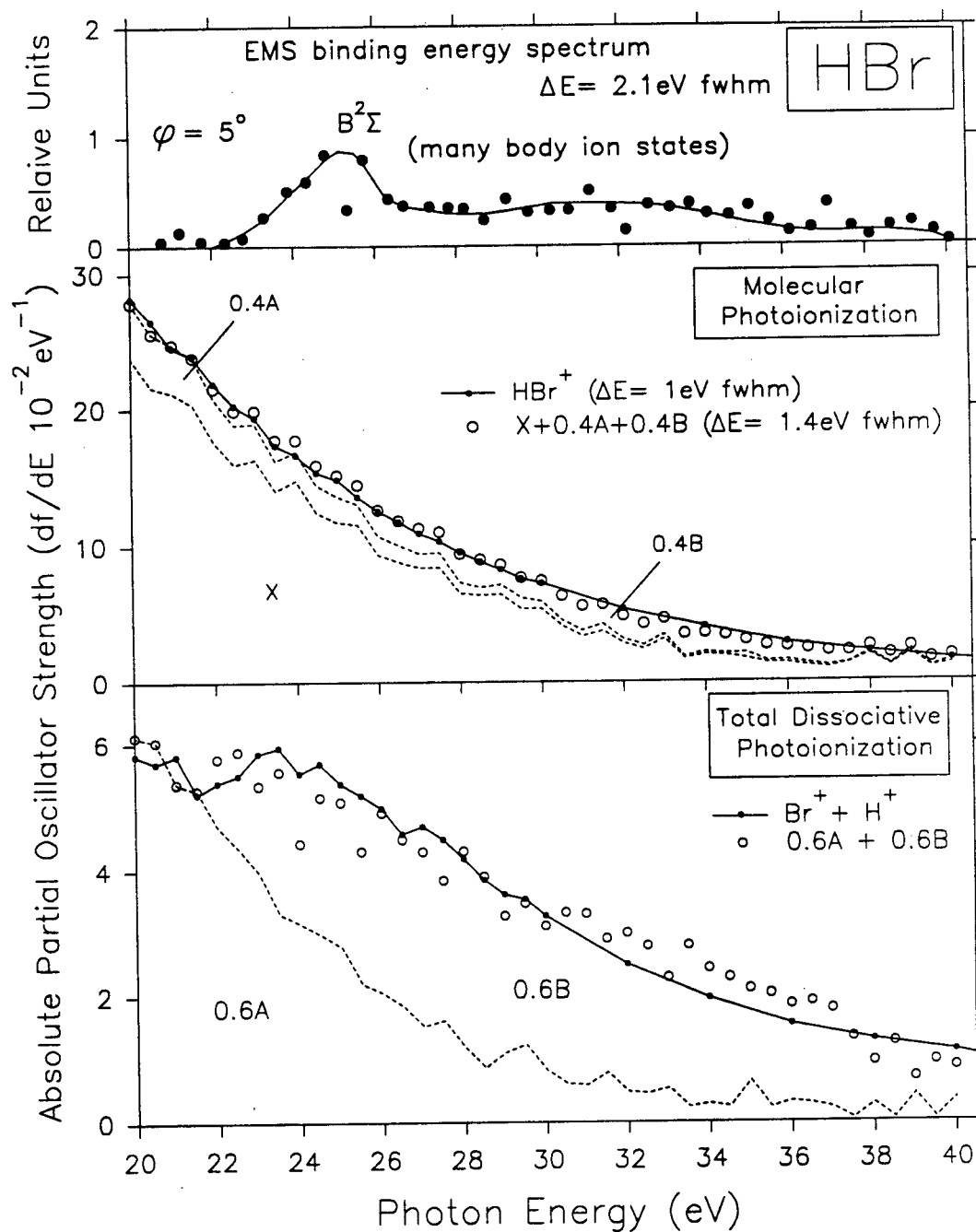
Figure 5.12: Absolute partial photoionization oscillator strengths for the molecular and total dissociative photoionization of HBr, with best fit linear combinations of contributions from the electronic ion state partial oscillator strengths. The top panel shows the EMS spectrum obtained at low resolution by Suzuki et al. [74].
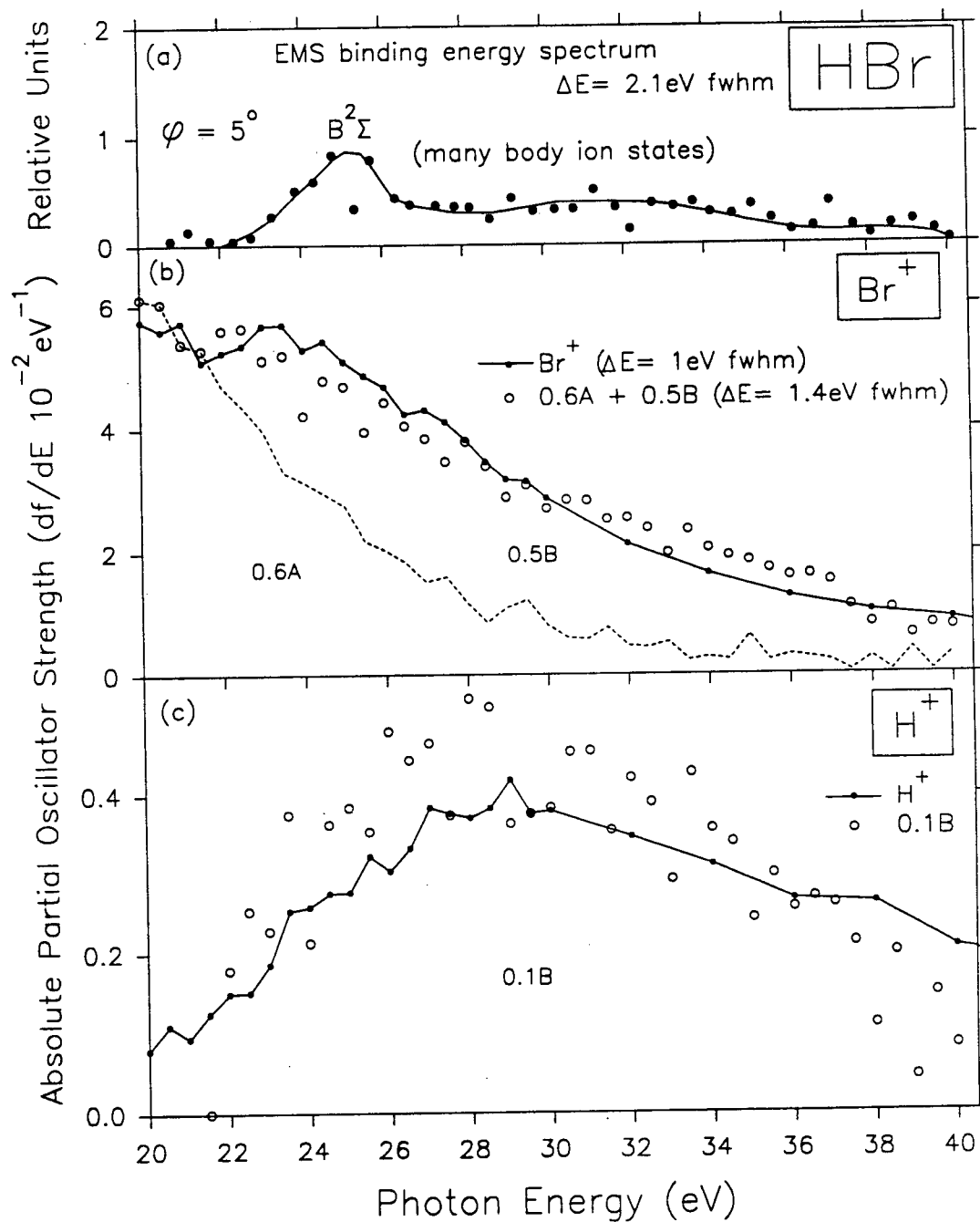
Figure 5.13: Absolute partial photoionization oscillator strengths for the dissociative ions Br[+]

and H^{+}, with best fit linear combinations of contributions from electronic ion state partial

oscillator strengths. The top panel shows the EMS spectrum obtained by Brion et al. [74].
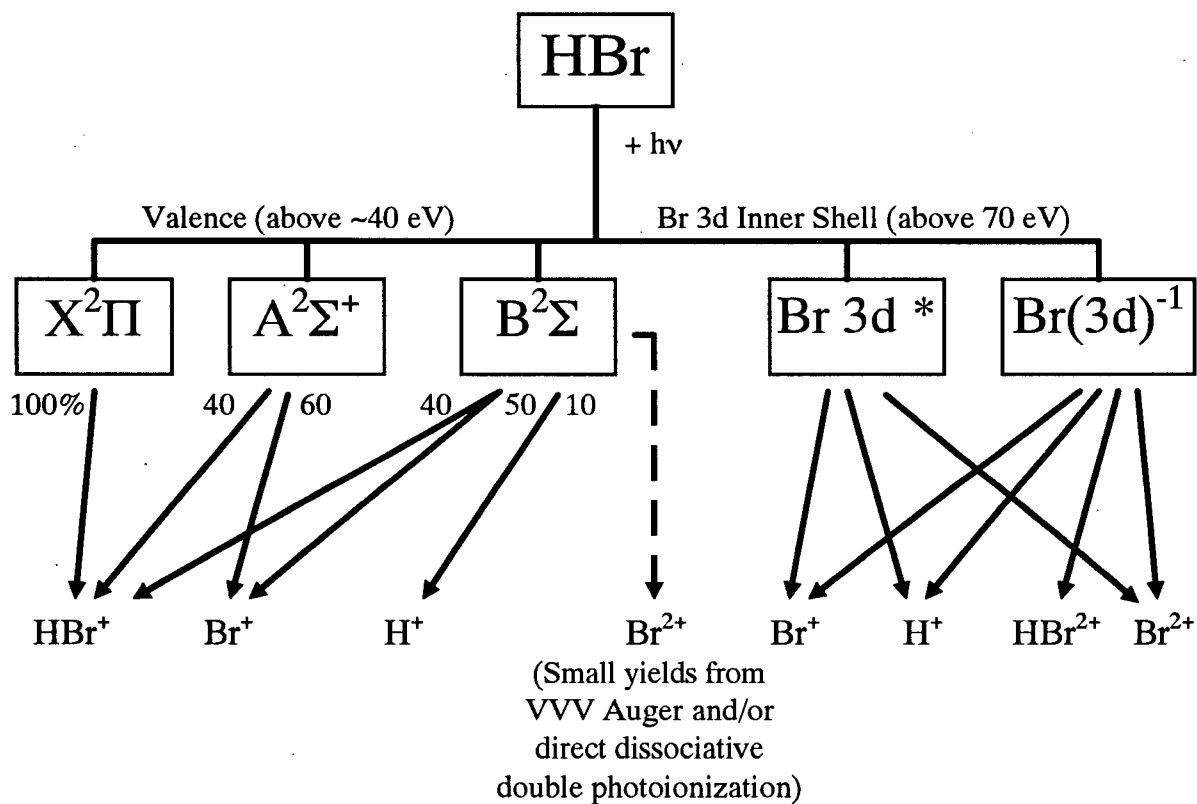
Figure 5.14. Dipole ionic photofragmentation breakdown pathways of HBr in the VUV and soft

X-ray regions.

5.2.5 Photoionization Measurements in the Br 3d Inner Shell Region of HBr

Time-of-flight mass spectra were also obtained in the Br 3d inner shell excitation and ionization region of HBr at selected equivalent photon energies at 1 eV fwhm energy resolution. Typical TOF spectra are shown in figure 5.15 at energies of 66 eV (inner valence), 71, 75, and 91 eV (selected Br 3d regions). Note that the ion yield scale is relative to the *tallest* peak, which is not necessarily the peak with the largest area. At 66 eV, in the valence shell continuum below the Br 3d threshold, HBr^+ (m/e = 80, 82) is the highest peak. There is a large amount of H^+ present, but very little Br^{2+}. At 71 eV, in the middle of the strong $3d \to \sigma^*$ transition (see figure 5.1, 1 eV fwhm, and figure 5.5, 0.1 eV fwhm), the HBr^+ peaks are substantially reduced, while the Br^+, Br^{2+} peaks are increasing in intensity. The width of the H^+ peak is appreciably broadened compared with the situation in the valence shell pre-edge region at 66 eV. At 75 eV, in the Rydberg excitation region, the relative intensities of the HBr^+, Br^+, and Br^{2+} peaks decrease, while H^+ increases. At 91 eV, well into the Br 3d ionization continuum, HBr^+ and Br^+ further decrease in relative intensity and Br^{2+} increases. In addition, a small amount of the doubly charged HBr^{2+} is formed, although no doubly charged molecular ions are observed at any of the lower energy TOF mass spectra. At 91 eV, the H^+ peak shows further broadening, indicating high kinetic energy protons probably formed in the Coulomb explosion of doubly charged ions (i.e. HBr^{2+}).

Photoion branching ratios for the Br 3d inner shell region are given in figure 5.8 and table 5.5. At the Br 3d excitation threshold, the branching ratio for HBr^+ decreases, while those for H^+, Br^+, and Br^{2+} increase. For each of H^+, Br^+, Br^{2+}, there is a peak ~71 eV which corresponds to the $3d \to \sigma^*$ virtual valence transition. This is apparently due to processes involving dissociative autoionization (resonance Auger decay [56]) of neutral excited states of HBr down to $H^+ + Br$,
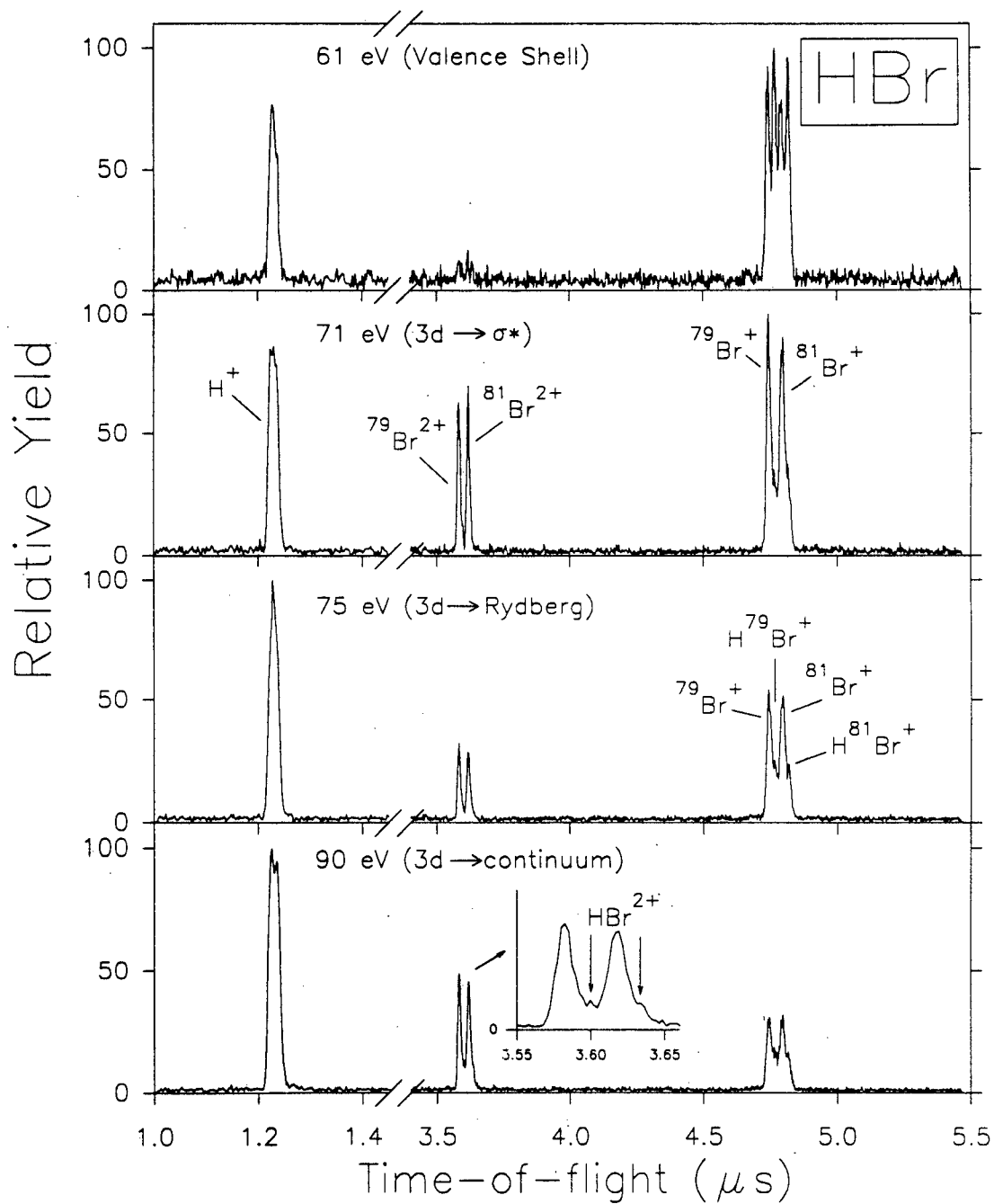
Figure 5.15: Time-of-flight mass spectra of HBr at selected energies in the inner valence and Br

3d inner shell regions (1 eV fwhm).

H + Br^+, and/or ionization to doubly charged HBr^{2+}, which rapidly dissociates to form H^+ + Br^+ (Coulomb explosion) or to Br^{2+} + H. In the 3d ionization continuum (91 eV) the relative yields of HBr^+ and Br^+ further decrease, while H^+ and Br^{2+} increase. In addition HBr^{2+} appears for the first time and in low yield (see figure 5.15). The appearance of HBr^{2+} is consistent with the onset of Auger processes expected in the 3d ionization continuum but not lower energies in the 3d excitation region. The Auger processes may lead to doubly charged HBr^{2+} and Br^{2+} ions and also Coulomb explosion of HBr^{2+} to give H^+ + Br^+. The slightly increased width of the H^+ peak (figure 5.15) is evidence for the latter process and/or dissociative single ionization (or autoionization) to H^+ + Br.

Partial photoionization oscillator strengths (PPOS's) for molecular and dissociative photoionization in the Br 3d inner shell region are shown in figure 5.10 above. In this energy region the remaining HBr^+ oscillator strength is formed essentially from valence shell processes only. The Br^+ PPOS shows a small peak at around 71 eV, corresponding to the strong 3d→σ* transition (figures 5.1 and 5.5), as already discussed above with reference to the photoion branching ratios. The H^+ and Br^{2+} PPOS's increase at the Br 3d excitation threshold. H^+ continues to increase in the Rydberg excitation and ionization continuum regions, as also discussed above with reference to the branching ratios in (figure 5.8). In contrast Br^{2+} has a maximum at 71 eV, which drops in the Rydberg region before increasing again in the 3d ionization continuum where a small amount of HBr^{2+} (see figure 5.15) is also formed.

Table 5.4: Absolute differential photoabsorption oscillator strengths for valence shell and Br 3d

inner shell regions of HBr (1 eV fwhm).

Total Photoabsorption Oscillator Strength (df/dE)							
eV	$10^{-2}eV^{-1}$	eV	$10^{-2}eV^{-1}$	eV	$10^{-2}eV^{-1}$	eV	$10^{-2}eV^{-1}$
5.0	0.60	19.5	35.95	34.0	6.01	57.0	0.77
5.5	0.57	20.0	33.99	34.5	5.69	58.0	0.74
6.0	1.01	20.5	32.22	35.0	5.15	59.0	0.71
6.5	1.75	21.0	30.39	35.5	4.77	60.0	0.69
7.0	2.26	21.5	29.10	36.0	4.42	61.0	0.68
7.5	2.46	22.0	27.28	36.5	4.27	62.0	0.66
8.0	7.02	22.5	25.75	37.0	3.95	63.0	0.65
8.5	20.07	23.0	25.22	37.5	3.51	64.0	0.64
9.0	18.68	23.5	23.28	38.0	3.49	65.0	0.61
9.5	12.54	24.0	22.16	38.5	3.21	66.0	0.61
10.0	25.86	24.5	21.03	39.0	3.15	67.0	0.61
10.5	36.97	25.0	20.21	39.5	2.90	68.0	0.59
11.0	46.39	25.5	18.75	40.0	2.68	69.0	0.63
11.5	52.35	26.0	17.55	41.0	2.44	70.0	1.18
12.0	44.67	26.5	16.35	42.0	2.17	71.0	1.93
12.5	36.76	27.0	15.61	43.0	1.95	72.0	1.75
13.0	40.48	27.5	14.86	44.0	1.78	73.0	1.05
13.5	50.17	28.0	13.73	45.0	1.59	74.0	1.05
14.0	53.83	28.5	12.72	46.0	1.45	75.0	1.49
14.5	51.53	29.0	11.92	47.0	1.38	76.0	1.51
15.0	50.34	29.5	11.18	48.0	1.25	77.0	1.44
15.5	48.62	30.0	10.57	49.0	1.16	78.0	1.39
16.0	47.43	30.5	9.66	50.0	1.08	79.0	1.37
16.5	46.07	31.0	8.89	51.0	1.00	80.0	1.38
17.0	44.27	31.5	8.58	52.0	0.97	81.0	1.39
17.5	42.65	32.0	7.82	53.0	0.92	82.0	1.41
18.0	41.07	32.5	7.24	54.0	0.88	83.0	1.39
18.5	39.33	33.0	6.92	55.0	0.83	84.0	1.46
19.0	37.31	33.5	6.30	56.0	0.79	85.0	1.49

Table 5.4 (continued): Absolute differential photoabsorption oscillator strengths for valence

shell and Br 3d inner shell regions of HBr (1 eV fwhm).

Total Photoabsorption Oscillator Strength (df/dE)							
eV	$10^{-2}eV^{-1}$	eV	$10^{-2}eV^{-1}$	eV	$10^{-2}eV^{-1}$	eV	$10^{-2}eV^{-1}$
86	1.53	130	4.23	188	4.93	246	4.43
87	1.58	132	4.35	190	5.00	248	4.39
88	1.59	134	4.36	192	5.00	250	4.46
89	1.66	136	4.36	194	5.00	252	4.43
90	1.71	138	4.50	196	4.98	254	4.34
91	1.81	140	4.53	198	4.93	256	4.43
92	1.88	142	4.56	200	4.96	258	4.43
93	1.90	144	4.63	202	4.94	260	4.34
94	1.95	146	4.69	204	4.93	262	4.38
95	1.97	148	4.67	206	4.99	264	4.32
96	2.09	150	4.71	208	4.96	266	4.23
97	2.06	152	4.70	210	4.81	268	4.16
98	2.19	154	4.75	212	4.89	270	4.15
99	2.27	156	4.72	214	4.79	272	4.20
100	2.34	158	4.69	216	4.85	274	4.23
102	2.46	160	4.75	218	4.74	276	4.24
104	2.60	162	4.78	220	4.80	278	3.91
106	2.76	164	4.70	222	4.70	280	4.04
108	2.90	166	4.80	224	4.65	282	4.03
110	3.06	168	4.77	226	4.69	284	4.03
112	3.19	170	4.76	228	4.74	286	3.91
114	3.33	172	4.67	230	4.63	288	3.93
116	3.47	174	4.70	232	4.57	290	3.82
118	3.58	176	4.72	234	4.55	292	3.82
120	3.69	178	4.69	236	4.48	294	3.78
122	3.88	180	4.75	238	4.51	296	3.89
124	3.94	182	4.71	240	4.37	298	3.72
126	4.10	184	4.89	242	4.62	300	3.61
128	4.13	186	4.99	244	4.48		

Table 5.5 Photoion branching ratios for the molecular and dissociative photoionization of HBr, as a percentage of total photoionization.

Photon Energy eV	Photoion Branching Ratio (%)			
	HBr^+	Br^+	Br^{2+}	H^+
10.0	100.00			
10.5	100.00			
11.0	100.00			
11.5	100.00			
12.0	100.00			
12.5	100.00			
13.0	100.00			
13.5	100.00			
14.0	95.66	4.34		
14.5	90.71	9.29		
15.0	90.29	9.71		
15.5	86.25	13.75		
16.0	77.03	22.97		
16.5	84.83	15.17		
17.0	83.11	16.89		
17.5	84.67	15.34		
18.0	83.78	16.22		
18.5	83.96	16.04		
19.0	83.08	16.89		0.03
19.5	82.62	17.29		0.09
20.0	82.89	16.88		0.23
20.5	82.33	17.33		0.34
21.0	80.87	18.82		0.31
21.5	82.09	17.48		0.43
22.0	80.26	19.19		0.55
22.5	78.66	20.75		0.59
23.0	76.81	22.45		0.74
23.5	74.51	24.41		1.09

Table 5.5. (continued): Photoion branching ratios for the molecular and dissociative photoionization of HBr, as a percentage of total photoionization.

Photon Energy eV	Photoion Branching Ratio (%)			
	HBr^+	Br^+	Br^{2+}	H^+
24.0	75.01	23.83		1.16
24.5	72.97	25.72		1.31
25.0	73.43	25.20		1.37
25.5	72.32	25.95		1.72
26.0	71.57	26.70		1.73
26.5	72.02	25.95		2.03
27.0	69.94	27.60		2.46
27.5	72.75	24.72		2.53
28.0	69.48	27.82		2.70
28.5	69.73	27.26		3.01
29.0	69.71	26.78		3.51
29.5	68.31	28.32		3.37
30.0	69.01	27.40		3.59
32.0	68.22	27.34		4.43
34.0	67.46	27.35		5.19
36.0	65.03	28.83	0.10	6.04
38.0	62.71	29.42	0.35	7.52
40.0	58.23	33.57	0.51	7.69
42.0	61.45	29.08	0.70	8.77
44.0	58.32	30.61	1.09	9.98
46.0	54.84	32.76	1.47	10.92
48.0	51.93	34.96	1.65	11.47
50.0	50.68	33.87	2.13	13.32
56.0	37.29	42.90	3.43	16.38
61.0	35.83	42.48	3.61	18.08
66.0	31.34	43.05	4.61	21.00
71.0	8.74	46.86	20.58	23.81
75.0	6.44	43.10	14.90	35.57
76.0	8.40	41.67	17.04	32.89
81.0	7.46	28.37	23.10	41.07
90.0	5.16	25.15	26.00	43.70

Table 5.6: Absolute partial differential oscillator strengths for the molecular and dissociative photoionization of HBr.

Photon Energy (eV)	Partial Differential Oscillator Strength ($10^{-2} eV^{-1}$)			
	HBr^+	Br^+	Br^{2+}	H^+
20.0	28.17	5.74		0.08
20.5	26.53	5.58		0.11
21.0	24.57	5.72		0.09
21.5	23.89	5.09		0.13
22.0	21.89	5.24		0.15
22.5	20.26	5.35		0.15
23.0	19.37	5.66		0.19
23.5	17.35	5.68		0.25
24.0	16.62	5.28		0.26
24.5	15.35	5.41		0.28
25.0	14.84	5.09		0.28
25.5	13.56	4.87		0.32
26.0	12.56	4.69		0.30
26.5	11.77	4.24		0.33
27.0	10.92	4.31		0.38
27.5	10.36	4.12		0.38
28.0	9.54	3.82		0.37
28.5	8.87	3.47		0.38
29.0	8.31	3.19		0.42
29.5	7.64	3.17		0.38
30.0	7.29	2.90		0.38
32.0	5.33	2.14		0.35
34.0	4.05	1.64	0.00	0.31
36.0	2.87	1.27	0.00	0.27
38.0	2.19	1.03	0.01	0.26
40.0	1.56	0.90	0.01	0.21

Table 5.6 (continued): Absolute partial differential oscillator strengths for the molecular and dissociative photoionization of HBr.

Photon Energy (eV)	Partial Differential Oscillator Strength ($10^{-2}eV^{-1}$)			
	HBr^+	Br^+	Br^{2+}	H^+
42.0	1.33	0.63	0.02	0.19
44.0	1.04	0.55	0.02	0.18
46.0	0.80	0.48	0.02	0.16
48.0	0.65	0.44	0.02	0.14
50.0	0.55	0.37	0.02	0.14
56.0	0.30	0.34	0.03	0.13
61.0	0.24	0.29	0.02	0.12
66.0	0.19	0.26	0.03	0.13
71.0	0.17	0.90	0.40	0.46
76.0	0.13	0.63	0.26	0.50
81.0	0.10	0.39	0.32	0.57

Table 5.7: Partial photoionization differential oscillator strengths for the production of electronic ion states of HBr.

Photon Energy (eV)	Partial Oscillator Strength[a] ($10^{-2}eV^{-1}$)		
	$X^2\Pi$	$A^2\Sigma^+$	$B^2\Sigma$
20.0	23.79	10.20	
20.5	21.59	10.06	
21.0	21.20	8.96	
21.5	20.32	8.79	0.00
22.0	17.66	7.83	1.79
22.5	15.96	7.26	2.53
23.0	16.32	6.62	2.28
23.5	14.01	5.52	3.75
24.0	14.77	5.26	2.13
24.5	12.44	4.96	3.63
25.0	11.74	4.63	3.84
25.5	11.57	3.64	3.54
26.0	9.36	3.40	4.79
26.5	8.86	3.06	4.43
27.0	8.44	2.53	4.64
27.5	8.44	2.67	3.74
28.0	6.55	1.98	5.20
28.5	6.41	1.43	5.09
29.0	6.47	1.82	3.64
29.5	5.39	2.03	3.76
30.0	5.39	1.35	3.83

a. Obtained using the dipole (e,2e) "photoelectron" branching ratios of reference [11] and the presently reported absolute photoabsorption oscillator strengths.

Table 5.7 (continued): Partial photoionization differential oscillator strengths for the production of the electronic ion states of HBr.

Photon Energy (eV)	Partial Oscillator Strength[a] (10^{-2}eV^{-1})		
	$X^2\Pi$	$A^2\Sigma^+$	$B^2\Sigma$
30.5	4.13	1.01	4.53
31.0	3.38	0.97	4.54
31.5	3.75	1.28	3.55
32.0	2.83	0.78	4.20
32.5	2.41	0.74	3.90
33.0	3.12	0.88	2.92
33.5	1.65	0.39	4.27
34.0	1.97	0.47	3.57
34.5	1.90	0.40	3.40
35.0	1.65	1.07	2.43
35.5	1.31	0.37	2.99
36.0	1.33	0.53	2.56
36.5	1.12	0.46	2.69
37.0	0.99	0.36	2.61
37.5	1.31	0.08	2.12
38.0	1.93	0.46	1.10
38.5	1.13	0.09	2.00
39.0	2.01	0.70	0.44
39.5	1.00	0.08	1.49
40.0	1.26	0.59	0.84

a. Obtained using the dipole (e,2e) "photoelectron" branching ratios of reference [11] and the presently reported absolute photoabsorption oscillator strengths.

Chapter 6

Photoabsorption Studies of Hydrogen Iodide

6.1 Introduction

Very little information is available for the photoabsorption of HI. A possible reason for the scarcity of studies involving HI is the difficulty in obtaining a pure sample because of disproportionation in the cylinder (i.e. 2HI $\leftrightarrow$ H$_2$ + I$_2$). In the present work, great care had to be taken in order to eliminate a large molecular hydrogen impurity present in the HI gas sample as well as signals due to desorption of HBr and HCl from the surfaces in the gas inlet system and the spectrometer. Repeated purgings and evacuations were necessary to obtain the spectrum of pure HI. Similar problems with impurities occurred in earlier photoabsorption studies of hydrogen fluoride [101].

To the best of our knowledge, very few *absolute* photoabsorption spectra of HI have been published. Roxlo and Mandl [35] reported absolute photoabsorption cross sections for HI in the region 5.4-7.3 eV. Romand [36] and Goodeve and Taylor [99] also obtained measurements in the same region. Wang et al. [100] measured the absolute photoabsorption spectrum of HI in the very limited energy range 10.4 to 11.1 eV. Other than in these restricted energy ranges the valence shell electronic absorption spectrum of HI is apparently unknown.

Several photoelectron spectroscopy studies have been performed on HI. Lempka et al. [49] obtained the HeI high resolution photoelectron spectrum of HI in the outer valence region. More recently, Adam et al. [102] used X-ray (hv=1487 eV), He I (hv=21.22 eV) and He II (hv=40.8 eV) radiation to investigate the inner valence photoelectron spectra of HI. Angle resolved PES studies and partial cross-sections obtained using synchrotron radiation have been reported by Bowering et al. [103], and by Carlson et al. [104]. Karlsson et al. [105] and Cutler et

115

al. [106] have measured the NVV Auger electron spectrum which involves the I 4d inner shell of

HI. Brion et al. [74] have measured binding energy spectra at low resolution over the entire

valence shell binding energy range using EMS spectroscopy.

Photoionization mass spectroscopy has been used to measure relative photoionization

cross sections for HI by Tsai and Baer [107], and by Eland and Berkowitz [108]. Absolute

photoionization cross sections have been calculated by Raseev et al. [109].

In the present work, absolute photoabsorption oscillator strengths (cross sections) for the

valence and I 4d inner shells of HI were obtained from 5 to 120 eV with low resolution (1.0 eV

fwhm), and from 5 to 60 eV with high resolution (0.05-0.1 eV fwhm) using dipole (e,e)

spectroscopy. To the best of our knowledge, no previous absolute photoabsorption

measurements of the I 4d inner shell region of HI have been reported.

6.2 Results and Discussion

6.2.1 Electronic Structure

The ground state electronic structure of HI can be represented as:

$$\text{core} \quad (4d)^{10} \quad (10\sigma)^2(11\sigma)^2(6\pi)^4 \quad (12\sigma)^0$$

$$\text{I 4d} \qquad\qquad \text{Valence} \qquad\qquad \text{Virtual Valence}$$
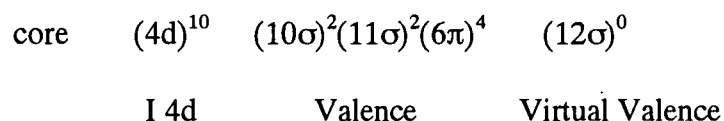
Ionization produces the following ionic states: $X^2\Pi_{3/2,1/2}$ from $(6\pi)^{-1}$, $A^2\Sigma^+$ from $(11\sigma)^{-1}$, and $B^2\Sigma$

from $(10\sigma)^{-1}$. Ionization potentials have been reported by Lempka et al. [49] to be 10.38 eV

$(X^2\Pi_{3/2})$, 11.05 eV $(X^2\Pi_{1/2})$, and 13.85 eV $(A^2\Sigma^+)$. Adam et al. [102] reported values of 21.2,

22.5, and 23.6 eV for the $B^2\Sigma$ many body states involved in the manifold [74]. Karlsson et al.

[105] reported the I 4d inner shell ionization potentials with values of 57.49 and 59.25 eV for the

I $4d_{5/2}$ and I $4d_{3/2}$ states respectively.

6.2.2 Photoabsorption Oscillator Strengths

6.2.2.1 Low-Resolution Photoabsorption Measurements of HI

The low resolution (1.0 eV fwhm) absolute photoabsorption oscillator strength spectrum of HI from 5 to 120 eV was obtained by normalizing the Bethe-Born converted relative spectrum obtained on the low resolution dipole (e,e) spectrometer (see section 3.2). The low energy onset of the I 4d inner shell (~50 eV) makes use of the VTRK sum rule unreliable (see discussion for HBr in section 5.2.2.1). Thus the S(-2) sum rule was used, together with an experimental static dipole polarizability (α_N) of 35.3 a.u. [64], to normalize the valence shell spectrum.

The low resolution valence shell spectrum (5-40 eV) and the long range spectrum (5-120 eV), including the valence shell and I 4d inner shell regions are shown in figure 6.1 below. The absolute oscillator strengths are given in table 6.3. In the valence shell spectrum (figure 6.1(a)), two broad peaks are visible at ~10 and 12.5 eV, as well as a pronounced shoulder around 8 eV. The high resolution spectra shown and discussed in sections 6.2.2.2 and 6.2.2.3 below provide more detailed investigations of the discrete valence shell and I 4d inner shell regions respectively. In the long range spectrum (figure 6.1(b)), the I 4d inner shell spectrum can be seen above 48 eV. The peak at ~51 eV corresponds to the strong 4d→σ* transition, and there is a very broad continuum resonance at ~ 92 eV. The energy scale of the spectrum was set by comparison with the high resolution spectrum, convoluted with 1 eV fwhm. A comparison (figure 6.2) of the low resolution (1 eV fwhm) and high resolution (0.05 eV fwhm, convoluted with 1 eV fwhm) gives a good consistency check of the absolute scale normalization of the spectra obtained using the two different instruments.
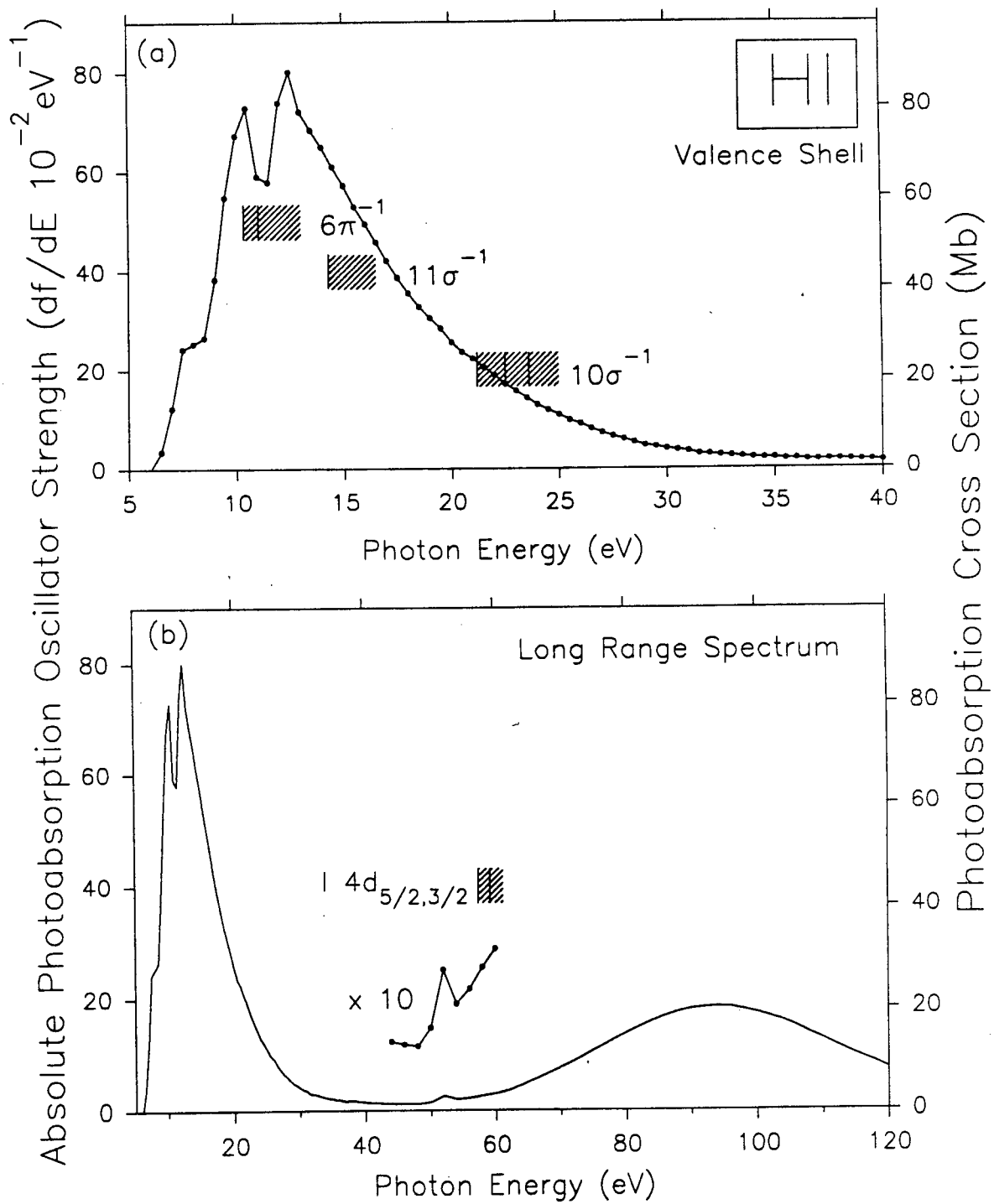
Figure 6.1: Absolute photoabsorption differential oscillator strengths (cross sections) for the valence and I 4d inner shell regions of HI. The ionization energies are from references [49, 102].
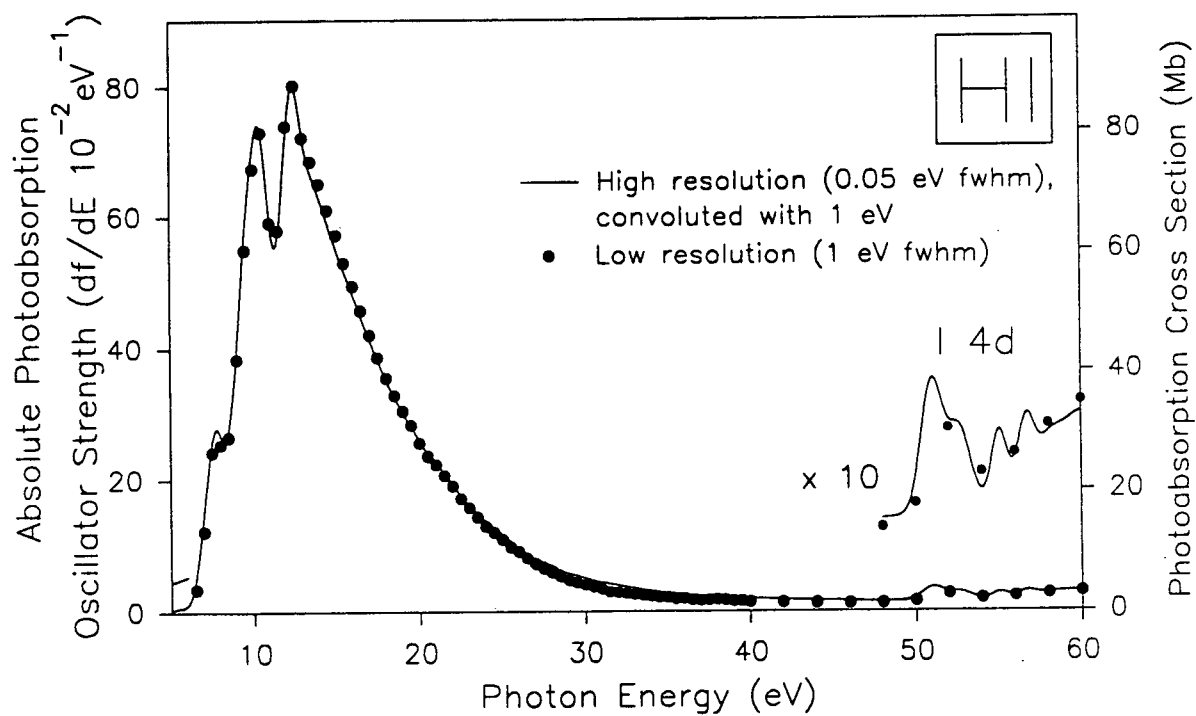
Figure 6.2: Comparison of low resolution (1 eV fwhm) and high resolution (0.05 eV fwhm, convoluted with 1 eV) absolute photoabsorption oscillator strengths for HI.

6.2.2.2 Valence Shell High Resolution Photoabsorption Measurements of HI

The high resolution (0.05 eV fwhm) valence shell (5-20 eV) absolute photoabsorption spectrum is shown in figure 6.3, with assignments from reference [110]. This represents the first full valence shell spectrum of HI to be reported. The spectrum was obtained from S(-2) sum rule normalization of the relative Bethe-Born converted energy-loss spectrum obtained on the high resolution dipole (e,e) spectrometer (see section 3.3). In the spectrum in figure 6.3(a), it is interesting to note the lack of discrete structure between 11 eV and 14 eV, i.e. between the $X^2\Pi_{1/2}$ and $A^2\Sigma^+$ limits. Integrated oscillator strengths (cross sections) for selected energy regions in the valence shell are given in table 6.1.

Only very few previously published *absolute* photoabsorption spectra [35, 36, 99, 100] of HI were found, and these are in very limited energy ranges. The most recent of these is by Roxlo and Mandl [35], who used a direct optical technique with a pulsed Xe_2 discharge lamp to measure the photoabsorption spectrum of HI from 230 to 170 nm (5.4-7.3 eV). A single transition at 176 nm (7.04 eV) was observed in their spectrum [35], with a peak height of ~4.2 Mb and an integrated cross section of 1.76 Mb, which is significantly lower than value of 12.38 Mb reported in the present work, as is shown in table 6.1. This large difference is evidence for large line saturation errors in the optical work of Roxlo and Mandl [35], which caused significant reduction of the sharp transition observed at ~7 eV.

Two other absolute photoabsorption studies were reported in the work by Roxlo and Mandl [35]: Romand [36] and Goodeve and Taylor [99], who studied the absorption spectrum of HI in the pre-edge outer valence region (below 8 eV). The spectrum reported by Romand shows a single transition at ~176 nm (~7eV) that is somewhat different in shape from that observed by
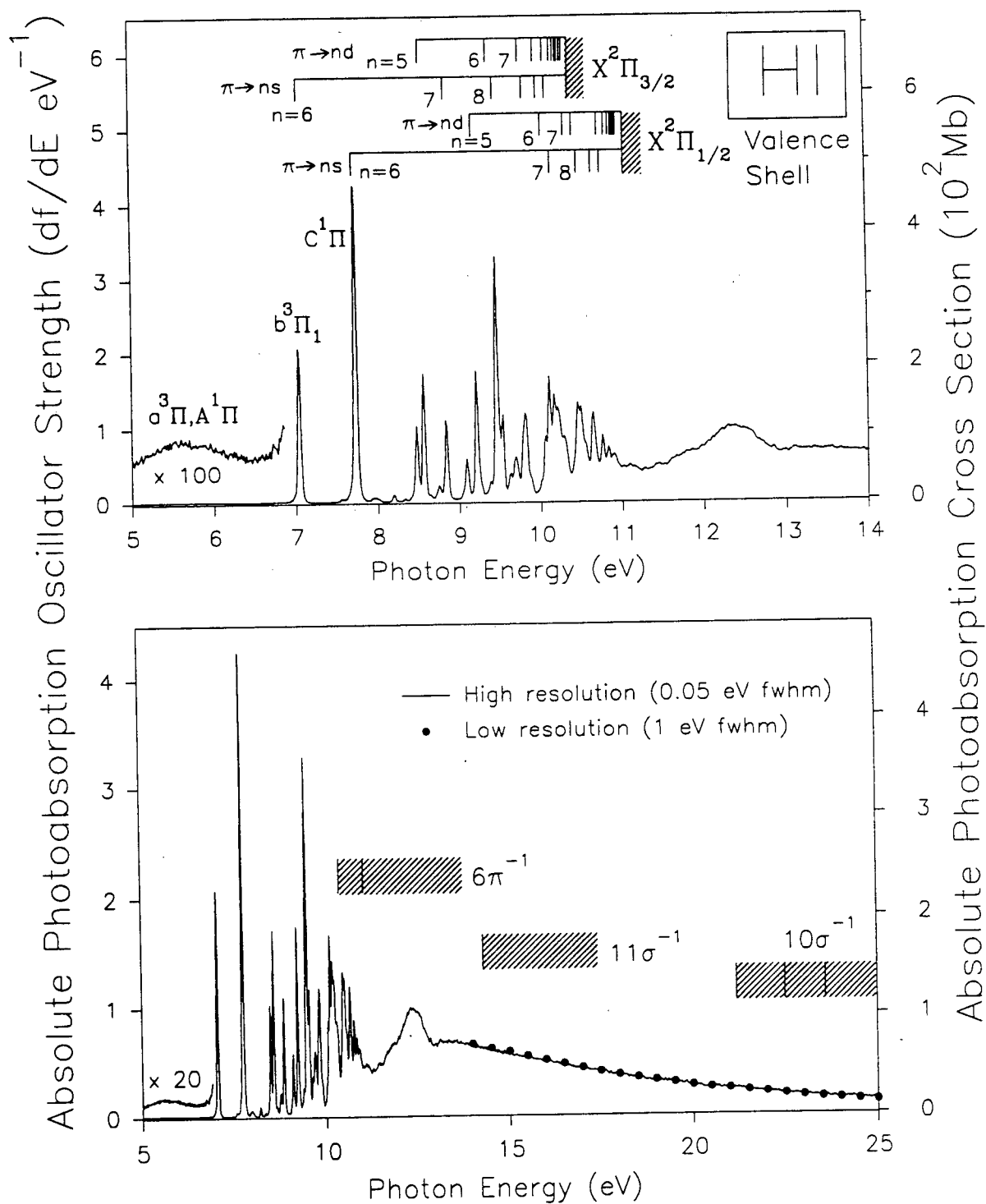
Figure 6.3: Absolute photoabsorption oscillator strengths (cross sections) for the valence shell of

HI, obtained with high resolution (0.05 eV fwhm).

Table 6.1: Integrated oscillator strengths (cross sections) for selected energy regions in the valence shell obtained from the present measurements of HI, with comparison to those reported in the literature.

Energy Range	Present Work (Mb)	ref. [35] (Mb)
5.40- 7.3	12.38	1.76
6.90- 7.1	10.98	
7.50- 7.9	25.35	
8.35- 8.68	14.60	
8.68- 8.90	7.46	
9.01- 9.14	3.61	
9.14- 9.31	10.06	
9.31- 9.59	2.56	
9.59- 9.75	7.22	
9.75- 9.93	11.58	
9.93-10.37	38.52	
10.37-10.60	21.07	
10.60-10.72	10.63	
10.72-10.80	6.26	

Roxlo and Mandl [35]. The cross sections obtained by both Romand [36] and Goodeve and

Taylor [99] are lower than those reported by Roxlo and Mandl [35].

Wang et al. [100] measured the absolute photoabsorption spectrum of HI in the region

between the $X^2\Pi_{3/2}$ and $X^2\Pi_{1/2}$ limits (10.4-11.1 eV) with apparently slightly higher resolution

than in the present work. The cross sections reported by Wang et al. are significantly lower

(~90%) than those reported in the present work.

6.2.2.3 High Resolution I 4d Inner Shell Photoabsorption Measurements of HI

The absolute photoabsorption oscillator strength (cross section) spectrum of the I 4d inner

shell of HI, obtained with high resolution (0.1 eV fwhm) from 48 to 60 eV is shown in figure 6.4

below. The two broad peaks with maxima at 51 and 52.8 eV correspond to the strong $4d \rightarrow \sigma^*$

transitions, with the spacing between the peaks corresponding to the spin-orbit splitting of the

$4d_{5/2,3/2}$ states. Above 54 eV, some discrete structure is visible, corresponding to transitions to

Rydberg states converging on the $4d_{5/2,3/2}$ ionization limits [105]. Integrated oscillator strengths

(cross sections) for selected energy regions in the I 4d inner shell of HI are given in table 6.2.
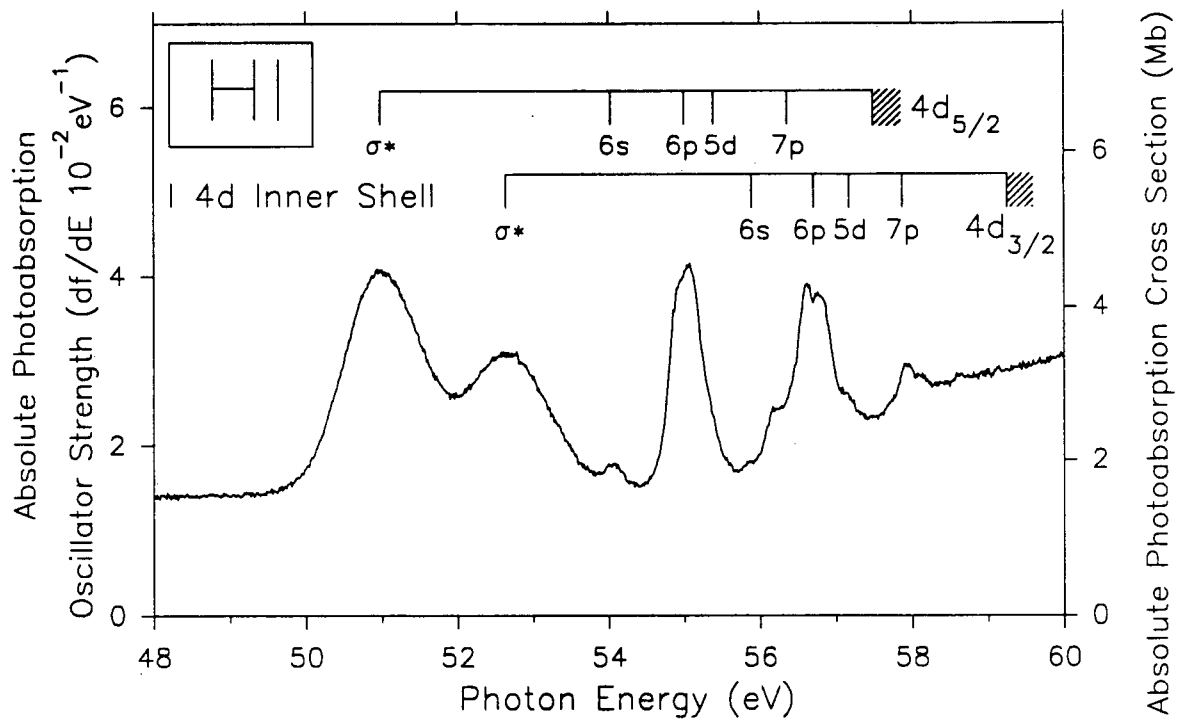
Figure 6.4: Absolute photoabsorption oscillator strength (cross section) spectrum of the I 4d

inner shell region of HI, obtained with high resolution (0.1 eV fwhm).

Table 6.2: Integrated oscillator strengths (cross sections) for selected energy ranges in the I 4d

inner shell of HI, with and without estimated contributions from the valence shell continuum.

Energy Range	df/dE (Mb)	
	With Valence	Without Valence
49.38-53.83	13.06	6.29
53.83-54.38	1.00	0.17
54.38-55.69	3.73	1.74
55.69-57.43	5.13	2.47
57.43-58.20	2.22	1.05
58.20-59.92	5.39	2.81

Table 6.3: Absolute differential photoabsorption oscillator strengths for the valence shell and I

4d inner shell regions of HI (1 eV fwhm).

Total Photoabsorption Oscillator Strength (df/dE)					
eV	$10^{-2}eV^{-1}$	eV	$10^{-2}eV^{-1}$	eV	$10^{-2}eV^{-1}$
6.0	-0.23	16.0	49.50	26.0	9.09
6.5	3.44	16.5	45.82	26.5	8.07
7.0	12.19	17.0	42.12	27.0	7.25
7.5	24.26	17.5	38.66	27.5	6.54
8.0	25.36	18.0	35.56	28.0	5.94
8.5	26.49	18.5	32.85	28.5	5.32
9.0	38.42	19.0	30.49	29.0	4.68
9.5	54.87	19.5	28.38	29.5	4.44
10.0	67.26	20.0	25.63	30.0	4.00
10.5	72.87	20.5	23.61	30.5	3.70
11.0	59.07	21.0	22.32	31.0	3.43
11.5	57.90	21.5	20.58	31.5	2.97
12.0	73.93	22.0	18.97	32.0	2.86
12.5	80.17	22.5	17.08	32.5	2.74
13.0	72.08	23.0	15.72	33.0	2.52
13.5	68.35	23.5	14.24	33.5	2.39
14.0	64.94	24.0	12.87	34.0	2.24
14.5	60.95	24.5	11.93	34.5	2.08
15.0	57.24	25.0	10.87	35.0	2.12
15.5	52.97	25.5	9.76	35.5	1.88

Table 6.3 (continued): Absolute differential photoabsorption oscillator strengths for the valence shell and I 4d inner shell regions of HI (1 eV fwhm).

| Total Photoabsorption Oscillator Strength (df/dE) |
eV	$10^{-2}eV^{-1}$	eV	$10^{-2}eV^{-1}$	eV	$10^{-2}eV^{-1}$
36.0	1.93	58.0	2.57	92.0	18.34
36.5	1.68	60.0	2.90	94.0	18.43
37.0	1.65	62.0	3.56	96.0	18.42
37.5	1.75	64.0	4.47	98.0	17.89
38.0	1.77	66.0	5.47	100.0	17.36
38.5	1.72	68.0	6.52	102.0	16.63
39.0	1.57	70.0	7.57	104.0	15.93
39.5	1.56	72.0	8.72	106.0	14.92
40.0	1.44	74.0	10.03	108.0	13.72
42.0	1.31	76.0	11.29	110.0	12.70
44.0	1.24	78.0	12.57	112.0	11.54
46.0	1.18	80.0	13.72	114.0	10.45
48.0	1.15	82.0	14.89	116.0	9.41
50.0	1.48	84.0	15.87	118.0	8.44
52.0	2.52	86.0	16.81	120.0	7.39
54.0	1.91	88.0	17.58		
56.0	2.18	90.0	18.06	—	

Chapter 7

Concluding Remarks

Dipole (e,e) spectroscopy has been used to obtain relative energy-loss spectra of HCl, HBr, and HI at high impact energies (8000 eV or 3000 eV) and at zero degree mean scattering angle. The Bethe-Born converted relative spectra were put onto an absolute photoabsorption scale by sum-rule normalization procedures. In the case of HCl, the VTRK sum rule (S(0)) was used, with extrapolation of the measured spectrum to infinite energy, and taking into account the correction factor for Pauli-excluded transitions. The accuracy of the absolute scale was confirmed by the very good value of the dipole polarizability of HCl obtained from S(-2) sum rule analysis of the absolute oscillator strength spectrum. The spectra of HBr and HI were normalized using the S(-2) sum rule, using experimental values of the dipole polarizability, due to the low-energy onsets of the Br 3d and I 4d inner shells, which preclude use of the VTRK sum rule. Thus absolute photoabsorption oscillator strengths (cross sections) were obtained for HCl, HBr, and HI. Previously published optical oscillator strength measurements using the Beer-Lambert law, have been found to be subject to serious "line-saturation" errors (i.e. linewidth-bandwidth interactions) in the discrete excitation regions of the photoabsorption spectra (see sections 1.3, 4.2.2.2, 5.2.2.2, 6.2.2.2).

Previous absolute photoabsorption data in the literature for the valence and inner shells of the halogen halides have been found to be quite limited. Where such data are available they are generally over rather small energy regions. Few studies have focused on HCl, and even fewer on HBr and HI. The present work has added significantly to scientific information in this area, and is the first study in which absolute photoabsorption data was obtained for all three molecules over

128

the UV, vacuum UV and soft X-ray regions, covering the valence as well as selected inner shells of the molecules (Cl 2p, Br 3d, and I 4d for HCl, HBr, and HI respectively).

In the cases of HCl and HBr, the present work gives absolute photoabsorption spectra for the entire range from 5 to 280 eV for HCl, and 5 to 300 eV for HBr. The present work has served to test the reliability of earlier, more limited energy range dipole (e,e) and dipole (e,e+ion) studies of HCl and HBr in this lab [10, 11]. The results from the earlier and present work have been compared, and certain problems anticipated from instrumental and data analysis methods used in the earlier work were confirmed. Comparisons have also been made with other published direct optical studies. In general these earlier Beer-Lambert law measurements have much lower cross sections in the discrete region than those measured in the present work due to line saturation errors in the optical work.

In the case of HI, absolute photoabsorption studies prior to the present work were limited to the regions below 8 eV, and between 10 and 11 eV. The present work is therefore the first absolute photoabsorption study to cover the entire valence and the I 4d inner shell regions, from 5 to 120 eV with low resolution (1.0 eV fwhm), and from 5 to 60 eV with high resolution (0.05-0.1 eV fwhm). The previously published absolute photoabsorption data were found to be significantly higher than the cross sections measured in the present work.

Dipole (e,e+ion) measurements for HCl and HBr were used to obtain photoion branching ratios and partial photoionization oscillator strengths (cross sections) for production of the molecular and dissociative ions. A consideration of these partial oscillator strengths for molecular and dissociative photoionization, together with partial oscillator strengths for the electronic states of the molecular ion (from dipole (e,2e) spectroscopy) has made possible some investigation of the dipole-induced breakdown pathways of HCl and HBr at VUV and soft X-ray energies.

Contributions from the various electronic ion state partial oscillator strengths to the partial oscillator strengths for the molecular and each dissociative ion were obtained.

The present work could be expanded in the future to include photoionization studies of HI, as well as photoion-photoion or photoelectron-photoion coincidence studies of HCl, HBr, and HI to give a more detailed analysis of the dipole breakdown pathways of each molecule. The numerical data for the photoabsorption of HCl, HBr, and HI at both low and high resolution can be obtained as ascii data files at the web location ftp://chem.ubc.ca/pub/cooper. Further details can be found in reference [7].

REFERENCES

[1] C.E. Brion, *Comm. At. Mol. Phys.*, **16**(5), (1985) 249.

[2] J.W. Gallagher, C.E. Brion, J.A.R. Samson, P.W. Langhoff, JILA Data Center Rep. no. 32, (1987).

[3] W.F. Chan, G. Cooper, and C.E. Brion, *Phys .Rev. A*, **44** (1991) 186.

[4] W.F. Chan, G. Cooper, and C.E. Brion, *Phys. Rev. A*, **45** (1992) 1420.

[5] W.F. Chan, G. Cooper, and C.E. Brion, *Chem. Phys.* **170** (1993) 123.

[6] W.F. Chan, G. Cooper, R.N.S. Sodhi and C.E. Brion, *Chem. Phys.* **170** (1993) 81.

[7] T.N. Olney, N.M. Cann, G. Cooper, and C.E. Brion, to be published (1997).

[8] F. Carnovale and C.E. Brion, *Chem. Phys.* **74** (1983) 253.

[9] F. Carnovale, R.Tseng, and C.E. Brion, *J. Phys. B: At. Mol. Opt. Phys.* **14** (1981) 4771.

[10] S. Daviel, Y. Iida, F. Carnovale, and C.E. Brion, *Chem. Phys.* **83** (1984) 319.

[11] C.E. Brion, Y. Iida, F. Carnovale and J.P. Thomson, *Chem. Phys.* **98** (1985) 327.

[12] J. A. R. Samson, *Techniques of Vacuum Ultraviolet Spectroscopy*, John Wiley & Sons, Inc., New York, 1967.

[13] M.S. Lubell, *Can. J. Phys.* **74** (1996) 713.

[14] C.E. Brion, S.Daviel, R. Sodhi, and A.P. Hitchcock, *AIP Conf. Proc.*, **94** (1982) 429.

[15] R.D. Hudson, *Rev. Geophys. Space Phys.* **9** (1971) 305.

[16] G.M. Lawrence, D.L. Mickey and K. Dressler, *J. Chem. Phys.* **48** (1968) 1989.

[17] H. Bethe, *Ann. Phys.* **5** (1930) 325.

[18] M. Inokuti, *Rev. Mod. Phys.* **43** (1971) 297.

[19] W.F. Chan, G. Cooper, X. Guo and C.E. Brion, *Phys. Rev. A* **45** (1992) 1420.

[20] M.J. Van der Wiel, *Physica* **49** (1970) 411.

[21]   J. Berkowitz, *Photoabsorption, photoionization and photoelectron spectroscopy*, Academic Press, New York, 1979.

[22]   G.R. Burton, W.F. Chan, G. Cooper, C.E. Brion, A. Kumar and W.J. Meath, *Can J Chem*, **71** (1993) 341.

[23]   J.L. Dehmer, M. Inokuti, and R.P. Saxon, *Phys. Rev. A* **12** (1975) 102.

[24]   C. Backx, R.R. Tol, G.R. Wight, and M.J. Van der Wiel, *J Phys B: At Mol Phys* **9** (1975) 2050.

[25]   C. Backx and M.J. Van der Wiel, *J Phys B: At Mol Phys*, **8** (1975) 3020.

[26]   Y. Iida, F. Carnovale, S. Daviel, and C.E. Brion, *Chem. Phys.*, **105** (1986) 211.

[27]   X. Guo, G. Cooper, W.F. Chan, G.R. Burton and C.E. Brion, *Chem. Phys.* **161** (1992) 453.

[28]   G. Cooper, Y. Zheng, G.R. Burton, and C.E. Brion, *Rev. Sci. Instrum.*, **64** (1993) 1140.

[29]   S. Daviel, C.E. Brion, and A.P. Hitchcock, *Rev. Sci. Instrum.* **55** (1984) 182.

[30]   W.L. Wiese, M.W. Smith and B.M. Glenon, Atomic Transition Probabilities, Vol 1. Hydrogen through Neon, NSRDS-NBS Circular No. 4 (U.S. GPO, Washington, D.C., 1966).

[31]   G. Cooper, T.N. Olney, and C.E. Brion, *Chem. Phys.* **194** (1995) 175.

[32]   T. Ogawa, T. Tsuboi, and K. Nakashima, *J. Chem. Phys.* **101** (1994) 3696.

[33]   J.B. Nee, M. Suto, and L.C. Lee, *J. Chem. Phys.*, **85** (1986) 719.

[34]   R.G. Wang, M.A. Dillon, and D. Spence, *J. Chem. Phys.* **80** (1984) 63.

[35]   C. Roxlo and A. Mandl, *J. Appl. Phys.* **51** (1980) 2969.

[36]   J. Romand, *Ann. Phys.* **4** (1949) 35.

[37]   J. Myer and J. Samson, *J. Chem. Phys.* **52** (1970) 266.

[38]   H. Frohlich and M. Glass-Maujean, *Phys. Rev. A* **42** (1990) 1396.

[39]   W. Hayes and F.C. Brown, *Phys. Rev. A* **6** (1972) 21.

[40] K. Ninomiya, I. Ishiguro, S. Iwata, A.Mikuni, and T. Sasaki, *J. Phys. B: At. Mol. Opt. Phys.* **14** (1981) 1777.

[41] D.T. Terwilliger and A.L Smith, *J. Mol. Spec.* **45** (1973) 366.

[42] D.S. Ginter and M.L. Ginter, *J. Mol. Spec.* **90** (1981) 177.

[43] S.G. Tilford and M.L. Ginter *J Mol Spec* **40** (1971) 568.

[44] S.G. Tilford, M.L. Ginter, and J.T Vanderslice, *J. Mol. Spec.* **33** (1970) 505.

[45] J.K. Jacques and R.F.Barrow, *Proc. Phys. Soc. London* **73** (1958) 538.

[46] T.A York and J. Comer, *J. Phys. B: At. Mol. Phys.* **17**(1984) 2563.

[47] D.A. Shaw, D. Cvejanovic, G.C. King, and F.H Read, *J. Phys. B: At. Mol. Phys.* **17** (1984) 1173.

[48] A.J.C. Nicholson, *J. Chem. Phys.* **43** (1965) 1171.

[49] H.J. Lempka, T.R. Passmore and W.C. Price, *Proc. Roy. Soc.* **A304** (1968) 53.

[50] M.J. Weiss, G.M. Lawrence, and R. A. Young, *J. Chem. Phys.* **52** (1970) 2867.

[51] M.Y. Adam, *Chem. Phys. Lett.* **128** (1986) 280.

[52] S. Svensson, L. Karisson, P. Baltzer, B. Wannberg, U. Gelius, M.Y. Adam, *J. Chem. Phys.* **89** (1988) 7192.

[53] A.A. Wills, D. Cubric, M. Ukai, F. Currell, B.J. Goodwin, T. Reddish, and J. Comer, *J. Phys. B: At. Mol. Opt. Spec.* **26** (1993) 2601.

[54] K. Faegri Jr. and H.P. Kelly, *Chem. Phys. Lett.* **85** (1982) 472.

[55] G. Cooper, G.R. Burton and C.E. Brion, *J. El. Spec.* **73** (1995) 139.

[56] J.W. Au, G.R. Burton and C.E. Brion, *Chem. Phys.* submitted (1997).

[57] M. Bettendorf, S.D. Peyerimhoff and R.J. Buenker, *Chem. Phys.* **66** (1982) 261.

[58] K.P. Huber and G. Herzberg, *Molecular spectra and molecular structure, Vol 4, Constants of diatomic molecules*, Van Nostrand, Princeton, 1979.

[59] D.M. Hirst and M.F. Guest, *Mol. Phys.* **41** (1980) 1483.

[60]   I.H. Suzuki, C.E. Brion, E. Weigold, and G.R.J. Williams, *Intl. J. Quant. Chem.* **18** (1980) 275.

[61]   B.P. Hollebone, C.E. Brion, E.R. Davidson, and C. Boyle, *Chem. Phys.* **173** (1993) 193.

[62]   M. Inokuti, private communication *Version (2) June 4, 1994.*

[63]   C. Cuthbertson and M. Cuthbertson, *Phil. Trans R. Soc. Lond. A,* **213** (1913) 1.

[64]   H.A. Stuart, *Landolt-Bornstein, Atom und Molekularphysik,* (Springer-Verlag, Berlin, Vol 1, Part 3, pp 509, 1951).

[65]   A.A. Maryott and F. Buckley, *U.S. National Bureau of Standards Circular No. 537,* (US GPO, Washington, DC, 1953).

[66]   U. Hohm and U. Trumper, *Chem. Phys.* **189** (1994) 443.

[67]   A. Kumar and W.J. Meath, *Can. J. Chem.* **63** (1985) 1616.

[68]   J. Dougherty and M.A. Spackman, *Mol. Phys.* **82** (1994) 193.

[69]   T.A. Carlson, M.O. Krause, F.A. Grimm, P.R. Keller and J.W. Taylor, *Chem. Phys. Lett.* **87** (1982) 552.

[70]   M.W. Chase, Jr, C.A. Davies, J.R. Downey, Jr, D.J. Frurip, R.A. McDonald, and A.N. Syverud, *J. Phys. Chem. Ref. Data,* **14** (1985).

[71]   M. Krauss, J.A. Walker, and V.H. Dibeler, *J. Res. Nat. Bur. Stand.* **72A** (1968) 281.

[72]   R.E. Fox, *J. Chem. Phys.* **26** (1957) 1281.

[73]   F.H. Dorman, J.D. Morrison, *J. Chem. Phys.* **35** (1961) 575.

[74]   C.E. Brion, I.E. McCarthy, I.H. Suzuki, E. Weigold, G.R.J. Williams, K.L Bedford, A.B. Kunz, and R. Weidman, *J. El. Spec. Rel. Phen.* **27** (1982) 83.

[75]   M.J. Van der Wiel and C.E. Brion, *J. El. Spec.* **1** (1972/1973) 309.

[76]   F. Carnovale, A.P. Hitchcock, J.P.D. Cook, and C.E. Brion, *Chem. Phys.* **66** (1982) 249.

[77]   K.H. Tan, C.E. Brion, P.E. Van der Leeuw, and M.J. Van der Wiel, *Chem. Phys.* **29** (1978) 299.

[78]   J.B. Nee, M. Suto, and L.C. Lee, *J. Chem. Phys.,* **85** (1986) 4919.

[79] G. Brasseur and S. Solomon, *Aeronomy of the Middle Atmosphere,* Reidel, Amsterdam (1984).

[80] P.D. Brewer, S. Halle, and R.M. Osgood, Jr., *Appl. Phys. Lett.* **45** (1984) 475.

[81] J. Huebert and R.M. Martin, *J. Phys. Chem.* **72** (1968) 3046.

[82] A. Goodeve and W.C. Taylor, *Proc. R. Soc. London. Ser. A* **152** (1935) 221.

[83] M.L. Ginter and S.G. Tilford, *J. Mol. Spec.* **34** (1970) 206.

[84] M.L. Ginter and S.G. Tilford, *J. Mol. Spec.* **37** (1971) 159.

[85] D.S. Ginter, M.L. Ginter and S.G. Tilford, *J. Mol. Spec.* **90** (1981) 152.

[86] M.A. Baig, J. Hormes, J.P. Connerade and W.R.S. Garton, *J. Phys. B: At. Mol. Phys.* **14** (1981) L147.

[87] D.T. Terwilliger and A.L Smith, *J. Mol. Spec.* **50** (1974) 30.

[88] R. Puttner, M. Domke, K. Schulz, A. Gutierrez and G. Kaindl, *J. Phys. B: At. Mol. Opt. Phys.* **28** (1995) 2425.

[89] P. Morin and I. Nenner, *Phys. Rev. Lett.* **56** (1986) 1913.

[90] M.Y. Adam, M.P. Keane, A. Naves de Brito, N. Correia, P. Baltzer, B. Wannberg, L. Karlsson and S. Svensson, *J. El. Spec. Rel. Phen.* **58** (1992) 185.

[91] M. Salzmann, N. Bowerin, H-W. Klausing, R. Kuntze and U. Heinzmann, *J. Phys. B: At. Mol. Opt. Phys.* **27** (1994) 1981.

[92] Z.F. Liu, G.M. Bancroft, K.H. Tan and M. Schachter, *Phys. Rev. Lett.* **72** (1994) 621.

[93] Z.F. Liu, G.M. Bancroft, K.H. Tan and M. Schachter, *J. El. Spec. Rel. Phen.* **67** (1994) 299.

[94] K. England, T. Reddish, and J. Comer, *J. Phys. Lett.* **23** (1990) 2151.

[95] D.W. Turner, C. Baker, A.D. Baker and C.R. Brundle, *Molecular Photoelectron Spectroscopy,* Wiley-Interscience, London (1970).

[96] J. Delwiche, P. Natalis, J. Monigny and J.E. Collin, *J. El. Spec. Rel. Phen.* **1** (1973) 219.

[97] J.G. Lias, J.E. Bartness, J.F. Liebman, J.L. Holmes, R.D. Levin, and W.G. Mallard, *J. Phys. Chem. Ref. Data,* **17** (1988) Suppl No. 1, 1.

[98] H.M. Rosenstock, K. Draxl, B.W. Steiner and J.T. Herron, *J. Phys. Chem. Ref. Data* **6** (1977) Suppl. No. 1

[99] A. Goodeve and W.C. Taylor, *Proc. R. Soc. London Ser. A* **154** (1936) 181.

[100] H.T. Wang, W.S. Felps, G.L. Findley, A.R.P. Rau, and S. P. McGlynn, *J. Chem. Phys.* **67** (1977) 3940.

[101] C.E. Brion and A.P. Hitchcock, *J. Phys. B* **13** (1980) L677.

[102] M.Y. Adam, M.P. Keane, A. Naves de Brito, N. Correia, B. Wannberg, P. Baltzer, L. Karlsson and S. Svensson, *Chem. Phys.* **164** (1992) 123.

[103] N. Bowering, M. Muller, M. Salzmann, and U. Heinzmann, *J. Phys. B: At. Mol. Opt. Phys.* **24** (1991) 4793.

[104] T.A. Carlson, A.Fahlman, M.O. Krause, P.R. Keller, J.W. Taylor, T. Whitley, and F.A. Grimm, *J. Chem. Phys.* **80** (1984) 3521.

[105] L. Karlsson, S Svensson, P. Baltzer, M. Carlsson-Gothe, M.P. Keane, A. Naves de Brito, N. Correia, and B. Wannberg, *J. Phys. B: At. Mol. Opt. Phys.* **22** (1989) 3001.

[106] J.N. Cutler, G.M Bancroft, and K.H. Tan, *J. Phys B: At. Mol. Opt. Phys.* **24** (1991) 4897.

[107] B.P. Tsai and T. Baer, *J. Chem. Phys.* **61** (1974) 2047.

[108] J.H.D. Eland and J. Berkowitz, *J. Chem. Phys.* **67** (1977) 5034.

[109] G. Raseev, F. Keller, and H. Lefebvre-Brion, *Phys. Rev. A* **36** (1987) 4759.

[110] J.N. Cutler, G.M. Bancroft and K.H. Tan, *J. Chem. Phys.* **97** (1992) 7932.